

AD\_\_\_\_\_

Award Number: DAMD17-03-1-0023

TITLE: Intensity Modulated Radiation Treatment of Prostate  
Cancer Guided by High Field MR Spectroscopic Imaging

PRINCIPAL INVESTIGATOR: Lei Xing, Ph.D.

CONTRACTING ORGANIZATION: Stanford University  
Stanford, California 94305-5401

REPORT DATE: May 2004

TYPE OF REPORT: Annual

PREPARED FOR: U.S. Army Medical Research and Materiel Command  
Fort Detrick, Maryland 21702-5012

DISTRIBUTION STATEMENT: Approved for Public Release;  
Distribution Unlimited

The views, opinions and/or findings contained in this report are those of the author(s) and should not be construed as an official Department of the Army position, policy or decision unless so designated by other documentation.

20041215 055

**REPORT DOCUMENTATION PAGE**Form Approved  
OMB No. 074-0188

Public reporting burden for this collection of information is estimated to average 1 hour per response, including the time for reviewing instructions, searching existing data sources, gathering and maintaining the data needed, and completing and reviewing this collection of information. Send comments regarding this burden estimate or any other aspect of this collection of information, including suggestions for reducing this burden to Washington Headquarters Services, Directorate for Information Operations and Reports, 1215 Jefferson Davis Highway, Suite 1204, Arlington, VA 22202-4302, and to the Office of Management and Budget, Paperwork Reduction Project (0704-0188), Washington, DC 20503

<b>1. AGENCY USE ONLY</b> (Leave blank)		<b>2. REPORT DATE</b> May 2004	<b>3. REPORT TYPE AND DATES COVERED</b> Annual (1 May 2003 - 30 Apr 2004)
<b>4. TITLE AND SUBTITLE</b> Intensity Modulated Radiation Treatment of Prostate Cancer Guided by High Field MR Spectroscopic Imaging			<b>5. FUNDING NUMBERS</b> DAMD17-03-1-0023
<b>6. AUTHOR(S)</b> Lei Xing, Ph.D.			
<b>7. PERFORMING ORGANIZATION NAME(S) AND ADDRESS(ES)</b> Stanford University Stanford, California 94305-5401  <i>E-Mail:</i> lei@reyes.stanford.edu			<b>8. PERFORMING ORGANIZATION REPORT NUMBER</b>
<b>9. SPONSORING / MONITORING AGENCY NAME(S) AND ADDRESS(ES)</b> U.S. Army Medical Research and Materiel Command Fort Detrick, Maryland 21702-5012			<b>10. SPONSORING / MONITORING AGENCY REPORT NUMBER</b>
<b>11. SUPPLEMENTARY NOTES</b>			
<b>12a. DISTRIBUTION / AVAILABILITY STATEMENT</b> Approved for Public Release; Distribution Unlimited			<b>12b. DISTRIBUTION CODE</b>
<b>13. ABSTRACT (Maximum 200 Words)</b> <p>With the development of computer controlled multileaf collimators, IMRT now provides unprecedented means for us to deliver 3D-dose distributions with sub-centimeter resolution. Simultaneously, MRSI is capable of noninvasively providing critically needed 3D metabolic and physiological information. Together with anatomical CT or MRI images, functional imaging affords valuable 4D data (3D structural plus 1D metabolic). A timely issue is how to integrate the metabolic/functional data into IMRT treatment planning to improve clinical prostate cancer management. Toward establishing biologically conformal radiation therapy for prostate treatment, we have carried out a series of studies and developments and have successfully accomplished a number of important milestones of the proposed project. These include (i) implemented 3T prostate MRSI technique with J-resolved pulse sequence; (ii) developed a robust image registration procedure to map endorectal coil-based MRSI data onto treatment planning CT/MRI images; (iii) performed experimental validation of the image registration tools; (iv) designed and fabricated MRSI quality assurance phantom; and (v) improved currently available inverse planning algorithm for MRSI-guided prostate IMRT. Integration and further refinement of the above tools are still underway. It is expected these tools will greatly facilitate the imaging, planning, delivery, and quality assurance of MRSI-guided prostate treatment.</p>			
<b>14. SUBJECT TERMS</b> Prostate cancer			<b>15. NUMBER OF PAGES</b> 159
			<b>16. PRICE CODE</b>
<b>17. SECURITY CLASSIFICATION OF REPORT</b> Unclassified	<b>18. SECURITY CLASSIFICATION OF THIS PAGE</b> Unclassified	<b>19. SECURITY CLASSIFICATION OF ABSTRACT</b> Unclassified	<b>20. LIMITATION OF ABSTRACT</b> Unlimited

NSN 7540-01-280-5500

Standard Form 298 (Rev. 2-89)  
Prescribed by ANSI Std. Z39-18  
298-102

## Table of Contents

1.	Cover page .....	1
2.	SF 298 .....	2
3.	Table of Contents .....	3
3.	Introduction.....	4
3.	Body .....	4
4.	Key Research Accomplishments .....	11
5.	Reportable Outcomes.....	12
6.	Conclusions.....	13
8.	References.....	14
14.	Appendices.....	15

## **I. INTRODUCTION**

This Idea Award (DAMD17-03-1-0023, entitled "Intensity Modulated Radiation Treatment of Prostate Cancer Guided by High Field MR Spectroscopic Imaging") was awarded to the principal investigator (PI) for the period of May 1, 2003—April 30, 2006. This is the annual report for the first funding period (May 1, 2003 –April 30, 2004). The goal of this project is to establish biologically conformal - as opposed to anatomically conformal - IMRT as a viable modality through integration with 3T MRSI imaging to more effectively kill prostate tumor cells. The underlying hypothesis driving this work is that the MRSI-guided IMRT will provide substantially improved dose distributions required to achieve greater local tumor control while maintaining, or reducing, complications to sensitive structures. The specific aims of the project are: (1) To establish a robust procedure for registering and mapping of MR spectroscopic data to CT/MRI images for prostate irradiation. (2) To develop an inverse planning system for MRSI-guided IMRT prostate treatment and demonstrate the feasibility of concurrent dose escalation to intraprostatic lesion(s) through a set of phantom studies and at least two previously treated prostate cases who had undergone CT/MRSI scans. Under the generous support from the U.S. Army Medical Research and Materiel Command (AMRMC) , the PI has contributed significantly to prostate cancer research by applying physics and engineering knowledge to prostate cancer research. A number of conference abstracts and refereed papers have been resulted from the support. The preliminary data obtained under the support of the grant has also enabled the PI to start new research initiatives and significantly advanced his academic career. In this report, the past year's research activities if the PI are highlighted.

## **II. RESEARCH AND ACCOMPLISHMENTS**

Prostate Intensity modulated radiation therapy (IMRT) is an image-guided process whose success depends critically on the imaging modality used for treatment planning and the level of integration of the available information. In current clinical practice, IMRT prostate treatment planning, performed under the guidance of CT or MRI, is aimed at achieving uniform dose distribution to the entire prostate volume. While tumor biology plays a crucial role in the treatment outcome, neither MRI nor CT provides biological information(9, 11, 13). Recent advancement of MR spectroscopic imaging (MRSI)(2, 10, 14), especially high field (3 Tesla) MRSI, now makes possible to effectively distinguish between regions of cancer and normal prostatic epithelium with clinically acceptable resolution (~3mm). Coupled with the technical capability of IMRT for delivering customized 3D dose distributions, an important and timely question to ask is whether the metabolic information derived from MRSI can be used for more objective tumor delineation and for guiding IMRT treatment planning.

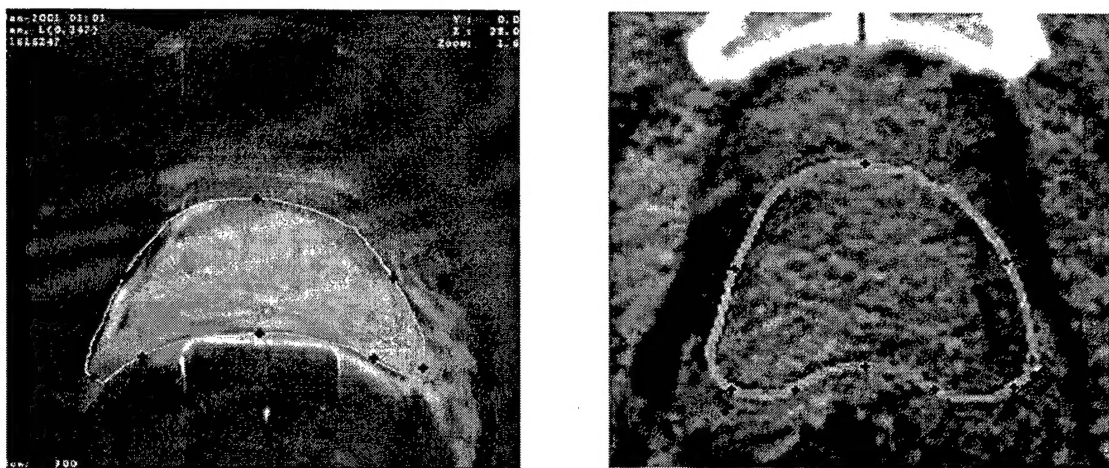


Toward establishing biologically conformal IMRT for prostate cancer treatment, we have done substantial work in the past year in integration of MRSI imaging into IMRT treatment planning and in improving the existing prostate IMRT planning techniques. The research is sorted into four different categories and summarized below.

***Development of 3T MRSI techniques:*** We have successfully implemented single- and multi-voxel and versions of J-resolved MRS sequences in order to better detect and quantify a number of smaller  $^1\text{H}$  MRS peaks, including those from glutamate (Glu) and myo-Inositol (mI). The detection of many smaller metabolites in the  $^1\text{H}$  spectrum is complicated by signal overlap due to both a small dispersion in chemical shift and the multiplet structure of J-couple resonances. An effective remedy is to use two-dimensional J-resolved MRS (2D-J-MRS) where chemical shift and J-coupling information are separated into two different frequency axis known as  $f_1$  and  $f_2$  respectively. Closely related to 2D-J-MRS, Constant-Time PRESS (CT-PRESS) has been introduced as a method to detect coupled resonances with effective homonuclear decoupling and high SNR. A PRESS module for spatial localization is followed by an additional refocusing pulse whose position is shifted from excitation to excitation to encode chemical shift in the second frequency dimension ( $f_1$ ). In contrast to 2D-J-MRS, the time interval between excitation and data acquisition is kept constant. While CT-PRESS is a 2D experiment, data are usually display as a 1D “diagonal” spectrum obtained by integrating the 2D magnitude spectrum along  $f_2$  within a limited range about the spectral diagonal. As we have demonstrated, an advantage of this technique is that the evolution time can be optimized with respect to the coupling constants of a given spin system, hence increasing the SNR for a particular metabolite. In vivo data demonstrated the robust detection of Glu, NAA, Cho, Cre, and mI resonances. We have further extended our CT-PRESS acquisition with the addition of spiral readout gradients for spectroscopic imaging. In vivo results demonstrate single-slice variable density spiral MRSI CT-PRESS with excellent spectral quality in good agreement with a corresponding single-voxel acquisition. A manuscript on in vivo detection of citrate for prostate cancer at 3T has been submitted to *Magnetic Resonance Imaging in Medicine*.

***Using Biomechanical Model to Register Endorectal Coil-Based MRI/MRSI with Treatment Planning CT Images:*** As it is practiced now, radiation therapy treatment planning is mostly done based on CT image and it is thus required to map any new imaging information onto treatment planning CT images. The introduction of endorectal surface coils significantly improve spatial resolution and signal-to noise ratio (SNR) of prostate MR imaging and allows evaluation of the tumor location, tumor volume, capsular

penetration, invasion of neurovascular bundle, and seminal vesicle involvement, which is crucial for accurate treatment planning. Endorectal-coil based MRSI has also been shown effective in distinguishing between areas of cancer and normal prostatic epithelium through differences in [choline+ creatine]/citrate ratio (2, 5, 6, 14). However, the use of endorectal probe inevitably distorts the prostate and other soft tissue organs, making it impossible to directly fuse the acquired image data onto treatment planning CT. In figure 1 we show the difference between endorectal coil-based MRI defined and CT-defined prostate volume (8). In order to fuse MRI/MRSI with treatment planning CT, it is needed to develop an effective deformable image registration procedure. Otherwise, the gain from the use of the state-of-the-art imaging techniques may be lost due to the inferior performance of image registration.



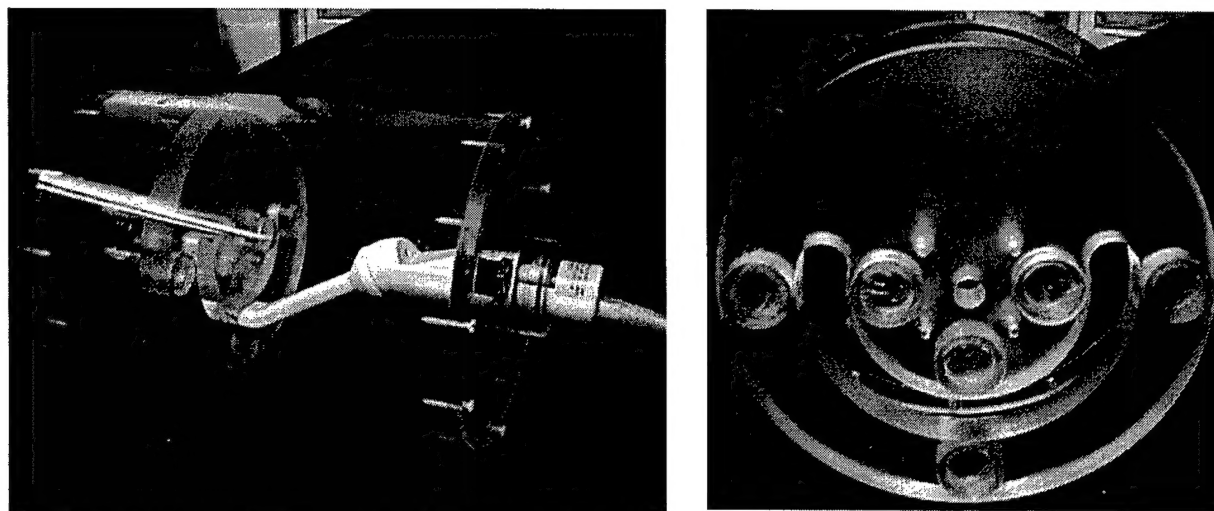
**Figure 1** Difference between endorectal coil-based MRI defined and treatment planning CT-defined prostate volumes.

Image registration is the determination of a geometrical transformation that aligns points in one view of an object with corresponding points in another view of that object or another object. Different methods have been proposed to deal with the registration of deformed organs but the optimal approach is still illusive in many cases, especially when the distortions are severe. We have recently applied the *thin-plate splines* (TPS) method (7) to deal with the registration of endorectal MRI/MRSI and verified the accuracy of the registration by phantom and patient studies (the work has been conditionally accepted for publication in *Medical Physics*). For this purpose, a thin plate spline (TPS) transformation first introduced by Bookstein (1) was implemented to establish voxel-to-voxel correspondence between a *reference* image and a *floating* image with deformation. The idea is to find a continuous transformation within a suitable Hilbert space to minimize the landmark difference in two images. The detailed description of the TPS transformation can be found in Bookstein's original paper (1). To access the quality of the registration, an

elastic phantom with a number of implanted fiducial markers was designed. Radiographic images of the phantom were obtained before and after a series of intentionally introduced distortions. After mapping the distorted phantom to the original one, the displacements of the implanted markers were measured with respect to their ideal positions and the mean error was calculated. Phantom studies showed that using the deformable registration method the mean landmark displacement error was  $0.62 \pm 0.39$  mm when the distortion was of the order of 23.07 mm. A deformable model seems to be necessary to faithfully map the metabolic information onto the treatment CT images. When a non-deformable method based on a rigid-body transformation and scaling was used for the same distortion, the mean displacement of the fiducials with respect to their actual positions was found to be as large as  $12.95 \pm 0.57$  mm. In patient studies, CT images of two prostate patients were acquired, followed by 3 Tesla (3T) MR images with a rigid endorectal coil. For both patient studies, significantly improved registration accuracy was achieved. The prostate centroid position displacement was  $0.58 \pm 0.10$  mm and the coincidence index was  $92.6 \pm 5.1$  % when a TPS transformation was used. Different from the non-deformable approach, the TPS-based registration accommodates the organ distortion and enables us to achieve significantly higher MR/MRSI and CT image registration accuracy. A more advanced and automated finite element method is being developed to attack the problem (12), which is briefly summarized here.

The finite-element calculation was performed using an open-source software toolkit named the Insight Toolkit (ITK) (Insight Software Consortium). For the problem of multi-modality deformable registration, the ITK provides an implementation of finite-element model (FEM)-based algorithm. In this implementation, each image is viewed as a set of iso-intensity contours. The main idea is that a regular grid of forces deform an image by pushing the contours in the normal direction. The orientation and magnitude of the displacement is derived from the commonly used instantaneous optical flow equation. The FEM-based deformable registration models the image as a block of elastic material on which the forces are applied. The forces are computed based on the local derivatives of image metrics on points of a coarse grid. In general, subject to the same forces, higher elasticity results in smaller displacements, and higher density results also in smaller displacements. The algorithm is initialized with a deformation vectors assessed by a spline-based deformable registration applied on a mesh of automatically generated points. The elasticity and tissue density used in our calculation are from the literature and fine-tuning of the parameters is sometime required to better map the MRI and CT images. The accuracy of a FEM deformable image registration method is evaluated by using elastic phantom with known physical properties. The goodness of multi-modality deformable registration is quantitatively assessed using a mutual information metric. The metric is voxel-based and no control point or manual intervention from

the user is needed. In addition to the mutual information assessment, other software tools are also implemented to visually assess the registration results and to facilitate the interaction with radiation oncologists. Two patient studies yield consistent agreement and suggest that the approach is adequate for radiation therapy application. The whole registration procedure for a complete 3D study containing  $512 \times 512 \times 64$  voxels is less than 1 hour on a standard PC. The restored MRI/MRSI image data are written in the CT-coordinates in DICOM image form and can be easily imported by any treatment planning system. The registration works directly on 3D images and no control points need to be specified by clinician. We are in the process of refining the tool for MRSI-guided prostate IMRT and writing up the manuscript for publication.



**Figure 2.** A photo of quality assurance phantom built for testing/validating the geometric and metabolic accuracy of the endorectal coil-based MRI/MRSI.

***Phantom design and measurement for validation and quality assurance of MRSI:*** Increasingly, *ratios* of organ-specific metabolite intensities, as measured by MRSI methods, are being used to differentiate regional levels of abnormality for diseased tissue. We developed a QA phantom (figure 2 shows a photo of the phantom) and procedure to ensure the accuracy of MRSI-derived metabolite data (3). A phantom filled with a prostate-mimicking solution was custom-built with an insert holding a few vials containing calibrated solutions of precisely varying metabolite concentrations that emulated increasing grade/density of prostate tumor. This work is an extension of our previous work on brain MRSI phantom measurement(4). Metabolite ratios calculated from MRS data for each vial were compared to calibration ratios acquired *in vitro* at 9.4 T. Least squares regression analysis was used to investigate these relationships. Regression analysis revealed an expected linear relationship with regression coefficients close to 1 and intercepts close to 0 for the three

acquisition modes. This simple phantom-based QA of MRS metabolite ratio data quality is useful in a routine clinical environment or for development of new MRS and MRSI acquisition software.

***Improve IMRT dose distribution by using non-uniform penalty scheme:*** We have established a novel inverse planning formalism for producing spatially non-uniform IMRT dose distributions. A strategy to model the intra-structural tradeoff has been developed. Generally speaking, voxels within a structure volume are not equivalent in achieving their dosimetric goals. To consider this in inverse planning, we proposed to purposely modulating the penalty on individual voxel level based on the *a priori* dosimetric capability (which is quantified by the dosimetric capability that measures the degree for a voxel to achieve its dosimetric goal and is obtained by using a Cimmino algorithm on a case specific basis). We have shown that an inverse planning framework with customized non-uniform importance factors can lead to significantly improved IMRT treatment plans that would otherwise be unattainable. A manuscript has been submitted to *International Journal of Radiation Oncology, Biology, Physics* for consideration of publication.

In a separate but related project, we have developed a biologically more sensible yet clinically practical inverse planning system for functional image-guided IMRT planning. Current inverse planning is done using dose-based algorithms, which do not consider the nonlinear dose response for tumors and normal structures. The choice of structure specific importance factors represents an additional degree of freedom of the system and makes rigorous optimization intractable. We proposed to characterize the dose-volume status of a structure by using the concept of effective volume in the voxel domain and constructed an objective function with incorporation of the volumetric information. To automate the determination of the structure specific importance factors, we wrote the conventional importance factor of an organ into a product of two components: (i) a generic importance that parameterizes the relative importance of the organs in the ideal situation when the goals for all the organs are met; (ii) a dose-dependent factor that quantifies our level of clinical/dosimetric satisfaction for a given plan. The generic importance is determined *a priori*, and in most circumstances, does not need adjustment, whereas the second one, which is responsible for the intractable behavior of the tradeoff seen in conventional inverse planning, is determined automatically. Compared with the conventional inverse planning technique, we found that, for the same target dose coverage, the critical structure sparing was substantially improved for all testing cases.

To show potential benefit of the stated non-uniform penalty scheme, in Fig. 3 we plotted the isodose distribution for a prostate IMRT case. With this newly proposed technique, we found that the dose distribution was remarkably improved in comparison with the conventional IMRT plan obtained with



structurally uniform importance factors. In this case, the dose everywhere within the sensitive structure was reduced by ~17%. Clinically, this implies that the target dose may be escalated by ~10% while keeping the toxicity at the level achievable by current IMRT planning technique. Considering the improvement was accomplished purely from a more physical modeling of the system, the result is quite striking. The above planning formalism is ideally suitable for deriving spatially non-uniform dose distributions. This work is still in progress.

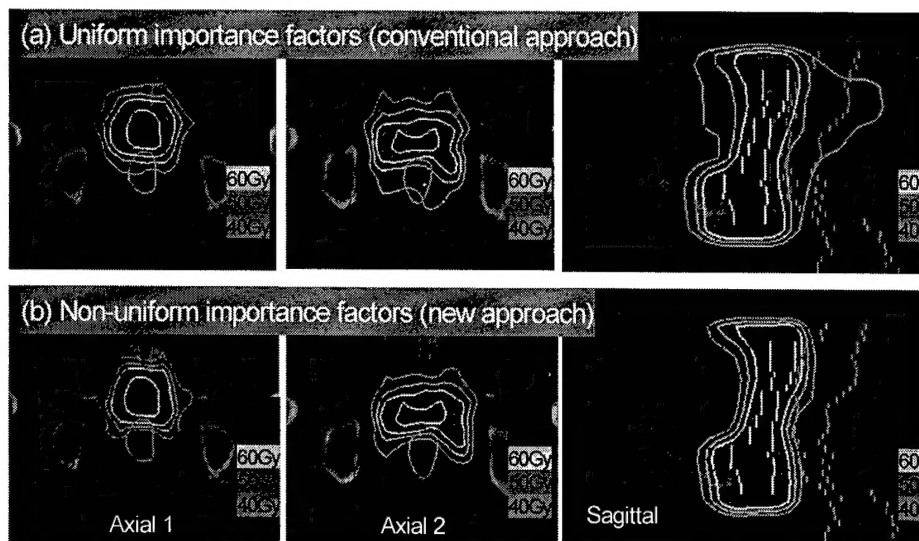


Fig. 3 Comparison of isodose distributions for a 5-field prostate case: (a) conventional approach (upper); (b) new approach (lower). The contours of the target (white) and the rectum (green) are also shown. It is clearly seen that the use of non-uniform importance factors allow us to "push" the high and intermediate isodose curves toward the target. The dosimetric improvement can also be seen in the DVHs shown in Fig. 4.

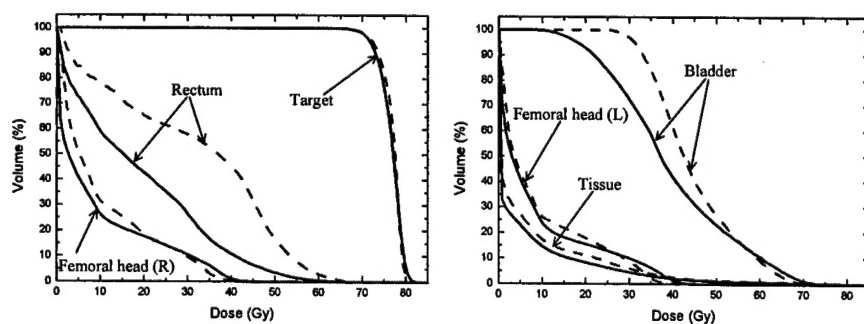


Fig. 4 Comparison of DVHs for a 5-field prostate case (isodose distributions are shown in Fig. 3). The dashed (red) and solid (blue) curves correspond to conventional plan and the plan obtained using non-uniform importance factors, respectively.

The Idea Award for Prostate Cancer Research from US Army Medical Research and Materiel Command also provides a unique educational opportunity for training junior researcher through the participation of research activities. In this aspect, the postdoctoral fellow, Eduard Schreiber, has been benefited greatly from the support. After obtaining his Ph.D. degree in Medical Physics from University of

Patras, Greece, Dr. Schreibmann jointed my group last year. Since he came here, he has had opportunity to learn the clinical prostate treatment planning, simulation, and quality assurance and many aspects of radiation treatment of prostate cancer. He has developed an elegant and clinically practical method of beam orientation optimization for prostate IMRT. He has also done substantial work on MRSI-CT image registration, which will be presented in the upcoming ASTRO annual meeting. He will continue working under the PI's supervision on the project. Given his training obtained under the support of this grant and his performance in the past year, I expect that he will become a leading researcher in the fields of medical physics and prostate radiotherapy in the years to come.

### III. KEY RESEARCH ACCOMPLISHMENTS

- Implemented 3T prostate MRSI technique with J-resolved pulse sequence.
- Developed a TPS-based deformable image registration tool for mapping prostate MRSI data onto treatment planning CT/MRI images. A more automated finite-element deformable registration method to further improve the TPS technique is close to be completed.
- Validated the deformable image registration model using elastic phantom.
- Designed and fabricated a phantom and carried out a series of measurement to validate the prostate MRSI data and to ensure the quality of endorectal coil-based MRI/MRSI images.
- Developed a novel inverse planning algorithm with spatially non-uniform penalty for optimizing the prostate IMRT plan.

#### IV. REPORTABLE OUTCOMES

The following is a list of publications resulted from the grant support. Copies of the publication materials are enclosed with this report.

##### Refereed publications:

1. Yong Y, Xing L, "Inverse planning with adaptively evolving voxel-dependent penalty scheme", *Medical Physics*, accepted.
2. Lian J, Hunjan S, Daniel B, Lo A, Levin J, Cardenas C, Dumoulin C, Watkins R, Rohling K, Giaquinto R, Boyer A, Xing, L. Mapping of the Prostate in Endorectal Coil-Based MRI/MRSI and CT: A Deformable Registration and Validation Study. *Medical Physics* 31: conditionally accepted., 2004.
3. Schreibmann E and Xing L, "Beam orientation class-solutions for IMRT prostate cancer treatment". *Medical Physics*, submitted.
4. Yang Y and Xing L, "Clinical knowledge-based inverse treatment planning". *International Journal of Radiation Oncology, Biology, Physics*, submitted.
5. Kim D, Mayer D., Xing L, Daniel B, Margolis, D., Spielman D., "In vivo detection of citrate for prostate cancer at 3 Tesla", *Magnetic Resonance Imaging in Medicine*, submitted.

##### Conference abstracts:

The PI's group has also been active in disseminating our research results. The following are some of the presentations given in various national/international meetings.

1. Lian J. and Xing L., Biological Model Based IMRT Optimization with Inclusion of Parameter Uncertainty, International Conference on Computers in Radiotherapy, Seoul, Korea, May, 2004.
2. Shou Z. and Xing L., Improve IMRT dose distribution using spatially non-uniform importance factors, International Conference on Computers in Radiotherapy, Seoul, Korea, May, 2004.
3. Xing L and Shou Z., "Intrinsic spatial heterogeneity in inverse planning and its significant role in defining the IMRT solution space", 2004 ASTRO Annual Meeting.
4. Yong Y. and Xing L, "Clinical knowledge-based inverse planning", 2004 ASTRO Annual Meeting.
5. Schreibmann E. and Xing L., "Dose-Volume Based Ranking of Incident Beams and its Utility in Facilitating IMRT Beam Placement", 2004 ASTRO Annual Meeting.
6. Schreibmann E., D. Kim, S. L.Hancock, A.L. Boyer, D. Spielman, B. Daniel, and Xing L., "Using Finite-Element Method to Register Endorectal Coil-Based MRI/MRSI with Treatment Planning CT Images", 2004 ASTRO Annual Meeting.

##### Invited talks:

The PI has been invited as abstract review and session chair in several national/international meetings and has given a number of invited talks. The following is a partial list of the relevant activities in last year.

1. Debate Session: IMRT or Proton? World Congress on Medical Physics and Biomedical Engineering, Sydney, Australia, Aug., 2003.
2. Dose Matching in IMRT, World Congress on Medical Physics and Biomedical Engineering, Sydney, Australia, Aug., 2003.
3. Integration of Functional Imaging into Radiation Therapy Planning, Workshop on Image Guided Radiotherapy, Lake Tahoe, Sept., 2003.
4. Functional and Molecular Imaging, Midwinter Symposium of AAPM Southern California Chapter, Los Angeles, Jan, 2004.
5. Clinical Knowledge-Based Inverse Planning, International Workshop on Intensity-Modulated Radiation Therapy, Medical Imaging, and Optimization, University of Haifa, Israel, June, 2004, to be delivered.



6. Recent Progress in Inverse Treatment Planning, Annual Radiological Society Meeting of Taiwan, Taipei, March, 2004.
7. Functional and Molecular Imaging, Image-Guided Interventions: Trial Design Methodology Workshop, Sponsored by the Cancer Imaging Program, NCI, Feb., 2004.
8. Toward Biologically Conformal Radiation Therapy. International Conference on Computers in Radiotherapy, May, Seoul, Korea, 2004.
9. Biological Imaging and Biological Imaging-Guided IMRT, American Cancer Society El Cerrito Relay for Life Open Ceremony, May, 2004.

**Book Chapters:**

1. Xing L., Yang Y., Spielman D., Molecular/Functional Image-Guided Radiation Therapy, T. Bortfeld, R. Schmidt-Ullrich, W. de Neve (editors), Springer-Verlag Heidelberg, Berlin, in press.

## V. CONCLUSIONS

MR Spectroscopic Imaging-guided IMRT technique is being developed for the treatment of prostate cancer. A few important milestones have been achieved toward the general goal of the project. These include (i) implemented 3T prostate MRSI technique with J-resolved pulse sequence; (ii) development of a robust image registration procedure to map endorectal coil-based MRSI data onto treatment planning CT/MRI images; (iii) experimental validation of the image registration tools; (iv) phantom measurement of MRSI; (v) improvement of currently available inverse planning algorithm for MRSI-guided prostate IMRT. Integration and further refinement of the above tools are underway. It is expected these tools will greatly facilitate the planning, delivery, and quality assurance of the MRSI-guided prostate treatment.

**References:**

1. Bookstein FL. Thin plate splines and the decomposition of deformations. *IEEE Trans. Pattern Anal. Mach. Intell.* 11: 567-585, 1989.
2. DiBiase SJ, Hosseinzadeh K, Gullapalli RP, Jacobs SC, Naslund MJ, Sklar GN, Alexander RB, Yu CU-hwscsaBW-K-Dacbeef. Magnetic resonance spectroscopic imaging-guided brachytherapy for localized prostate cancer. *International Journal of Radiation Oncology, Biology, Physics* 52 (2): 429-438, 2002.
3. Hunjan S, Kim D, Adalsteinsson E, Daniel B, Dumoulin C, Boyer A, Spielman D, L X. Quality Assurance for MR Spectroscopic Imaging-Guided Prostate Therapy. *Medical Physics* 30 (June): 1321, 2003.
4. Hunjan S, Adalsteinsson E, Kim DH, Harsh GR, Boyer AL, Spielman D, Xing L. Quality assurance of magnetic resonance spectroscopic imaging-derived metabolic data. *International Journal of Radiation Oncology, Biology, Physics* 57 (4): 1159-73, 2003.
5. Kim D, Mayer D, Xing L, Daniel D, Spielman D. In vivo detection of citrate for prostate cancer at 3 Tesla. *Magnetic Resonance in Medicine* : submitted., 2004.
6. Kurhanewicz J, Vigneron DB, Hricak H, Narayan P, Carroll P, Nelson SJ, Kalbhen CL. Three-dimensional H-1 MR spectroscopic imaging of the in situ human prostate with high (0.24-0.7-cm3) spatial resolution prostate carcinoma: MR imaging findings after cryosurgery. *Radiology* 198 (3): 795-805, 1996.
7. Lian J, Hunjan S, Daniel B, Lo A, Levin J, Cardenas C, Dumoulin C, Watkins R, Rohling K, Giaquinto R, Boyer A, Xing, L. Mapping of the Prostate in Endorectal Coil-Based MRI/MRSI and CT: A Deformable Registration and Validation Study. *Medical Physics* 31: conditionally accepted, 2004.
8. Schreiber E, Hancock, S., Boyer, A, Daniel B, Spielman D., Xing L. Using finite element method for registering 3T MRSI/MRI with CT. manuscript in preparation, 2004.
9. Ling CC, Humm J, Larson S, Amols H, Fuks Z, Leibel S, Koutcher JAU-hwscsaBW-D-Safadfb. Towards multidimensional radiotherapy (MD-CRT): biological imaging and biological conformality. *International Journal of Radiation Oncology, Biology, Physics* 47 (3): 551-560, 2000.
10. Pickett B, Vigneault E, Kurhanewicz J, Verhey L, Roach M. Static field intensity modulation to treat a dominant intra-prostatic lesion to 90 Gy compared to seven field 3-dimensional radiotherapy. *International Journal of Radiation Oncology, Biology, Physics* 44 (4): 921-9, 1999.
11. Rosenman J. Incorporating functional imaging information into radiation treatment. *Seminars in Radiation Oncology* 11 (1): 83-92, 2001.
12. Schreiber E, Kim D, Hancock S, Boyer A, Spielman D, Daniel B, Xing L. Using Finite-Element Method to Register Endorectal Coil-Based MRI/MRSI with Treatment Planning CT Images. In: Annual Meeting of ASTRO, Atlanta, GA, 2004.
13. Xing L, Cotrutz C, Hunjan S, Boyer AL, Adalsteinsson E, Spielman DM. Inverse Planning for Functional Image-Guided IMRT. *Physics in Medicine & Biology* 47 (10): 3567-3578, 2002.
14. Zaider M, Zelefsky MJ, Lee EK, Zakian KL, Amols HI, Dyke J, Cohen G, Hu Y, Endi AK, Chui C, Koutcher JA. Treatment planning for prostate implants using magnetic-resonance spectroscopy imaging. *International Journal of Radiation Oncology, Biology, Physics* 47 (4): 1085-96, 2000.

---

## Appendix I. manuscripts published or submitted for publication (see attachment)

### Manuscripts:

1. Yong Y, Xing L, "Inverse planning with adaptively evolving voxel-dependent penalty scheme", *Medical Physics*, accepted.
2. Lian J, Hunjan S, Daniel B, Lo A, Levin J, Cardenas C, Dumoulin C, Watkins R, Rohling K, Giaquinto R, Boyer A, Xing, L. Mapping of the Prostate in Endorectal Coil-Based MRI/MRSI and CT: A Deformable Registration and Validation Study. *Medical Physics* 31: conditionally accepted, 2004..
3. Schreibmann E and Xing L, "Beam orientation class-solutions for IMRT prostate cancer treatment". *Medical Physics*, submitted.
4. Yang Y and Xing L, "Clinical knowledge-based inverse treatment planning". *International Journal of Radiation Oncology, Biology, Physics*, submitted.
5. Kim D, Mayer D., Xing L, Daniel B, Margolis, D., Spielman D., "In vivo detection of citrate for prostate cancer at 3 Tesla", *Magnetic Resonance Imaging in Medicine*, submitted.

### Book Chapters:

1. Xing L., Yang Y., Spielman D., Molecular/Functional Image-Guided Radiation Therapy, T. Bortfeld, R. Schmidt-Ullrich, W. de Neve (editors), Springer-Verlag Heidelberg, Berlin, in press.

# **Inverse Treatment Planning with Adaptively Evolving Voxel-Dependent Penalty Scheme**

Yong Yang, Ph.D. and Lei Xing<sup>a)</sup>, Ph.D.

Department of Radiation Oncology, Stanford University School of Medicine,  
Stanford, CA 94305-5847

Short title: Adaptive Voxel-Dependent Penalty Scheme for Inverse Planning

<sup>a)</sup> Author to whom correspondence should be addressed:

Department of Radiation Oncology  
Stanford University School of Medicine,  
Clinical Cancer Center  
875 Blake Wilbur Drive, Rm G-204  
Stanford, CA 94305-5847  
Telephone: (650) 498-7896  
Fax: (650) 498-4015  
Email: lei@reyes.stanford.edu

Submitted to: Medical Physics

## Abstract

In current inverse planning algorithms it is common to treat all voxels within a target or sensitive structure equally and use structure specific prescriptions and weighting factors as system parameters. In reality, the voxels within a structure are not identical in complying with their dosimetric goals and there exists strong intra-structural competition. Inverse planning objective function should not only balance the competing objectives of different structures but also that of the individual voxels in various structures. In this work we propose to model the intra-structural tradeoff through the modulation of voxel dependent importance factors and deal with the challenging problem of how to obtain a sensible set of importance factors with a manageable amount of computing. Instead of letting the values of voxel dependent importance to vary freely during the search process, an adaptive algorithm, in which the importance factors were tied to the local radiation doses through a heuristically constructed relation, was developed. The new planning tool was applied to study a hypothetical phantom case and a prostate case. Comparison of the results with that obtained using conventional inverse planning technique with structure specific importance factors indicated that the dose distributions from the conventional inverse planning are at best sub-optimal and can be significantly improved with the help of the proposed non-uniform penalty scheme.

**Key word:** IMRT, inverse planning, dose optimization, objective function, tradeoff.

## Introduction

Inverse treatment planning is an indispensable step in the implementation of IMRT and its performance critically determines the success of an IMRT treatment<sup>1-11</sup>. While the general concept of inverse planning seems to be logical and straightforward, much remains to be done to improve the currently available algorithms<sup>3, 12-14</sup>. One of the key issues that have been overlooked in the formulation of inverse planning problem is the intra-structural tradeoff. Indeed, in most, if not all, inverse planning algorithms, the dose prescription and weighting factors are specified on a structure specific basis. An implicit assumption made in these implementations is that all points within a structure are equivalent. In reality, voxels within a structure are generally not equivalent in complying with their dosimetric requirements and this inherent heterogeneity has not been considered so far. Depending on the patient's geometry, beam modality and field configuration, some regions in a patient may have better chance to meet the prescription than others. Furthermore, the doses at different regions are often incompatible and even compete each other. Appropriate tradeoff between the voxels is a requisition to fully exploit the potential of IMRT in any type of inverse planning techniques<sup>15-19</sup>.

In this work we propose to model the intra-structural tradeoff through the modulation of voxel dependent importance factors. The new inverse planning technique allows us to balance not only the competing objectives of different structures but also that of the individual voxels within any structure. Computationally, the determination of intra-structural tradeoff is an intensive task because of the coupling between the beamlet weights and local importance. To obtain an adequate set of local importance factors with a manageable amount of computing time, we develop an adaptive algorithm. The main idea of the adaptive approach is to heuristically link the values of the voxel-dependent importance factors with the corresponding radiation doses and to continuously update their values until the optimality criterion is met. The new planning technique has been applied to study a hypothetical phantom case and a prostate case and its advantage over the conventional inverse planning technique with structurally uniform importance has been demonstrated. The algorithm seems to afford an effective way of modeling the system with only a little computational overhead and shows significant promise to improve the existing inverse planning techniques.

## Methods and Materials

### *Theoretical background*

Clinical objectives are multifaceted and often incompatible with one another. The inverse planning is thus inherently a multi-objective problem: each anatomical structure, or more generally, each voxel within a structure, as an independent entity with its own treatment objective. A commonly used approach is to combine these objectives to form an overall objective function by weighted sum of the individual objectives. That is

$$F = \sum_{\sigma=1} r_{\sigma} F_{\sigma}(\{D_c(i)\}), \quad (1)$$

where the summation is over all targets and sensitive structures,  $D_c(i)$  is the calculated dose in voxel  $i$ , and  $r_{\sigma}$  and  $F_{\sigma}$  are the weighting factor (or the importance factor) and the objective of the structure indexed by  $\sigma$ , respectively. Regardless of the model used,  $F_{\sigma}$  can be expressed as a function of the dose distribution,  $\{D_c(i)\}$ , within the structure.

For a dose-based optimization, the quadratic form<sup>20 21, 22</sup>,

$$F_{\sigma} = \frac{1}{N_{\sigma}} \sum_{i=1}^{N_{\sigma}} r_i [D_c(i) - D_0(i)]^2, \quad (2)$$

is often used, where  $N_{\sigma}$  represents the total number of voxels in structure  $\sigma$ , and  $D_0(i)$  is the prescription dose in voxel  $i$ . In the above description, two types of weighting factors are involved: the inter-structural importance,  $\{r_{\sigma}\}$ , and the intra-structural ones,  $\{r_i\}$ . Up to this point, however, only structure specific importance factors are utilized in inverse planning formulation and the importance of voxel specific weighting factors has been overlooked other than the fact that they have been used to “tweak” IMRT dose distributions<sup>15-16,18</sup>. Indeed, in most, if not all, objective functions, the voxels within a structure are tacitly assumed to be equivalent in complying with their dosimetric requirements and their relative importance factors are set to unity. This type of penalty scheme seriously limits the solution space and often leads to sub-optimal plan. To give a comprehensive example, one can imagine the consequence when two or more structures in a system are restricted to take a single importance. To be able to assess more candidate plans and obtain truly optimal IMRT plans, it is necessary to establish a voxel dependent

penalty scheme in which the penalty at a voxel depends not only on the dose deviation from the prescription but also on other physical and clinical requirements at the point, which can be reflected by purposely modulating the  $\{r_i\}$ .

#### ***Voxel dependent importance factor and its heuristic relation to the local dose***

While the introduction of voxel dependent importance factors has the advantage for us to obtain IMRT solutions that would be otherwise not accessible, a practical question is how to determine the optimal importance distribution for a given structure. In reality, there may be more than one source that contribute to the voxel heterogeneity (for example, the in-equivalence of the voxels in complying their dosimetric goals as discussed in this work, or biological heterogeneity resulting from non-uniform cell density or radiation sensitivity distribution) and the local importance can be generally written as a product of the contributions from various sources, that is,  $r_i = r_i^1 r_i^2 r_i^3 \dots$ , where the superscripts index the different sources of contributions. A possible approach for obtaining the importance distribution is so called *a priori* technique, in which one attempts to identify the origin of voxel in-equivalence and then derives the spatial distribution of  $\{r_i\}$  based on physical or clinical considerations. One can also proceed in *a posteriori* fashion<sup>15-17</sup> by directly optimizing the  $\{r_i\}$ , similar to the auto-selection of the structure specific importance factors proposed by Xing et al<sup>17</sup>. An optimization of the intra-structural tradeoff is likely to be computationally prohibitive due to the enormous size of the search space arising from the coupling of the beamlet weights and the local importance factor. To circumvent the problem, in this work we develop an alternative technique in which the importance distribution is determined adaptively under the guidance of a heuristically constructed function.

Intuitively, it is not difficult to conceive that the  $r_i$  in equation (2) can be regarded as a dose dependent parameter. For a voxel in a sensitive structure, for instance, the value of  $r_i$  should be higher if the voxel receives a high dose so that the voxel gets more penalty, and *vice versa*. This suggests that the local importance can be expressed as a function of the local dose and updated at each step of the iterative dose optimization process without invoking any additional computation. While the general monotonic dependence of  $r_i$  on the dose is clear, its specific form is a matter of experimentation. We propose



$$r_i = a_0 + a_1 D_c(i)^k \quad (3)$$

for the application, where  $a_0$ ,  $a_1$ , and  $k$  are heuristic structure specific parameters. The value of  $k$  is greater than zero for a voxel in a sensitive structure. For a voxel in a target,  $k$  should be less than zero in order to assimilate the clinical preference over overdosing versus underdosing. The penalty function for a structure consists essentially two terms. The first term is the conventional one with uniform importance across the whole structure and the second term modulates the importance according to the local value of dose. This phenomenological importance emphasizes on penalizing those voxels receiving a high radiation dose yet does not ignore those voxels with intermediate and even low dose of radiation at each step of the iterative calculation. In this study, we set  $a_0$  as unity and  $a_1$  as  $D_{ref}^{-k}(i)$ , where  $D_{ref}(i)$  is set as the 5% tolerance dose  $TD_{5/5}$  for sensitive structures and prescription dose  $D_0(i)$  for target.  $k$  is an adjustable parameter determined by a trial-and-error process. We emphasize that the  $\{r_i\}$  distribution so obtained may not be the best possible distribution due to the restriction on the feasible values imposed by equation (3). However, as will be seen in the Results section, the non-uniform importance factors resulted from the use of equation (3) allow us to significantly improve the IMRT dose distributions obtained using the existing inverse planning algorithm based on structure specific importance factors. The technique thus provides a practical solution to what appears to be a computationally overwhelming problem.

### *Calculation process*

An independent optimization module based on the objective function (2) (with  $\{r_i\}$  determined by equation (3)) was integrated into the PLUNC treatment planning system (University of North Carolina, Chapel Hill, NC). The dose calculation engine and varieties of evaluation tools existing in the PLUNC system were employed for this study. For a given patient, a set of structure specific importance factors,  $\{r_\sigma\}$ , were determined empirically, similar to that in the conventional inverse planning. For a given set of  $\{r_\sigma\}$ , we used the ray-by-ray iterative algorithm (SIITP) reported in References<sup>23, 24</sup> to obtain the optimal beam intensity profiles. The only difference here is that a  $r_i$ -modulated quadratic objective function was used. The calculation time for a typical prostate case is

less than 5 minutes on a PC with P4 1.7GHz and 1024MB RAM.

### ***Case Studies***

A hypothetical phantom case and a previously treated clinical prostate case were used to evaluate the level of improvement resulted from the new algorithm with adaptively determined spatially non-uniform importance factors. The results for both cases were compared with that obtained using the conventional dose optimization method with structural specific importance factors. For the purpose of plan comparison and assessment, we purposely adjusted the structure specific importance factors in such a way that the dose coverage of the target volume was similar for the two IMRT plans.

The phantom case consisted of a target and a sensitive structure (figure 1a). Five incident beams were used for target irradiation ( $32^\circ$ ,  $104^\circ$ ,  $176^\circ$ ,  $248^\circ$  and  $320^\circ$  in IEC convention). The incident photon energy is 15 MV. Table I listed the optimization parameters for both the approaches for this case. The target was prescribed to 100 (arbitrary unit) and the prescription dose to the sensitive structure,  $D_0(i)$  in equation (2), was set to zero.

In the prostate IMRT case, the target volume was the prostate. The sensitive structures involved in this study were rectum, and bladder. Five equally spaced 15MV photon beams (gantry angles of  $0^\circ$ ,  $72^\circ$ ,  $144^\circ$ ,  $216^\circ$ , and  $288^\circ$  in IEC convention) were used for the treatment. A radiation dose of 70Gy was prescribed to cover 99% of the target volume. For the sensitive strictures, the prescription doses to the sensitive structures,  $D_0(i)$  in equation (2), were set to zero. The optimization parameters for both approaches were summarized in Table II.

## **Results and Discussion**

### ***Hypothetical phantom IMRT plans***

Figures 1 and 2 summarized the calculation results and the comparison of the two IMRT plans obtained using the newly proposed and conventional penalty schemes. In figure 1a we depict the geometry of the phantom and in figures 1b and 1c we show the isodose

distributions for the plans without and with the use of non-uniform intra-structural importance factors. The DVHs of the target and sensitive structure are plotted in figure 2. The dashed and solid curves in figure 2 represent the results of the conventional and the newly proposed inverse planning approaches, respectively. It is clearly seen that the proposed technique greatly improves the critical structure sparing. The maximum dose to the sensitive structure is reduced from 67 to 61 and the doses to other voxels in the sensitive structure are all reduced by 2~14%. The fractional volume reduction in the intermediate and low doses is more distinct. For example, the fraction volume receiving dose above 40 is decreased from 19% to 10% while that receiving dose above 20 is decreased from 95% to 51%. For target, the volume receiving dose above 85 is similar for the two algorithms, 98.4% and 98.6% for the conventional and the new approaches, respectively. However, the volume receiving high doses is decreased (e.g., the fractional volume receiving a dose above 102 is reduced from 20.7% to 8.2%). Interestingly, the irradiation to the normal tissue surrounding the target and sensitive structure seems to be less in the new optimization technique. For example, the fraction volumes of the normal tissue that received doses above 60 and 40 are decreased from 12% to 8% and from 34% to 25%, respectively. We attribute the simultaneous improvement in the doses of all structures to the greatly enlarged solution space when non-uniform importance is permissible.

### ***Prostate IMRT plans***

The IMRT plans obtained using the two different approaches for the prostate case are summarized in figures 3 and 4. Figure 3 compares the isodose distributions in two transverse slices and one sagittal slice for the two plans. The DVHs of the target and the sensitive structures for the two plans are plotted in figure 4, in which the dashed lines represent the results obtained using the conventional algorithm and the solid lines the newly proposed approach. Similar to the phantom case, when non-uniform importance factors are permissible, the conformality of the final dose distribution is greatly improved in comparison with the conventional IMRT planning with structurally uniform importance factors. In particular, the doses to the sensitive structures are dramatically improved. As can be seen from figure 3, much steeper dose gradients at the interface

between the target and the sensitive structures are achieved. From the DVHs, it is observed that the rectum and bladder are better spared. For example, the fractional volume of the rectum that receives a dose above 40Gy is dropped from 36.5% to 10.5%. Similarly, 10% reduction (from 30.5% to 20.5%) is noticed in the fractional bladder volume receiving a dose above 30Gy. The integral dose to the normal tissue is, once again, reduced as a consequence of the use of non-uniform importance factors. It is important to emphasize that the improvement in sensitive structure sparing is achieved with essentially no change in the dose coverage of the tumor target. For the target, the fractional volume receiving dose below 70 Gy is decreased from about 2.1% to 1.2% and the fractional volume receiving dose above 80 Gy is decreased from 2.4% to 1.5%. The maximum doses for the two plans are almost same, 81.2Gy and 81.4Gy, respectively. But the minimum dose is increased from 63.4Gy for the conventional inverse planning to 65.5Gy for the new technique.

Finally, it is interesting to point out that the EUD-based optimization<sup>25-27</sup> is a special case of the empirical model proposed in this work. If we ignore the contribution from the dose discrepancy penalty part in Eq. (2) (*i.e.*, change the power of the dose discrepancy in Eq. (2) from 2 to 0), the objective function (2) with  $r_i$  given by Eq. (3) becomes a function of EUD. Generally speaking, the formalism proposed here is a hybrid of dose-based and EUD-based functions. Practically, the optimization problem here is formulated at a voxel level in dose domain while the EUD-based formalism works at a structural level in EUD domain. The voxel level information, such as non-uniform biology data in target and/or sensitive structures, can be more easily integrated into the objective function proposed here. In addition, prescription and evaluation of a treatment plan in dose domain other than in EUD domain makes the proposed method clinically more practical.

## Conclusion

Inverse planning is essentially to balance the competing dosimetric or clinical requirements of the individual elements in a given system. The level of optimality of the

final IMRT treatment plan depends not only on the performance of the optimization algorithm but also, more fundamentally, on the way that the tradeoff between different competing elements is defined. While a voxel in a patient is the smallest dosimetric element, the tradeoff in current inverse planning algorithm is being done implicitly on an organ or structure level. In this work, we have shown that this type of tradeoff scheme is deficient and seriously limits the solution space. Furthermore, we proposed a model for the tradeoff of different voxels through the modulation of voxel dependent importance factors. A novel inverse planning algorithm with adaptively determined local importance factors was described. A comparison with the conventional inverse planning technique indicated that the new tradeoff strategy substantially improves the IMRT dose distributions and allows us to obtain solutions that would otherwise be unattainable.

#### **Acknowledgement**

We wish to thank Dr. Zhengyu Shou for useful discussions. The supports from the National Cancer Institute (1 R01 CA98523-01) and Department of Defense (DAMD17-03-1-0023) are gratefully acknowledged.

## References

- 1 T. Bortfeld. Optimized planning using physical objectives and constraints. *Seminars in Radiation Oncology* 1999; 9: 20-34
- 2 S. V. Spirou and C. S. Chui. A gradient inverse planning algorithm with dose-volume constraints. *Medical Physics* 1998; 25: 321-333
- 3 G. Intensity Modulated Radiation Therapy Collaborative Working. Intensity-modulated radiotherapy: current status and issues of interest. *International Journal of Radiation Oncology, Biology, Physics* 2001; 51: 880-914
- 4 R. Mohan, G. S. Mageras, B. Baldwin, L. J. Brewster, G. J. Kutcher, S. Leibel, C. M. Burman, C. C. Ling and Z. Fuks. Clinically relevant optimization of 3-D conformal treatments. *Medical Physics* 1992; 19: 933-944
- 5 L. Xing, C. Cotrutz, S. Hunjan, A. L. Boyer, E. Adalsteinsson and D. Spielman. Inverse planning for functional image-guided intensity-modulated radiation therapy. *Phys Med Biol* 2002; 47: 3567-3578.
- 6 A. Brahme. Optimized radiation therapy based on radiobiological objectives. *Seminars in Radiation Oncology* 1999; 9: 35-47
- 7 J. O. Deasy. Multiple local minima in radiotherapy optimization problems with dose-volume constraints. *Medical Physics* 1997; 24: 1157-1161
- 8 Y. Xiao, J. Galvin, M. Hossain and R. Valicenti. An optimized forward-planning technique for intensity modulated radiation therapy. *Medical Physics* 2000; 27: 2093-2099
- 9 S. Webb. Optimization by simulated annealing of three-dimensional conformal treatment planning for radiation fields defined by a multileaf collimator. *Physics in Medicine & Biology* 1991; 36: 1201-1226
- 10 D. Michalski, Y. Xiao, Y. Censor and J. Galvin. The dose-volume constraint satisfaction problem for inverse treatment planning with field segments. *Physics in Medicine and Biology* 2004; 49: 601-616
- 11 S. Gaede, E. Wong and H. Rasmussen. An algorithm for systematic selection of beam directions for IMRT. *Med. Phys.* 2004; 31: 376-388

- 12 T. Bortfeld, C. Thieke, K. H. Kufer and H. Trinkaus. New Approaches in Intensity-Modulated Radiotherapy. ICRO Meeting. Monduzzi Editore, 2002; 251-258
- 13 H. I. Amols and C. C. Ling. EUD BUT NOT QUD. International Journal of Radiation Oncology, Biology, Physics 2002; 52: 1-2
- 14 C. Yeboah, G. A. Sandison and V. Moskvina. Optimization of intensity-modulated very high energy (50-250 MeV) electron therapy. Physics in Medicine and Biology 2002; 47: 1285
- 15 C. Cottruz and L. Xing. IMRT dose shaping with regionally variable penalty scheme. Med Phys 2003; 30: 544-551.
- 16 C. Cottruz and L. Xing. Using voxel-dependent importance factors for interactive DVH-based dose optimization. Phys Med Biol 2002; 47: 1659-1669.
- 17 L. Xing, J. G. Li, S. Donaldson, Q. T. Le and A. L. Boyer. Optimization of importance factors in inverse planning. Physics in Medicine & Biology 1999; 44: 2525-2536
- 18 C. Wu, G. H. Olivera, R. Jeraj, H. Keller and T. R. Mackie. Treatment plan modification using voxel-based weighing factors/dose prescription. Physics in Medicine & Biology 2003; 48: 2479-2491
- 19 Y. Chen, D. Michalski, C. Houser and J. M. Galvin. A deterministic iterative least-squares algorithm for beam weight optimization in conformal radiotherapy. Physics in Medicine & Biology 2002; 47: 1647-1658
- 20 G. Starkschall. A constrained least-squares optimization method for external beam radiation therapy treatment planning. Medical Physics 1984; 11: 659-665
- 21 T. Holmes and T. R. Mackie. A comparison of three inverse treatment planning algorithms. Physics in Medicine & Biology 1994; 39: 91-106
- 22 D. H. Hristov and B. G. Fallone. An active set algorithm for treatment planning optimization. Med Phys 1997; 24: 1455-1464.
- 23 L. Xing and G. T. Y. Chen. Iterative algorithms for Inverse treatment planning. Physics in Medicine & Biology 1996; 41: 2107-2123
- 24 L. Xing, R. J. Hamilton, D. Spelbring, C. A. Pelizzari, G. T. Chen and A. L. Boyer. Fast iterative algorithms for three-dimensional inverse treatment planning. Medical Physics 1998; 25: 1845-1849

- 25     A. Niemierko. Reporting and analyzing dose distributions: a concept of equivalent uniform dose. *Medical Physics* 1997; 24: 103-110
- 26     Q. Wu, R. Mohan, A. Niemierko and R. Schmidt-Ullrich. Optimization of intensity-modulated radiotherapy plans based on the equivalent uniform dose. *Int J Radiat Oncol Biol Phys* 2002; 52: 224-235.
- 27     C. Thieke, T. Bortfeld, A. Niemierko and S. Nill. From physical dose constraints to equivalent uniform dose constraints in inverse radiotherapy planning. *Med Phys* 2003; 30: 2332-2339.



**Table I** Summary of the optimization parameters used in the conventional and newly proposed approaches for the hypothetical phantom case

Organs	The dose-based approach		The proposed approach		
	Importance factors ( $r_o$ )	Prescription or tolerance doses (%)	Importance factors ( $r_o$ )	$D_{ref}(\%)$	$k$
Target	8.0	100	15.0	100	-4
Critical Structure	5.0	35	0.6	45	10
Normal tissue	1.0	70	0.5	70	2

**Table II** Summary of the optimization parameters used in the conventional and newly proposed approaches for the prostate case

Organs	The dose-based approach		The proposed approach		
	Importance factors ( $r_o$ )	Prescription or tolerance doses (Gy)	Importance factors ( $r_o$ )	$D_{ref}$ (Gy)	$k$
Target	4.0	70	5.0	70	-5
Bladder	1.0	50	0.1	65	2
Rectum	1.0	45	0.3	60	8.3
Normal tissue	0.5	65	0.4	68	2

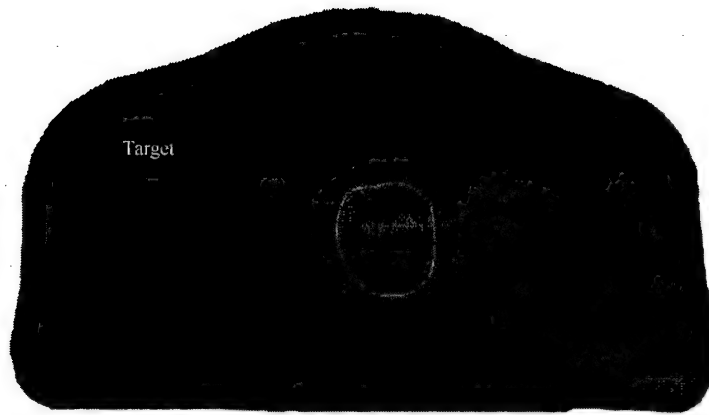
## Captions

Fig. 1. The comparison of the isodose distributions for the hypothetical phantom case: (a) the geometry of the phantom; and (b) dose distribution obtained using structurally uniform importance factors; (c) dose distribution obtained using the newly proposed algorithm with structurally non-uniform importance factors.

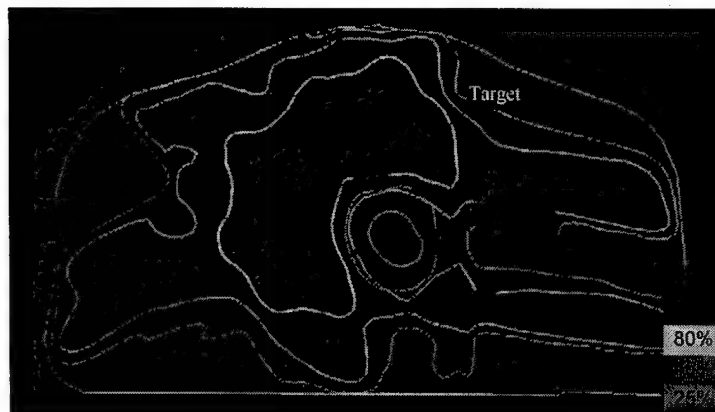
Fig. 2. Comparison of the Dose Volume Histograms (DVH) for IMRT plans obtained using our newly proposed algorithm (solid curves) and the conventional algorithm (dash lines).

Fig. 3. Comparison of the isodose distributions for the prostate IMRT plans: (a) dose distribution obtained using structurally uniform importance factors; (b) dose distribution obtained using the newly proposed algorithm with structurally non-uniform importance factors. The results on two transverse slices, and one sagittal slice are shown.

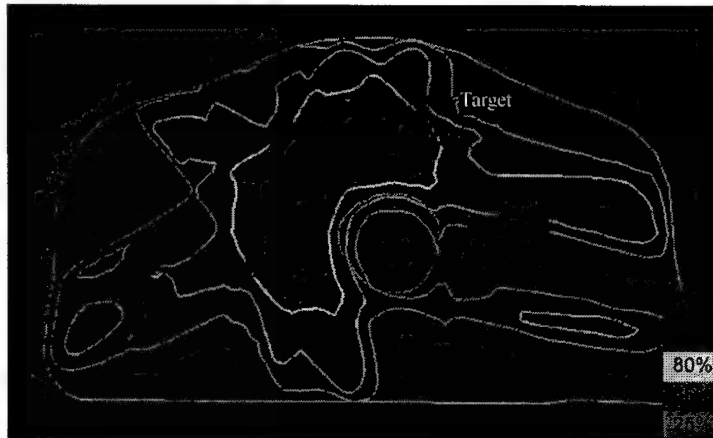
Fig. 4. Comparison of the Dose Volume Histograms (DVH) for the prostate IMRT plans obtained using our newly proposed algorithm (solid curves) and the conventional algorithm (dash lines).



(a)



(b)



(c)

Figure 1

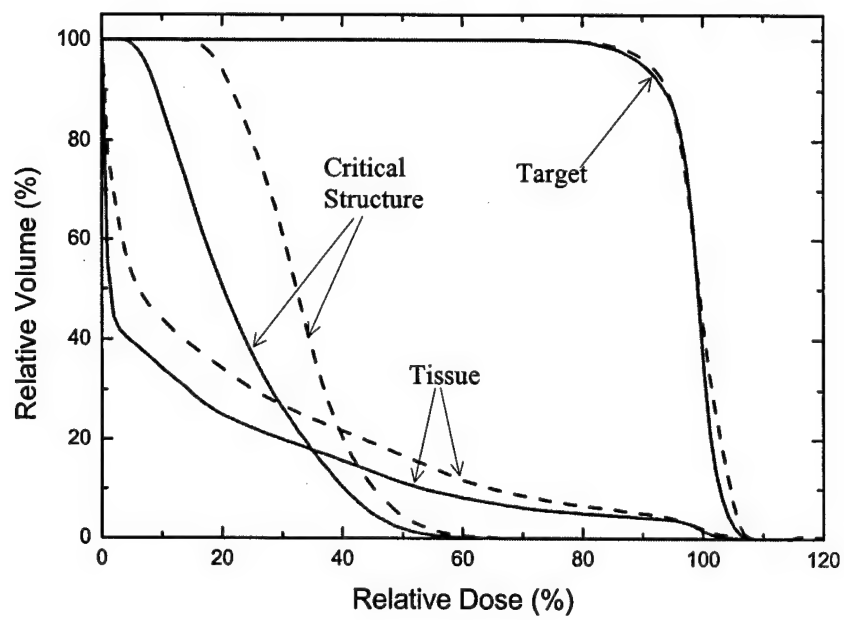
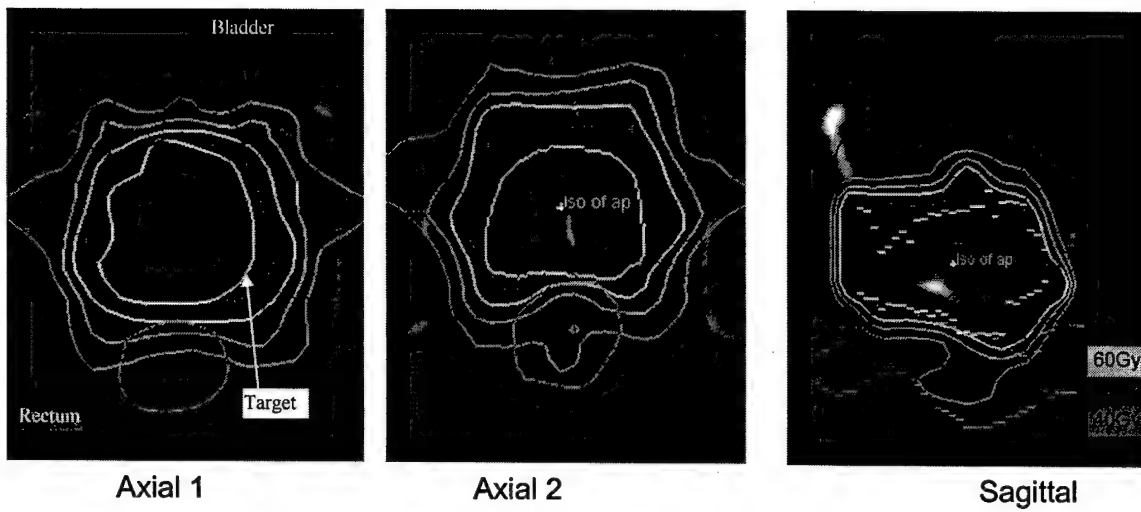
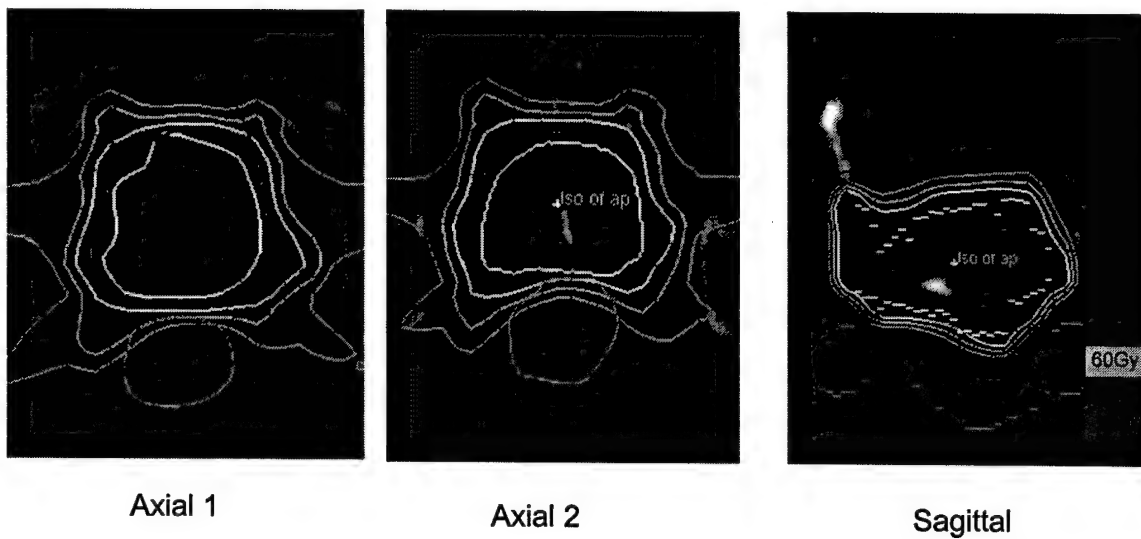


Figure 2



(a)



(b)

Figure 3

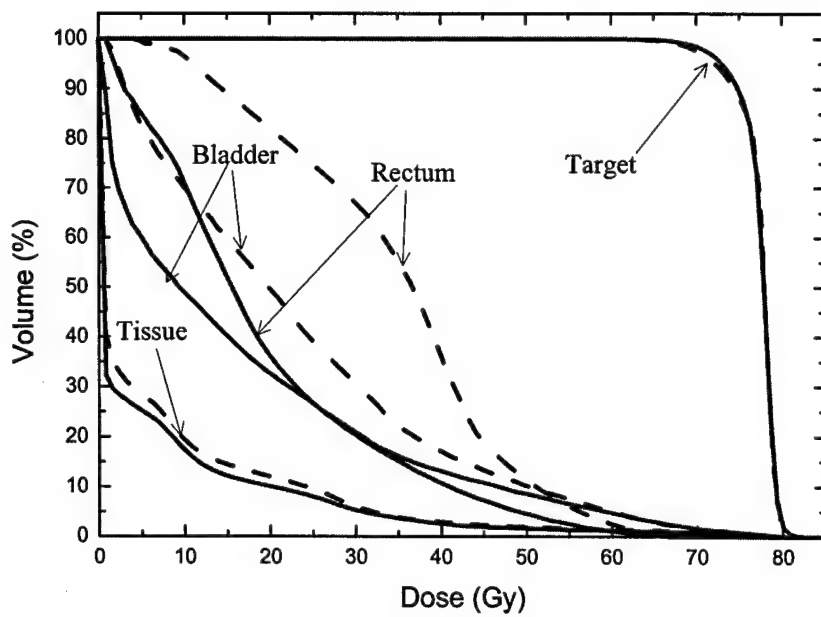


Figure 4

# **Mapping of the Prostate in Endorectal Coil-Based MRI/MRSI and CT: a Deformable Registration and Validation Study**

J. Lian<sup>1</sup>, L. Xing<sup>1</sup>, S. Hunjan<sup>1</sup>, C. Dumoulin<sup>3</sup>, J. Levin<sup>2</sup>, A. Lo<sup>1</sup>, R. Watkins<sup>3</sup>, K. Rohling<sup>3</sup>, R. Giaquinto<sup>3</sup>, D. Kim<sup>2</sup>, D. Spielman<sup>2</sup>, B. Daniel<sup>2</sup>

<sup>1</sup>Department of Radiation Oncology, <sup>2</sup>Department of Radiology, Stanford University School of Medicine, 300 Pasteur Drive, Stanford, California, CA 94305

<sup>3</sup>GE Corporate Research and Development Center, Schenectady, NY 12309

Corresponding author:  
Lei Xing, Ph.D.  
Stanford University School of Medicine  
Department of Radiation Oncology  
300 Pasteur Drive, A038  
Stanford, CA 94305-5304

E-mail: lei@reyes.stanford.edu  
Phone: (650) 498 7896  
Fax: (650) 498 4015

## Abstract

The endorectal coil is being increasingly used in magnetic resonance imaging (MRI) and MR spectroscopic imaging (MRSI) to obtain anatomic and metabolic images of the prostate with high signal-to-noise ratio (SNR). In practice, however, the use of endorectal probe inevitably distorts the prostate and other soft tissue organs, making the analysis and the use of the acquired image data in treatment planning difficult. The purpose of this work is to develop a deformable image registration algorithm to map the MRI/MRSI information obtained using an endorectal probe onto CT images and to verify the accuracy of the registration by phantom and patient studies. A mapping procedure involved using a thin plate spline (TPS) transformation was implemented to establish voxel-to-voxel correspondence between a *reference* image and a *floating* image with deformation. An elastic phantom with a number of implanted fiducial markers was designed for the validation of the quality of the registration. Radiographic images of the phantom were obtained before and after a series of intentionally introduced distortions. After mapping the distorted phantom to the original one, the displacements of the implanted markers were measured with respect to their ideal positions and the mean error was calculated. In patient studies, CT images of two prostate patients were acquired, followed by 3 Tesla (3T) MR images with a rigid endorectal coil. Registration quality was estimated by the centroid position displacement and image coincidence index (CI). Phantom studies show that using the deformable registration method the mean landmark displacement error was  $0.62 \pm 0.39$  mm when the distortion was of the order of 23.07 mm. When a non-deformable method based on a rigid-body transformation and scaling was used for the same distortion, the mean displacement of the fiducials with respect to



their actual positions was found to be as large as  $12.95 \pm 0.57$  mm. For both patient studies, significantly improved registration accuracy was also achieved. The prostate centroid position displacement was  $0.58 \pm 0.10$  mm and the CI was  $92.6 \pm 5.1$  % when a TPS transformation was used. Different from the non-deformable approach, the TPS-based registration accommodates the organ distortion and enables us to achieve significantly higher MR/MRSI and CT image registration accuracy. The technique should be useful to map the MR spectroscopic dataset acquired with ER probe onto the treatment planning CT dataset to guide radiotherapy planning.

## 1. Introduction

The introduction of endorectal (ER) surface coils significantly improves the spatial resolution and signal-to-noise ratio (SNR) of prostate MR and MR spectroscopic imaging<sup>1-8</sup>. The new MRI/MRSI tool provides an unprecedented means for us to characterize the location(s) and volume(s) of intraprostatic lesion(s) and to evaluate the possible capsular penetration, invasion of neurovascular bundle, and seminal vesicle involvement<sup>2-4, 9-13</sup>. The information derived from the new imaging modality is also valuable for guiding radiation therapy treatment planning to escalate radiation doses according to the regional tumor burden<sup>14-18</sup>. In practice, the use of ER coil severely distorts the prostate and surrounding organs. On the other hand, current radiation treatment planning is performed on the CT images without distortion. In order to use ER-based image data to guide radiation therapy treatment planning, it is imperative to develop a method to map the information in the ER-based MRI/MRSI to the corresponding location in CT images. Zaider et al (2000) and Mizowwki et al (2002) have reported a translation and scaling based registration method to map MRS positive volumes onto the CT and ultrasound images. In their approach, the coordinates of the boundary and the center of mass were used to linearly interpolate the positions of the mapped voxels. Although a clinically acceptable mean difference (2.4 mm) between the predicted and measured positions was reported, larger discrepancy was found for regions with more severe distortion ( $\geq 4\text{mm}$ ).

The purpose of this paper is to apply thin plate spline (TPS) -based deformable registration to improve the previously reported nondeformable MRS and CT mapping

technique and test the registration accuracy using a series of phantom measurements. The TPS transformation is a well-established mathematical method and its central idea is to find a continuous transformation to minimize the difference between the control points in two images. Since its first introduction into medical image analysis (Bookstein 1989), the TPS has been successfully used on several applications. A two step registration scheme (rigid body registration and TPS warping) was employed to make comparisons of MR images in interventional MRI guided radiofrequency ablation to determine whether a tumor is adequately treated <sup>19,20</sup>. In order to map changes in the shape and position of the liver between inhale and exhale breath held CT models of a patient, a mutual information (MI) based alignment with TPS warping was proposed <sup>21</sup>. A TPS transformation based technique has also been found useful to correct image distortion in fluoroscopic images <sup>22</sup>.

## **2. Methods and materials**

### **2.1. Image Mapping Method**

The prostate volumes in CT and MRI were first contoured by an experienced oncologist. The rotation operator was applied to adjust the relative tilt between two volumes. The axial slices of CT and MR data set were resampled using 1 mm interval. We aligned CT and MR slices with reference to the apex and base of the glands. Four to eight control points were placed in each pair of slices. The control points were only put along the contour of the gland and they are featured points such as corners and intersections of edges. Lastly the TPS transformation was applied on each pair of slices to establish a mapping relationship between voxels of MRI and CT. For convenience,

henceforth, the non-distorted CT volume is referred to as the *reference* and the distorted MRI the *floating* dataset.

The detailed description of the TPS transformation can be found in Bookstein's paper<sup>23</sup>. Here we briefly summarize the computational procedure.

(1) Assume  $P_1 = (x_1, y_1)$ ,  $P_2 = (x_2, y_2), \dots, P_n = (x_n, y_n)$  are the  $n$  control points in the *reference* image. The distance between point  $i$  and  $j$  is given by  $r_{ij} = |P_i - P_j|$ .

Define matrices

$$P = \begin{bmatrix} 1 & x_1 & y_1 \\ 1 & x_2 & y_2 \\ \dots & \dots & \dots \\ 1 & x_n & y_n \end{bmatrix},$$

$$K = \begin{bmatrix} 0 & U(r_{12}) & \dots & U(r_{1n}) \\ U(r_{21}) & 0 & \dots & U(r_{2n}) \\ \dots & \dots & \dots & \dots \\ U(r_{n1}) & U(r_{n2}) & \dots & 0 \end{bmatrix},$$

and

$$L = \begin{bmatrix} K & P \\ P^T & O \end{bmatrix}$$

where  $O$  is a  $3 \times 3$  matrix of zeros and  $U$  is a basis function  $U(r) = r^2 \log r^2$ .

(2) Let  $Q_1 = (u_1, v_1)$ ,  $Q_2 = (u_2, v_2)$ , ...,  $Q_n = (u_n, v_n)$  be  $n$  corresponding control points in the *floating* image. We construct matrices

$$V = \begin{bmatrix} u_1 & u_2 & \dots & u_n \\ v_1 & v_2 & \dots & v_n \end{bmatrix},$$

$$Y = (V \mid 0 \ 0 \ 0)^T.$$

The weighting vector  $W = (w_1, w_2, \dots, w_n)$  and the coefficients  $a_1$ ,  $a_u$ , and  $a_v$  can be computed by the equation

$$L^{-1}Y = (W \mid a_1 \ a_u \ a_v)^T.$$

(3) Use the elements of  $L^{-1}Y$  to define a function  $f(u', v')$  everywhere in the plane

$$f(u', v') = a_1 + a_u u + a_v v + \sum_{i=0}^n w_i U(|Pi - (u, v)|).$$

This function transforms a voxel in the *floating* volume to a new coordinate in the *reference* volume. The computation of the TPS transformation is rather efficient. In our experiment, it took around 5 seconds to compute a  $520 \times 520$ -pixel, 8-control point transformation on a Personal Computer (PC) with Intel Pentium® II 400Mhz CPU (Intel Corporation, Sunnyvale, CA) and 256MB memory.

For comparison purpose, we also implemented the non-deformable registration method reported by Zaider *et al* (2000) and Mizowaki *et al* (2002). For a particular voxel in the MR space (coordinate  $z_1$ ), the  $z$  coordinate in the US/CT space was obtained from:

$$\frac{z_1 - z_{C1}}{z_{T1} - z_{B1}} = \frac{z_2 - z_{C2}}{z_{T2} - z_{B2}},$$

where  $z_{T1}$  and  $z_{T2}$  are the coordinates of the superior aspects of the prostate in the MR and US/CT volume, respectively,  $z_{B1}$  and  $z_{B2}$  refer to the  $z$  coordinates of the inferior aspects of the prostate, respectively, and  $z_{C1}$  and  $z_{C2}$  represent the  $z$  coordinates of the prostate centroid in the MR space and US/CT space, respectively. Similarly, the  $(x, y)$  coordinates were mapped as follows:

$$\frac{y_{A1} - y_{P1}}{y_{A1} - y_1} = \frac{y_{A2} - y_{P2}}{y_{A2} - y_2}$$

$$\frac{x_{L1} - x_{R1}}{x_{L1} - x_1} = \frac{x_{L2} - x_{R2}}{x_{L2} - x_2}$$

Here,  $y_A$  and  $y_P$  are the y coordinates of the anterior and posterior aspects of the prostate, respectively, and  $x_L$  and  $x_R$  refer to, respectively, the x coordinates of the left and right aspects of the prostate. The results obtained by using this method and the newly developed TPS method were quantitatively compared in the phantom and patient studies.

## 2.2. Phantom Construction and Imaging

Tissue equivalent bolus material was used to construct the 2D phantoms which simulate the axial sections of the patient dataset. The bolus, made of vinyl gel, is elastic and has a density close to that of water. Ten to fifteen metal fiducial landmarks were embedded into each phantom. The phantoms were held in a custom made plastic holder, allowing them to be constricted and deformed in specifically chosen regions (Fig.1). The radiographic images were then acquired in anterior-posterior (AP) and lateral (LT) direction using a Ximatron Radiotherapy Simulator (Varian Medical Systems, Palo Alto, CA). An analysis of the AP/LT images for each phantom revealed the geometric locations of the fiducial markers before and after the distortion.

## 2.3. Patient Image Acquisition

Patient MRI was acquired on a 3-Tesla MR scanner (Signa; GE Medical Systems, Milwaukee, WI). RF excitation was achieved by using the whole body birdcage resonator, and the MR signal was received using a 4-element phased-array antenna (G.E.

Medical Systems, Milwaukee, WI) combined with a rigid single loop receiver-only surface coil with a fixed geometry that enables optimal tuning and matching for use at 3T. The coil dimensions are similar to trans-rectal ultrasound transducers used for routine sonographically-guided prostate imaging and biopsy. The ER-induced distortion of MRSI is very close to that of MRI. We show MR image in this study because they have higher image quality than MRSI. Patient CT images were acquired using a PQ5000 CT Scanner (Philips Medical Systems, Cleveland, OH).

#### 2.4. Validation of the Image Registration

For phantom studies, the control points were chosen only in the periphery for the registration of the *floating* and *reference* images. The inserted landmarks were used to trace the displacement and verify the registration accuracy. After mapping the distorted phantom to the original one, the displacements of the implanted markers were measured with respect to their ideal positions and the mean discrepancy was calculated for each phantom. The mean landmark displacement (MLD) was used as a metric for evaluating the quality of the registration.

For patient studies, typically 6-8 control points were chosen along the contour of the prostate based on the pronounced anatomical feature. Patient MR and CT registration accuracy was estimated by using the centroid position displacement of the prostate and the coincidence index (CI) defined by

$$CI(R, F) = \frac{\int_{\Omega} F(\bar{x})R(\bar{x})d\bar{x}}{\int_{\Omega} \max\{F(\bar{x}), R(\bar{x})\}d\bar{x}}$$

where CI is unity when two structures overlap exactly and zero when they are completely disjointed<sup>24</sup>. The *floating* (F) image and the *reference* (R) images were converted to

binary for the calculation. The use of CI provided us with an effective measure of the similarity between the warped *floating* (F) image and the *reference* (R) image. In both evaluations the tissue density was assumed to be homogenous.

### 3. Results

#### 3.1. Phantom studies

We first studied the dependence of registration accuracy on the number of control points. An elastic phantom with dimension  $5.5 \times 5.5 \times 1 \text{ cm}^3$  was used here. The phantom was distorted by the insertion of an object in the holder (Fig. 2A left) and it restored to the original shape when the object was removed (Fig. 2A right). When four control points were selected along the margin (Fig. 2B left), we obtained the warped image shown in the middle column. To evaluate the TPS algorithm, we computed the difference between the TPS predicted and the true image (Fig. 2B right panel). The MLD was found to be  $1.51 \pm 0.49 \text{ mm}$ . It is seen that the implanted landmarks do not coincide well in the two images. Next we added two more control points in the periphery and the corresponding mapped image shows reduced registration error with MLD down to  $0.76 \pm 0.54 \text{ mm}$  (Fig. 2C). When eight control points were selected, the MLD was further reduced to  $0.46 \pm 0.34 \text{ mm}$  and no significant landmark displacement was found in the difference image (Fig. 2D). In Fig. 2E we summarized the MLDs when four, six and eight control points were used in the warping calculation. The use of more control points resulted in higher registration accuracy. In practice, however, increasing the number of control points requires additional manual interaction and prolongs the registration process. In the following studies, six to eight pairs of control points were selected for the



TPS registration. We also mapped the distorted phantoms onto the *reference* images using a rigid-body registration and scaling based method <sup>17, 25</sup>. The non-deformable registration resulted in a  $2.50 \pm 0.83$  mm MLD when the maximum displacement was 4.2 mm. Hence, in the situation of a 4.2 mm distortion, the TPS method with eight control points yielded an MLD that was only 18.4% of the MLD obtained with the non-deformable model (0.46 versus 2.50 mm).

In the next level of validation we tested the algorithm with a larger rectangular phantom ( $9.2 \times 5.1 \times 1$  cm) to allow more flexible distortions. The *reference* image is shown in Fig. 3A. The *floating* images under a few different levels of distortions are shown in the left columns of B, C and D. Eight control points were used here to register the *floating* and *reference* images. The middle panels of B, C and D show the results after the TPS transformation. The differences between the TPS predictions and *references* are shown on the right panels of B, C and D. The quality of the TPS mapping was accessed by using the maximum and mean landmark displacement (MLD). As summarized in Table 1, for the distortion shown in Fig. 3A, the non-deformable registration gave a MLD of  $4.62 \pm 2.71$  mm, whereas the deformable registration reduced the error down to  $0.45 \pm 0.53$  mm. For the studies shown in Fig. 3C and D, the non-deformable registration yielded MLDs to  $7.35 \pm 4.20$  mm and  $12.95 \pm 6.57$  mm, respectively. The application of the deformable warping module significantly improved the mapping and led to MLDs of  $0.57 \pm 0.49$  mm and  $0.62 \pm 0.39$  mm, respectively. The largest registration error between the TPS prediction and the ideal situation were found to be 1.09 mm, 1.05 mm and 0.99 mm, respectively, for the three phantom distortions.

In order to examine the consistency of the registration, we inversed the previous transformation procedure by transforming the TPS-warped images (Fig.3 B, C and D middle panels) back to the distorted *floating* images. The calculation results are shown in the left columns of Fig.4 A, B and C. The difference images between them and the original deformed phantom images (the left columns of Fig. 3) are shown in the right panels. The resultant overlap of fiducial points was excellent in all three cases, suggesting the TPS is capable of generating consistent good mapping independent of the starting images. The MLDs for the three groups were  $0.23 \pm 0.08$ ,  $0.23 \pm 0.18$  and  $0.20 \pm 0.11$  mm, respectively. Maximum landmark registration discrepancies were found to be 0.35, 0.50 and 0.31 mm, respectively (Fig. 4 D).

### 3.2. Patient studies

We first studied where the distortion most likely happens in the ER-based MR images. After target segmentation and rotation operation, we compared the dimensions of the prostate in the datasets of two patients. The height of the prostate along superior-posterior axis was found almost the same (3.1% discrepancy) in CT and ER based-MR images. The width along left-right axis and the length along anterior-posterior axis differ a lot between CT and MR images. We measured the width and length of the prostate in the middle axial slices of two patients. The width of the prostate in MRI is  $116.9 \pm 1.5\%$  of that of the prostate in CT. The length of the prostate in MRI is  $82.1 \pm 1.4\%$  of that of the prostate in CT. After further comparing the shape of the prostates in CT and ER-MRI, we conclude that distortion mostly happens in the transverse plane. This observation

suggests that, to a reasonable approximation, we could perform the mapping procedure in a slice by slice fashion.

The TPS transformation was applied to the coregistration of the CT and ER-based MR images. We show a representative axial slice of a patient's CT images in Fig. 5A. To have a better view of the volume of interest, we selected a rectangular region encompassing the prostate (Fig. 5A right). The MR images were acquired with high resolution and the posterior portion of the image was distorted by the presence of the ER coil (Fig. 5B left). Eight control points were chosen along the contour of the corresponding MR and CT images. TPS transformation was applied to the distorted MR image and the mapped MRI contour of the prostate overlapped almost completely with that from the CT scan (Fig. 5B right). Difference between TPS-derived MR contour and CT contour is shown in Fig. 5C. Most prostate regions were in good agreement including the seriously contorted left and right posterior regions of the image. Similar results were obtained from the other patient.

We used centroid position displacement and coincidence index (CI) between the mapped MR images and the CT images to quantify the registration accuracy for these two datasets. Using the TPS method, the centroid displacement was  $0.58 \pm 0.10$  mm, significantly less than that of the non-deformable registration ( $1.96 \pm 0.43$  mm, Fig. 6A). The CI indices were found to be close to unity ( $92.6 \pm 5.1$  %), indicating that the TPS algorithm is able to model the nonrigid soft tissue deformation caused by the endorectal coil placement (Fig. 6B). On the other hand, a much lower CI,  $50.0 \pm 9.4$  %, was found when using the non-deformable registration. This suggests that fusion with a rigid-body

transformation and scaling is inadequate to deal with the system involving the images acquired with the ER coils.

The registration error depends on the appropriate placement of control point. We studied registration inconsistencies between different trials of one operator and between three operators. The intra-operator experiment was repeated five times on one patient's data. The centroid displacement was found to be in the range of 0.31 to 0.65 mm. The CI indices were found to be from 91.7% to 93.5%. Three operators were asked to repeat the control point placement five times and the mean results between the operators were compared. The centroid displacements were found to be  $0.55 \pm 0.30$ ,  $0.47 \pm 0.17$ , and  $0.54 \pm 0.25$  mm, respectively. The CI indices, corresponding to three operators, were  $92.7 \pm 0.9\%$ ,  $93.5 \pm 0.7\%$  and  $92.5 \pm 1.2\%$ , respectively. The centroid displacement and CI index show no significant difference between trials and operators.

#### **4. Discussion and Conclusion**

Registration has been implemented in several commercial medical image analysis and radiation treatment planning systems. For example, Radionics (Radionics<sup>TM</sup>, Burlington, MA) has developed ImageFusion software which provides the ability to fuse multiple image sets based on the mutual information. AcQSim Oncodiagnostic Simulation/Localization System (Philips Medical Systems, Cleveland, OH) provides two registration methods: point matching (a minimum of three common points need to be selected on both sets of images registered) and interactive image-based registration (a color wash of one image set is displayed over a grayscale image of the other). At this point, they all use a rigid-body transformation and scaling, which maintain the

straightness of lines, and hence cannot accommodate contour/shape distortion. In reality, the shape of the prostate gland can be easily changed by many factors such as patient position change, invasive brachytherapy procedures or endorectal coil placement during high resolution MR/MRS images acquisition <sup>26</sup>. To help physicians to segment the prostate gland and possible intraprostatic lesions by incorporating MRI/MRSI metabolic data on a CT-based treatment planning system, there is an indisputable need for developing a computationally efficient deformable registration technique to achieve voxel to voxel mapping. In this work, we used a TPS method to register the endorectal coil-based MR data with CT images. The data presented in the last section suggests that the TPS technique is well suited for this type of application.

The warping process was carried out in a slice-by-slice way and is worth of further investigation. This may result in the registration error in the longitudinal direction. Based on our observations for the two patients involved in this study, it seems that the distortion occurs mainly along the right-left and the anterior-posterior directions. The height of the prostate along the superior-inferior axis remains almost constant in the MR and CT datasets. This is consistent to the finding by another group in 1.5T MR imaging of the prostate <sup>26</sup>. In actuality, it is possible to extend the current quasi-2D model to a fully 3D one. The current study sheds useful insight into this type of extension and provides a nature starting point for the implementation of a complete 3D TPS mapping.

A few more sophisticated deformable registration methods have been investigated by several groups. A viscous- fluid transformation and fluid- landmark registration technique have been proposed to model the nonrigid deformation of organs in intracavitary brachytherapy <sup>24, 27</sup>. A finite-element method has been used to model the

tissue mechanical property and to register brain and prostate images <sup>28, 29</sup>. A biomechanical model of an elastic body has been used to quantify patient organ motion in the process of radiation therapy so that the dose delivered on the volume of a deforming organ can be accumulated <sup>30</sup>. These methods are usually computationally intensive. Moreover, the model parameters normally need to be determined empirically because of the lack of tissue biomechanical data in the literature, which compromises the advantages of these physics-based models. The TPS method is a simple deformable registration technique based on the mathematical interpolation. Our phantom and patient studies have shown that the approach is computationally efficient and can yield clinically acceptable registration accuracy.

It's noted that the TPS based registration needs manual placement of control points, which requires the input from an experienced clinician. This is similar to the previously reported rigid body- based registration method <sup>17, 25</sup>. The intra- and inter-operator experiments have shown that the registration accuracy doesn't not depend on the different operators or different trials significantly.

In conclusion, we have implemented a TPS transformation algorithm to map voxels in endorectal coil-based prostate MR/MRS images with those in CT images. The deformable mapping technique significantly improved the previously reported non-deformable method and should be adequate for routine clinical application. The accuracy of the approach has been tested by using phantom and patient studies. The registration scheme should be useful to map the functional MRSI data onto CT to guide the design of conformal radiation treatment plans.

## **Acknowledgements**

We would like to thank the useful discussion with A. Boyer, C. Cardenas, F. van den Haak, Y. Yang and Y. Song. This work was supported by a research grant from the prostate cancer research program of U.S. Department of Defense (DAMD17-03-1-0023).

## References

- <sup>1</sup> C. Bartolozzi, L. Crocetti, I. Menchi, S. Ortori, and R. Lencioni, Endorectal magnetic resonance imaging in local staging of prostate carcinoma. *Abdom Imaging*. **26**, 111-22 (2001).
- <sup>2</sup> M.D. Schnall, Y. Imai, J. Tomaszewski, H.M. Pollack, R.E. Lenkinski, and H.Y. Kressel, Prostate cancer: local staging with endorectal surface coil MR imaging. *Radiology*. **178**, 797-802 (1991).
- <sup>3</sup> M.D. Schnall, R.E. Lenkinski, H.M. Pollack, Y. Imai, and H.Y. Kressel, Prostate: MR imaging with an endorectal surface coil. *Radiology*. **172**, 570-4 (1989).
- <sup>4</sup> J.F. Martin, P. Hajek, L. Baker, V. Gyls-Morin, R. Fitzmorris-Glass, and R.R. Mattrey, Inflatable surface coil for MR imaging of the prostate. *Radiology*. **167**, 268-70 (1988).
- <sup>5</sup> R.A. Huch Boni, C. Meyenberger, J. Pok Lundquist, F. Trinkler, U. Lutolf, and G.P. Krestin, Value of endorectal coil versus body coil MRI for diagnosis of recurrent pelvic malignancies. *Abdom Imaging*. **21**, 345-52 (1996).
- <sup>6</sup> Y. Kaji, J. Kurhanewicz, H. Hricak, D.L. Sokolov, L.R. Huang, S.J. Nelson, and D.B. Vigneron, Localizing prostate cancer in the presence of postbiopsy changes on MR images: role of proton MR spectroscopic imaging. *Radiology*. **206**, 785-90 (1998).
- <sup>7</sup> J. Kurhanewicz, D.B. Vigneron, H. Hricak, P. Narayan, P. Carroll, and S.J. Nelson, Three-dimensional H-1 MR spectroscopic imaging of the in situ human prostate with high (0.24-0.7-cm<sup>3</sup>) spatial resolution. *Radiology*. **198**, 795-805 (1996).
- <sup>8</sup> L. Kwock, J.K. Smith, M. Castillo, M.G. Ewend, S. Cush, T. Hensing, M. Varia, D. Morris, and T.W. Bouldin, Clinical applications of proton MR spectroscopy in oncology. *Technology in Cancer Research & Treatment*. **1**, 17-28 (2002).
- <sup>9</sup> J.C. Presti, Jr., H. Hricak, P.A. Narayan, K. Shinohara, S. White, and P.R. Carroll, Local staging of prostatic carcinoma: comparison of transrectal sonography and endorectal MR imaging. *AJR Am J Roentgenol*. **166**, 103-8 (1996).
- <sup>10</sup> H. Hricak, G.C. Doms, R.B. Jeffrey, A. Avallone, D. Jacobs, W.K. Benton, P. Narayan, and E.A. Tanagho, Prostatic carcinoma: staging by clinical assessment, CT, and MR imaging. *Radiology*. **162**, 331-6 (1987).
- <sup>11</sup> M. Perrotti, R.P. Kaufman, Jr., T.A. Jennings, H.T. Thaler, S.M. Soloway, M.D. Rifkin, and H.A. Fisher, Endo-rectal coil magnetic resonance imaging in clinically localized prostate cancer: is it accurate? *J Urol*. **156**, 106-9 (1996).



- <sup>12</sup> G.J. Jager, J.L. Severens, J.R. Thornbury, J.J. de La Rosette, S.H. Ruijs, and J.O. Barentsz, Prostate cancer staging: should MR imaging be used?--A decision analytic approach. *Radiology*. **215**, 445-51 (2000).
- <sup>13</sup> S.F. Quinn, D.A. Franzini, T.A. Demlow, D.R. Rosencrantz, J. Kim, R.M. Hanna, and J. Szumowski, MR imaging of prostate cancer with an endorectal surface coil technique: correlation with whole-mount specimens. *Radiology*. **190**, 323-7 (1994).
- <sup>14</sup> P. Xia, B. Pickett, E. Vigneault, L.J. Verhey, and M. Roach, 3rd, Forward or inversely planned segmental multileaf collimator IMRT and sequential tomotherapy to treat multiple dominant intraprostatic lesions of prostate cancer to 90 Gy. *Int J Radiat Oncol Biol Phys*. **51**, 244-54 (2001).
- <sup>15</sup> S.J. DiBiase, K. Hosseinzadeh, R.P. Gullapalli, S.C. Jacobs, M.J. Naslund, G.N. Sklar, R.B. Alexander, and C. Yu, Magnetic resonance spectroscopic imaging-guided brachytherapy for localized prostate cancer. *Int J Radiat Oncol Biol Phys*. **52**, 429-38 (2002).
- <sup>16</sup> L. Xing, C. Cotrutz, S. Hunjan, A.L. Boyer, E. Adalsteinsson, and D. Spielman, Inverse planning for functional image-guided intensity-modulated radiation therapy. *Phys Med Biol*. **47**, 3567-78 (2002).
- <sup>17</sup> M. Zaider, M.J. Zelefsky, E.K. Lee, K.L. Zakian, H.I. Amols, J. Dyke, G. Cohen, Y. Hu, A.K. Endi, C. Chui, and J.A. Koutcher, Treatment planning for prostate implants using magnetic-resonance spectroscopy imaging. *Int J Radiat Oncol Biol Phys*. **47**, 1085-96 (2000).
- <sup>18</sup> C.C. Ling, J. Humm, S. Larson, H. Amols, Z. Fuks, S. Leibel, and J.A. Koutcher, Towards multidimensional radiotherapy (MD-CRT): biological imaging and biological conformality. *Int J Radiat Oncol Biol Phys*. **47**, 551-60. (2000).
- <sup>19</sup> B. Fei, A. Wheaton, Z. Lee, J.L. Duerk, and D.L. Wilson, Automatic MR volume registration and its evaluation for the pelvis and prostate. *Phys Med Biol*. **47**, 823-38 (2002).
- <sup>20</sup> B. Fei, C. Kemper, and D.L. Wilson, A comparative study of warping and rigid body registration for the prostate and pelvic MR volumes. *Comput Med Imaging Graph*. **27**, 267-81 (2003).
- <sup>21</sup> K.M. Brock, J.M. Balter, L.A. Dawson, M.L. Kessler, and C.R. Meyer, Automated generation of a four-dimensional model of the liver using warping and mutual information. *Med Phys*. **30**, 1128-33 (2003).
- <sup>22</sup> S. Fantozzi, A. Cappello, and A. Leardini, A global method based on thin-plate splines for correction of geometric distortion: an application to fluoroscopic images. *Med Phys*. **30**, 124-31 (2003).

- 23 F.L. Bookstein, Principal Warps: Thin Plate Splines and the Decomposition of Deformations. *IEEE Trans. Pattern Anal. Mach. Intell.* **11**, 567-85 (1989).
- 24 G.E. Christensen, B. Carlson, K.S. Chao, P. Yin, P.W. Grigsby, K. Nguyen, J.F. Dempsey, F.A. Lerma, K.T. Bae, M.W. Vannier, and J.F. Williamson, Image-based dose planning of intracavitary brachytherapy: registration of serial-imaging studies using deformable anatomic templates. *Int J Radiat Oncol Biol Phys.* **50**, 227-43 (2000).
- 25 T. Mizowaki, G.N. Cohen, A.Y. Fung, and M. Zaider, Towards integrating functional imaging in the treatment of prostate cancer with radiation: the registration of the MR spectroscopy imaging to ultrasound/CT images and its implementation in treatment planning. *Int J Radiat Oncol Biol Phys.* **54**, 1558-64 (2002).
- 26 M. Hirose, A. Bharatha, N. Hata, K.H. Zou, S.K. Warfield, R.A. Cormack, A. D'Amico, R. Kikinis, F.A. Jolesz, and C.M. Tempany, Quantitative MR imaging assessment of prostate gland deformation before and during MR imaging-guided brachytherapy. *Acad Radiol.* **9**, 906-12 (2002).
- 27 S.C. Joshi and M.I. Miller, Landmark matching via large deformation diffeomorphisms. *IEEE Trans Imaging Proc.* **9**, 1357-70 (2000).
- 28 A. Bharatha, M. Hirose, N. Hata, S.K. Warfield, M. Ferrant, K.H. Zou, E. Suarez-Santana, J. Ruiz-Alzola, A. D'Amico, R.A. Cormack, R. Kikinis, F.A. Jolesz, and C.M. Tempany, Evaluation of three-dimensional finite element-based deformable registration of pre- and intraoperative prostate imaging. *Med Phys.* **28**, 2551-60 (2001).
- 29 M. Ferrant, A. Nabavi, B. Macq, F.A. Jolesz, R. Kikinis, and S.K. Warfield, Registration of 3-D intraoperative MR images of the brain using a finite-element biomechanical model. *IEEE Trans Med Imaging.* **20**, 1384-97 (2001).
- 30 D. Yan, D.A. Jaffray, and J.W. Wong, A model to accumulate fractionated dose in a deforming organ. *Int J Radiat Oncol Biol Phys.* **44**, 665-75 (1999).

**Table 1**

Deformable and non-deformable registration error of the distorted phantoms shown in Fig. 3 B, C and D. The maximum refers to the maximum landmark displacement and the mean refers to the mean landmark displacement in each case.

Distortion (mm)	Non-deformable registration		Deformable registration	
	maximum	mean	maximum	mean
Fig. 3B	9.83	$4.62 \pm 2.71$	1.09	$0.45 \pm 0.53$
Fig. 3C	14.74	$7.35 \pm 4.20$	1.05	$0.57 \pm 0.49$
Fig. 3D	23.07	$12.95 \pm 6.57$	0.99	$0.62 \pm 0.39$

## Figure captions

Figure 1. A photo of the deformable phantom with implanted landmarks in a holder.

Figure 2. A registration study using a square phantom deformed by external force. (A) The phantom under the influence of a force (left) and its original shape (right). The distorted phantom is shown in a smaller scale than the original phantom in order to include part of the holder and external object. (B) The position of four control points on the distorted phantom as indicated by pink plus signs (left). The middle and right show the computed deformed image and difference image, respectively. (C) and (D) are similar to B except that six and eight control points are used respectively. (E) The landmark displacement of the three groups.

Figure 3. A registration study by systematically bending a rectangular phantom. (A) The original phantom. (B) The distorted phantom (left), the TPS-warped phantom (middle) and the difference image (right). (C) and (D) are similar to (B) except that with increased distortions.

Figure 4. Registration consistency test. Left panels of A, B and C represent the computer-warped images with the middle panel images of Fig. 3 B, C and D as input. Right panels of A, B and C represent the corresponding difference images between the mapped and the original images. D, Landmark displacement between the model prediction and the actual position for the three groups.

Figure 5. Deformable registration of the prostate gland in a patient. (A) A transverse CT study (left) and a region of interest encompassing the prostate (right). (B) The MRI study (left) and computer-deformed image (right). (C) Difference between the CT and the mapped MR image. The control points are denoted with plus signs.

Figure 6. Centroid position displacement (A) and coincidence index of deformable and non-deformable registration in patient studies (B).

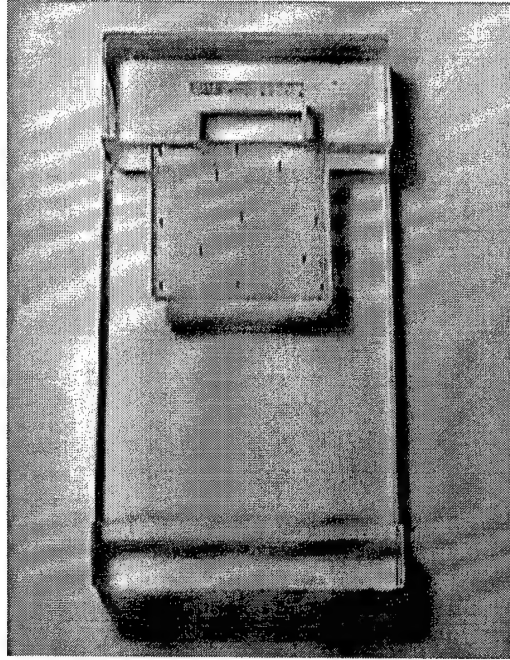
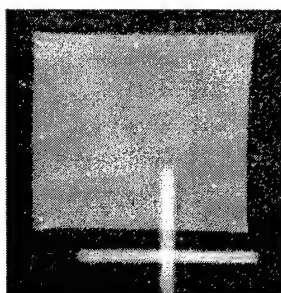
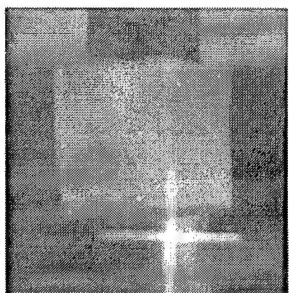
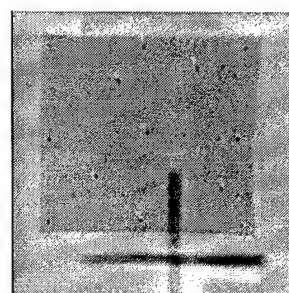
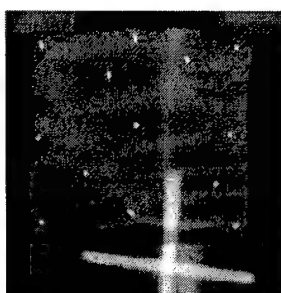
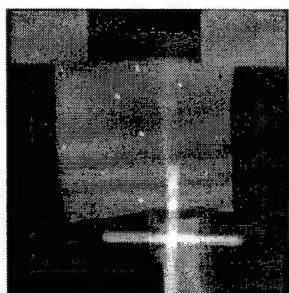


Figure 1

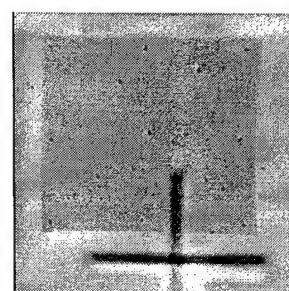
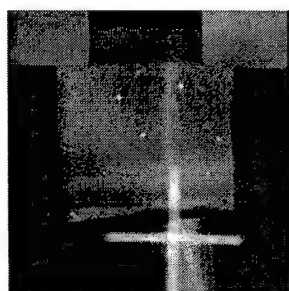
A



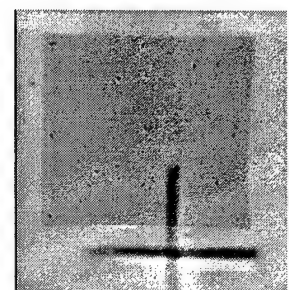
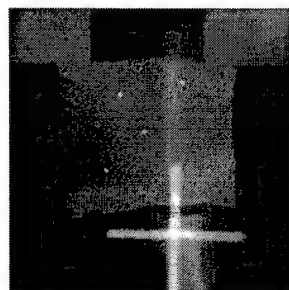
B



C



D



E

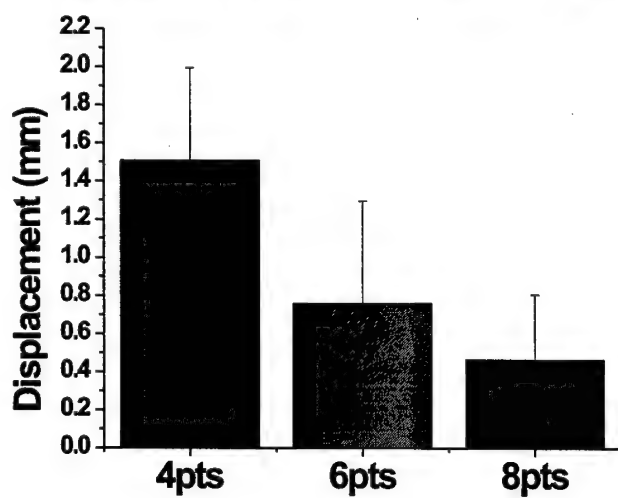
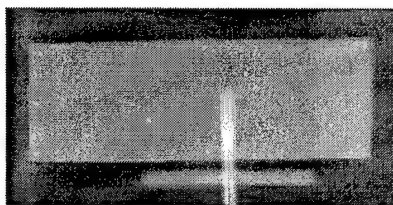
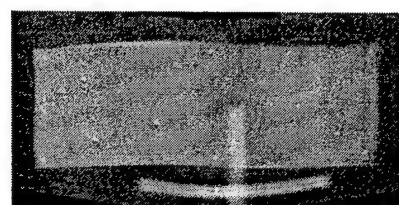
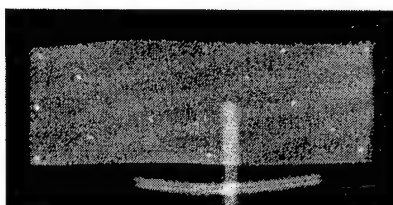
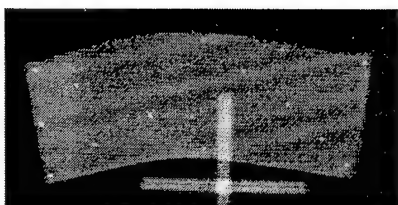


Figure 2

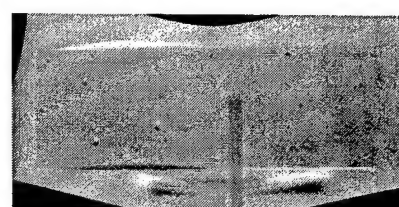
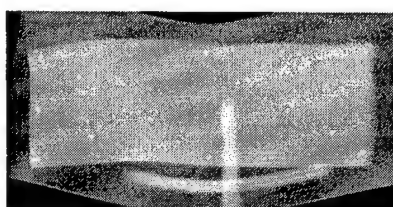
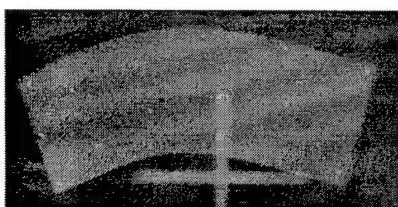
A



B



C



D

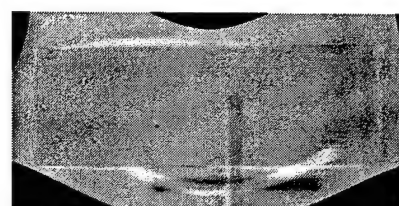
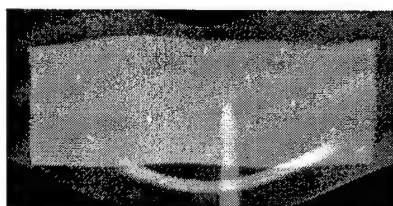
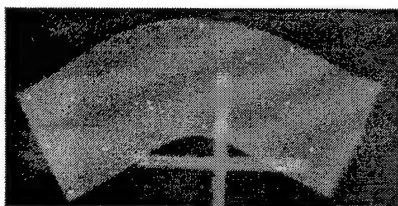
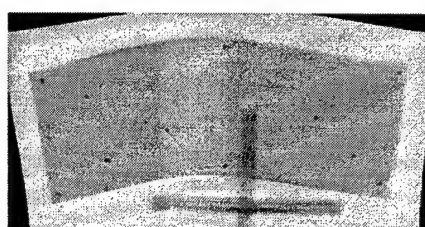
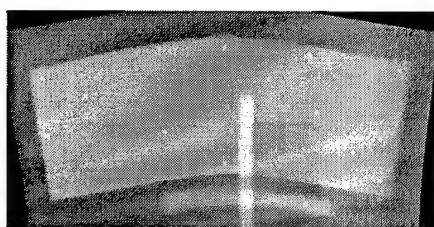


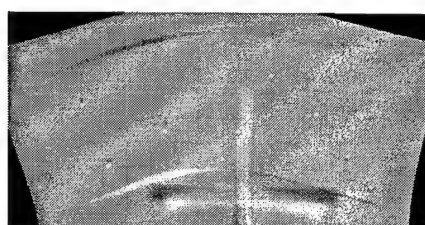
Figure 3



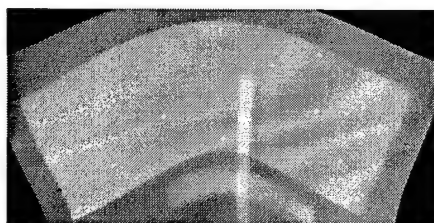
A



B



C



D

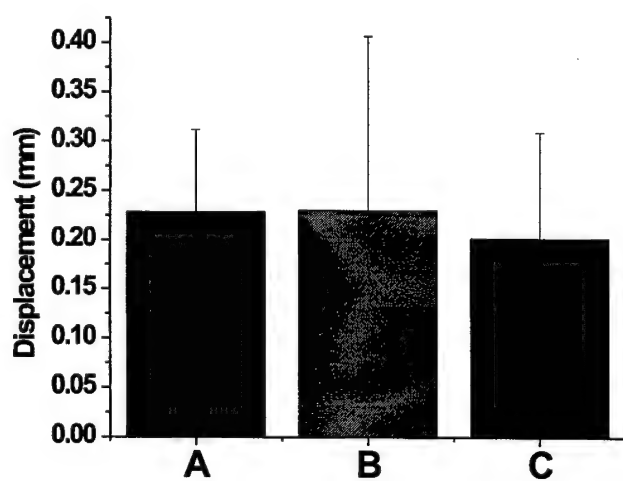
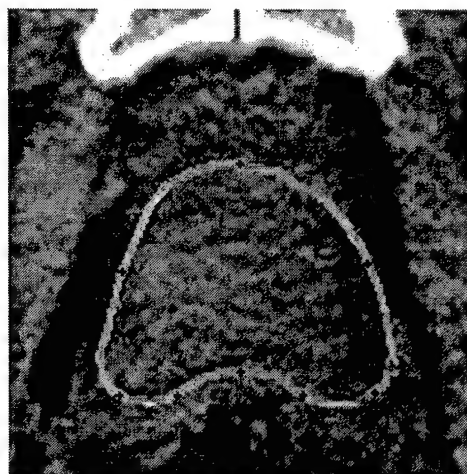
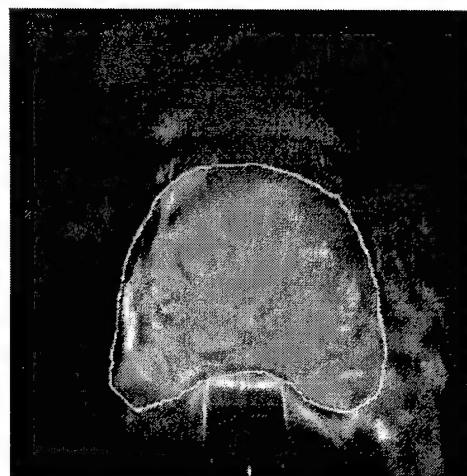


Figure 4

A



B

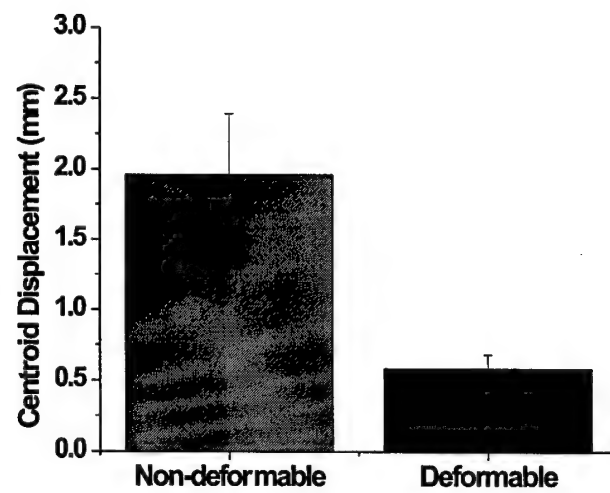


C



Figure 5

A



B

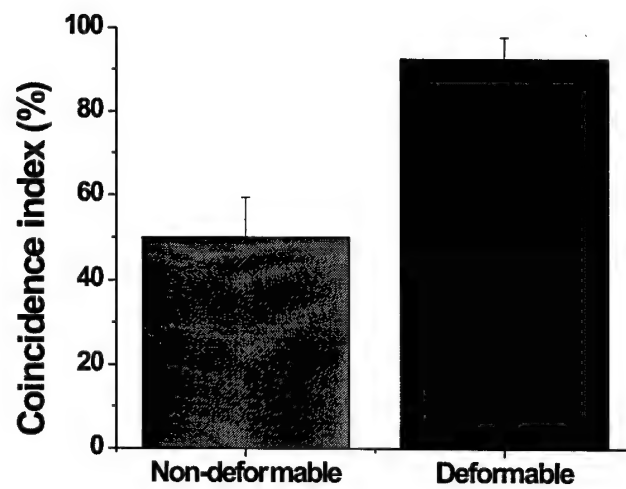


Figure 6

# Beam Orientation Class-Solutions for Prostate IMRT

Eduard Schreibmann, Ph.D. and Lei Xing<sup>a)</sup>, Ph.D.

Department of Radiation Oncology, Stanford University School of Medicine,

Stanford, California 94305-5304, USA

<sup>a)</sup>Author to whom correspondence should be addressed.

Stanford University School of Medicine  
Department of Radiation Oncology  
300 Pasteur Drive  
Stanford, CA 94305-5304

E-mail: lei@reyes.stanford.edu  
Phone: (650) 498 7896  
Fax: (650) 498 4015

Submitted to: Medical Physics

**Purpose:** IMRT is being increasingly used for treatment of prostate cancer. In practice, however, the beam orientations used for the treatments are still selected empirically without any guideline. The purpose of this work was to investigate inter-patient variation of the optimal beam configuration and to facilitate IMRT prostate treatment planning by deriving a set of beam orientation class-solutions for a range of numbers of incident beams.

**Method:** Fifteen prostate cases were used to generate the beam orientation class-solutions. For each patient and a given number of incident beams, a multiobjective optimization engine, which optimizes the beam directions by using a genetic algorithm and the beam profiles by a gradient-based algorithm, was employed to provide the patient specific beam directions. For each pre-selected number of beams, the angular distributions of the incident beams of the fifteen patients were analyzed and a population-based average of the angular distributions was conducted. The most frequent beam directions are identified as the class-solution for the corresponding number of incident beams. The level of validity of the class-solutions was tested using an additional clinical prostate case by comparing with the individually optimized beam configurations.

**Results:** In the case of five incident beams, beam configuration with gantry angles of 55°, 120°, 195°, 270° and 345° seems to yield the best possible IMRT dose distribution. For the fifteen cases considered, the gantry angle of any of the five beams was all distributed within a range of 18°, indicating that a population-based class-solution may provide a good approximation of the optimal beam orientations. In other cases with six to nine incident beams, similar trend was observed. The class-solution gantry angles for prostate IMRT were found to be: 3 beams-(110°, 230°, 350°), 5 beams-(50°, 120°, 190°, 260°, 330°), 6 beams-(60°, 120°, 180°, 240°, 300°, 360°), 7 beams-(20°, 70°, 120°, 170°, 220°, 270°, 320°), 8 beams-(20°, 65°, 110°, 155°, 200°, 245°, 290°, 335°), and 9 beams-(30°, 70°, 110°, 150°, 190°, 230°, 270°, 310°, 350°). The level of accuracy of the class-solution approach was examined by analyzing the difference between the plans obtained with class-solutions and patient specific optimizations.

**Conclusion:** A set of beam orientation class-solutions for prostate IMRT treatment planning are provided based on a beam orientation optimization study. This simplifies the trial-and-error selection of the beam orientations and facilitates the IMRT prostate treatment planning process.

**Key Words:** IMRT, class solution, prostate cancer, inverse treatment planning, dose optimization, beam orientation.

## Introduction

Beam configuration may have significant influence on the quality of an IMRT treatment even when a large number of incident beams (e.g., 9 beams) are used [1]. Clinically, however, the gantry angles are still selected empirically and multiple adjustments may often be required. This has become one of the bottleneck problems that hinder the optimal and efficient use of IMRT. A class-solution method for beam placement has been thought [2] [3]. The idea behind this approach is to construct a representative beam configuration based on previous experience, or more adequately, on accurate beam orientation optimization, for a given disease site and then use this "class-solution" for subsequent patient treatment planning. Unfortunately, up to this point, the degree of validity of this approach has never been tested, even for geometrically relatively regular disease site such as prostate, where it is believed that the class-solution should work. This paper systematically investigates the issue and derives a set of beam orientation class-solutions for IMRT prostate irradiation.

In the past few years, several groups have investigated the problem of beam orientations in 3D conformal radiation therapy [4-11] and in IMRT [12-18]. The main focus of these studies was on the modeling, formulation and optimization of beam configurations. To obtain a set of good gantry angles for an IMRT treatment, in principle, all one needs to do is to add the gantry angle variables into an objective function and then to optimize the objective function with respect to the gantry angles and the beamlet weights. A main difficulty of this type of brute-force optimization lies in its excessive computational time caused by the greatly enlarged search space. The development of beam orientation class-solution for some simple disease sites like prostate has the potential to significantly reduce the effort of beam placement in IMRT planning, which is thus of practical importance.

To derive a population-based beam orientation class-solution, the optimal solutions need to be obtained for at least a representative group of patients. For this purpose, in the next section we will present an effective beam orientation algorithm for the optimization of IMRT beam orientations. It is intuitively conceivable that the optimal beam configuration varies from patient to patient because of their geometric differences. Generally speaking, a class-solution exists if the inter-patient variation in the beam orientations distribution is small. As will be seen in the Results section, this is approximately the case for the representative group of fifteen prostate cases selected randomly from the patient pool treated at Stanford. We have investigated the behavior of the system for a variety of numbers of incident beams and provided the class-solutions for the

cases of five to nine incident beams to meet different clinical needs. Our study has indicated that the beam orientation class-solutions provided here represent good compromise between practicality and optimality and may facilitate the IMRT treatment planning by eliminating or simplifying the trial-and-error process of the beam orientation selection.

## Materials and methods

### *Multiobjective optimization*

A multi-objective (MO) optimization with a mix of genetic and iterative algorithms was used to optimize the system. The genetic algorithm optimizes the beam orientations and the gradient based method the intensity profiles of the beams. The MO is useful in radiotherapy dose optimization because of the existence of multiple conflicting objectives in the system. In the previous studies, the problem has been transformed into a single objective problem by introducing a set of importance factors to parameterize our tradeoff strategy [19]. The MO optimization tries to obtain all acceptable solutions and the more information on the tradeoff between the different objectives. Here, by an acceptable solution we mean a plan with a good compromise of all the objectives involved in the problem. Mathematically, the MO optimization or vector optimization [20] is to determine a set of decision variables that optimizes a vector function whose elements represent  $M$  objective functions without violating the system constraints.

We denote the decision variables in an optimization problem by  $\mathbf{x}=\{x_j, j=1,2,...,N\}$ . To access the goodness of a solution it is needed to establish some criteria of evaluation. These criteria are expressed as computable functions  $f_1(\mathbf{x}),..., f_M(\mathbf{x})$  of the decision variables, which are called *objective functions*. These form a vector function  $\mathbf{f}$ . The vector function  $\mathbf{f}(\mathbf{x})$  maps the set  $\mathbf{X}$  to the set  $\mathbf{F}$  that represents all possible values of the objective functions. In general, some of these objectives will be in conflict with others and do not have a situation in which all the  $f_i(\mathbf{x})$  reach their optimums at a common point  $\mathbf{x}$ . The multiobjective optimization problem is to find the vector  $\mathbf{x}=(x_1,x_2,...,x_N)$ , i.e., the solution which optimize the vector function  $\mathbf{f}$ .

To proceed, it is necessary to establish some criteria to define the optimality. These solutions in multiobjective optimization constitute the so-called Pareto optimum [21]. A solution  $\mathbf{x}_1$  dominates a solution  $\mathbf{x}_2$  if the two following conditions are true:

$\mathbf{x}_1$  is no worse than  $\mathbf{x}_2$  in all objectives, i.e.  $f_j(\mathbf{x}_1) \leq f_j(\mathbf{x}_2) \quad \forall j=1,...,M$

$\mathbf{x}_1$  is strictly better than  $\mathbf{x}_2$  in at least one objective, i.e.  $f_j(\mathbf{x}_1) < f_j(\mathbf{x}_2)$  for at least one  $j \in \{1,2,...,M\}$ .

We assume, without loss of generality, that the problem that we are dealing with here is a minimization problem. Among a set of solutions  $P$ , the non-dominated set of solutions  $P'$  are those that are not dominated by any other member of the set  $P$ . When the set  $P$  is the entire feasible search space then the set  $P'$  is called the *global Pareto optimal set*. If for every member  $\mathbf{x}$  of a set  $P$  there exists no solution in the neighborhood of  $\mathbf{x}$  then the solutions of  $P$  form a *local Pareto optimal set*. The image of the Pareto optimal set is called the *Pareto front*.

### ***Optimization method***

The variables to be optimized include the beam directions and the bixel intensities. We quantify the variables in a two-component chromosome. The first part  $\mathbf{W}$  contains the bixel weights of all beams with a double precision floating-point representation. The second part  $\mathbf{B}$  is a boolean string, which represents the possible beam directions. The boolean value records if the beam is active or not. In this study, the beams of coplanar setup are divided in 360 beams with  $1^\circ$  separation between adjacent beams. Each beam is divided in a grid of  $40 \times 40$  bixels and each bixel has a dimension of  $1 \times 1 \text{ cm}^2$ . Only bixels that pass through the PTV are activated and considered in the optimization process and the rest bixels are assigned with zero weights. The number of bixels to be optimized depends on the patient's geometry and number of beams ranging from 4050 to 9584 for the prostate cases analyzed in this paper.

The system was optimized using two algorithms: a genetic algorithm as the main optimization framework and a gradient-based algorithm applied on a fraction of the newly generated solutions. Without the gradient-based algorithm, the genetic algorithm will converge very slowly because the cost function is too sensitive to the changes in bixel weights generated by the genetic algorithm [22]. The gradient-based algorithm, used for a few iterations on the new solutions, lower the sensitivity by adjusting the bixel weights. While it is possible to use gradient-based algorithms alone [23, 24], a combination of a genetic algorithm with a gradient-based algorithm improves the convergence behavior and speeds up the optimization. The combinational optimization algorithm starts each time from an almost optimized set of bixels taken from the parent population, rather than from a new randomly selected set.

### ***Objective functions***

The objective functions used in this study for the PTV and for an OAR are defined as

$$f_{PTV} = \frac{1}{N_{PTV}} \sum_{j=1}^{N_{PTV}} (d_j^{PTV} - D_{ref})^2$$



$$f_{OAR} = \frac{1}{N_{OAR}} \sum_{j=1}^{N_{OAR}} (d_j^{OAR})^2$$

where  $\Theta(x)$  is the Heaviside step function,  $D_{ref}^{PTV}$  is the prescription dose to the PTV,  $d_j^{PTV}$  and  $d_j^{OAR}$  are the calculated doses at the  $j$ th sampling point for the PTV and OAR, respectively,  $N_{PTV}$  and  $N_{OAR}$  are the corresponding number of sampling points. We include as an additional objective the number of beams  $f_N$ .

All calculations in this paper are performed in 3D geometry with 15 MV photons. The incident photon fluence was divided into pencils and assigned with different transmission factors. The width of the pencil projected at the isocenter plane was 10 mm. The dose value at each sampling point was obtained from the interpolation of tissue maximum ratio (TMR) values and off-axis ratio (OAR) values. The sampling points were generated quasi-random in each structure [25], their number corresponding to the structures volume, at a density of 30 points/cm<sup>3</sup>. A minimum number of 1000 and a maximum number of 30000 where the limits imposed additionally on the number of points, in order to avoid over-sampling of the normal tissue or under-sampling of small structures.

### ***Dosimetric Constraints***

In accordance to the clinical practice, we impose two sets of constraints during the optimization process. The first restricts the maximum dose to an OAR to a value below  $D_{Limit}$ . The second one is fractional-volume limit, since for some OARs late effects would be resulted if a volume larger than a specific limit  $V_{Critic}$  is irradiated to a dose exceeding a critical value  $D_{Critic}$ . The dose limits for the rectum, bladder and femurs are assigned according to the literature [26, 27]. For the OARs, the selected values of  $D_{Limit}$  and  $V_{Critic}$ ,  $D_{Critic}$  are summarized in Table 1. The constraints imposed on the PTV include (a) the maximum dose should be less than 78 cGy; and (b) only 5% of the PTV volume may receive a dose of less than 72 cGy.

The constraints are implemented by assigning a better rank to the solutions satisfying the constraints, forcing selection of clinically sensible solutions. This was realized by using the constrained non-domination relation, which is used for the selection of the individuals of the population. The population in the NSGA-II algorithm is sorted according to the dominance. Non-dominated members are assigned rank 1. The remaining population is then again checked

and the non-dominated are assigned rank 2. This process continues until all members are classified.

### ***Optimization calculation***

We use for inverse planning the MO multi-objective evolutionary algorithm non-dominated sorting genetic algorithm with constrained elitism *NSGA-II* [28] that is one of the most effective evolutionary optimization algorithms. The gradient-based algorithm selected was the low memory BFGS algorithm (L-BFGS) to reduce the memory requirements in the iterative calculation of the cost functions gradient [29]

The crossover and mutation probability  $P_c$  and  $P_m$  were chosen as 0.9 and 0.01 for this study. The algorithm uses the arithmetic crossover and the non-uniform mutation. Because this is a N-dimensional problem where N is large, we use a population size of 100 to maintain the genetic algorithm's diversity. These optimal parameters have been estimated by comparing with results obtained using a deterministic gradient-based algorithm, which indicated that the Pareto front does not change significantly after 100 generations. The deterministic gradient based algorithm LBFGS is applied on all new solutions at each generation, and is used for 10 iterations. Without support from LBFGS, the algorithm would require 1000 or more generations to produce similar results.

### ***Selection of solutions from the Pareto set***

A set of solutions is generated at the end of a multiobjective optimization, each corresponding to an IMRT plan that is relevant to the clinical treatment [14,21]. Specifically, the treatment planner is provided with a table of values for all the members of the Pareto set of the objectives, DVHs for all OARs and PTV, and dose statistics. For a given patient and pre-selected number of beams, an appropriate solution is generally chosen from the Pareto set based on clinical considerations [14, 21]. The optimization objectives were to conform the PTV, while minimizes the dose to bladder and femoral heads.

### ***Beam orientation class-solutions***

Fifteen prostate cases were selected randomly from the patient pool at Stanford University Hospital. The patients were scanned in supine position, using a 3 or 4 mm CT slice thickness. The contours were delineated on a Philips virtual simulation system (Philips Medical System, Cleveland, OH) and imported in our in-house treatment planning system using the DICOM

transfer protocol. The beam orientation optimization was then performed for each of the patients for a range of number of incident beams ( $N=3, 5, 6, 7, 8$  and  $9$ ) using the algorithm described above. Only coplanar beams were considered in this work. The angular distribution of the incident beams for a given number of incident beams for the fifteen patients was analyzed. For each number of beams, we identified the directions for the class-solution by averaging the gantry angles of the fifteen patients.

### ***Test of the degree of validity of class-solution***

In order to test the validity of the beam orientation class-solution approach we randomly selected additional prostate patient from the patient pool at Stanford University Hospital. Two IMRT plans were generated for the patient: one with class-solution selected beams and one with beams chosen by the patient specific beam orientation optimization. The difference between the two plans is analyzed according to the commonly used plan evaluation indices, such as DVH, maximum/minimum/average target/sensitive structure doses.

## **Results**

### ***Pareto front plans for a given patient***

For a given patient, a set of plans is provided by the multiobjective optimization described in the last section, that is, the user is provided with a spectrum of plan index values, each characterizes the quality of a plan in the Pareto front. The DVH of a given structure also constitutes a spectrum of curves instead of a single curve. In Figure 1 we show the DVH spectra of prostate, rectum, and bladder for a representative patient for all the non-dominated five-field IMRT plans in the Pareto front.

Each non-dominated plan in the Pareto front has different beam parameters (bixel maps and/or gantry angles). The angular distributions of the Pareto front plans for the above patient are shown in Fig. 2 for different number of incident beams. If a beam direction is more feasible it shows up in the final plans with high frequency. For 3 beams the directions appeared with high frequencies in the Pareto front plans are at  $120^\circ$ ,  $240^\circ$  and  $340^\circ$ . It is interesting to note that the beam configuration is similar to that found by inspecting the most-selected plan. Small peaks appear at  $60^\circ$  and  $290^\circ$  because they are opposite to the most favorable beam directions, *i.e.*,  $240^\circ$  and  $120^\circ$ .

As will be seen in the next section, for 3-7 beams, the angles of the maximums of the angular distributions are in accordance with directions found using the most-selected plans. As the number of beams increased, the importance of optimizing beam orientation decreases and a large

set of beam configurations with more “diffusive” angular distributions become capable of producing valid plans with adequate PTV coverage and OAR sparing. In this situation, the feature of distinct peaks in the angular distribution diminishes.

### *Class-solutions*

For a given patient, the beam configuration occurring most frequently in the Pareto front is identified as the optimal one. In figure 3 we show the optimized five-beam configurations for each of the fifteen patients. Two symmetrical configurations are observed, with one beam passing through either left or right femur. To better visualize this, in figure 4b we show the gantry angles for the fifteen patients (Figure 4) on a single plot. We select the configuration with one beam passing through the right femur. The gantry angles of the ideal class-solution for IMRT treatment with five incident beams seems to be  $55^\circ$ ,  $120^\circ$ ,  $195^\circ$ ,  $270^\circ$  and  $345^\circ$  and are indicated in red in figure 4b. These angles were selected based on the average direction for each cluster of beam orientations in the most-selected plans. For practice purpose, it is desirable to “round” the beam angles to a set of more convenient implementable beams. With the consideration of angular distribution of each beam direction shown in figure 4b, we identify 5-beam class-solution to be  $50^\circ$ ,  $120^\circ$ ,  $190^\circ$ ,  $260^\circ$ , and  $330^\circ$ . Because of the adjustment is done with the range of the angular distribution of the beams, the compromise is limited. We note that the equispaced setup is in accordance to the findings of [17, 30], and the starting gantry configuration of  $60^\circ$  is consistent with that of Ref. [31].

The solutions derived above seem to be physically sensible. Setting the angles of beams 1 2 and 4 to  $50^\circ$ ,  $120^\circ$  and  $260^\circ$  balances the dose to the femoral heads. The locations of the 3<sup>rd</sup> ( $190^\circ$ ) and 5<sup>th</sup> ( $330^\circ$ ) beams are chosen to balance the dose requirements of the PTV and rectum. Depending on the geometry of the case, the optimizer makes individual adjustments of the beam angles, but the selected directions are within a  $\pm 18^\circ$  window. The standard deviations of the five fields are  $10^\circ$ ,  $30^\circ$ ,  $30^\circ$ ,  $35^\circ$ , and  $25^\circ$ , respectively.

The same calculation described above is repeated for 3, 6, 7, 8 and 9 incident beams and the distributions of the optimal configurations for the fifteen cases are shown in figure 4. The class-solution for each of the situations is presented in figure 4 in red. For convenience, the beam angles of the class-solution are summarized here: 3 beams-( $110^\circ$ ,  $230^\circ$ ,  $350^\circ$ ), 5 beams-( $50^\circ$ ,  $120^\circ$ ,  $190^\circ$ ,  $260^\circ$ ,  $330^\circ$ ), 6 beams-( $60^\circ$ ,  $120^\circ$ ,  $180^\circ$ ,  $240^\circ$ ,  $300^\circ$ ,  $360^\circ$ ), 7 beams-( $20^\circ$ ,  $70^\circ$ ,  $120^\circ$ ,  $170^\circ$ ,  $220^\circ$ ,  $270^\circ$ ,  $320^\circ$ ), 8 beams-( $20^\circ$ ,  $65^\circ$ ,  $110^\circ$ ,  $155^\circ$ ,  $200^\circ$ ,  $245^\circ$ ,  $290^\circ$ ,  $335^\circ$ ), and 9 beams-( $30^\circ$ ,  $70^\circ$ ,  $110^\circ$ ,  $150^\circ$ ,  $190^\circ$ ,  $230^\circ$ ,  $270^\circ$ ,  $310^\circ$ ,  $350^\circ$ ). After adjustments with consideration of the 3-7 beams, the locations of the maximums of the angular distributions for the fifteen patients are consistent with the

directions found using the most-selected plans. The beam setups tend to be equispaced when 3-7 beams are used, with the first beam placed around 20-50°. We noticed that as the number of incident beams increases, the beams tend to be less confined to a few fixed directions (see figure 4). Instead, the optimal configuration for a case may differ from another significantly. In addition, the quality of the final plan becomes less sensitive to the beam angle variations. In other words, as the number of beams increases, the importance of optimizing beam orientation decreases. As a result, it is less necessary to derive a class-solution for IMRT prostate treatment with 8 or 9 beams. Practically, however, it is still desirable to have a set of fixed gantry angles to “streamline” the clinical IMRT treatment planning process. For this reason, we have specified a set of beam configurations for these situations in Figure 4.

It is interesting to observe that, in the case of 6 and 8 beams, one pair of beams are required to incident from opposed (or almost opposed) directions in the class-solution. We expect that when lower energy photons are used, more opposed beam pairs will show up in the final solution.

#### ***Evaluation of class-solution approach***

Validity of the class-solution approach was investigated by comparing plans obtained based on patient specific beam orientation optimization and beam orientation class-solution. An additional patient was selected from the patient pool of Stanford University Hospital. Two sets of plans were generated. In the first set, the optimizer uses fixed beams during the optimization process, with the directions taken from the class-solution, while in the second set beams orientation are optimized. Both 5 and 9 incident beams were studied.

In figure 5a we show the Pareto fronts of the two plans when 5 beams are used. As can be seen from the figure, the Pareto fronts obtained with the two methods are similar. For comparison, we selected one optimal plan from each set and made a side-by-side comparison (Figure 5b). The two plans were found to be quite similar and both plans satisfied the imposed constraints. The plan with class-solution beam configuration irradiates slightly more volume of rectum at lower doses but is slightly better at high doses. Similar results were found in the case of 9 incident beams, as can be seen from figure 6.

#### **Conclusion**

In general, the beam orientation class-solution is an oversimplified approach since, clinically, the anatomy, target shape and its relative location with respect to the adjacent sensitive structures, and the patient's radiation treatment history may vary from patient to patient. An

individualized beam configuration is frequently, if not always, needed to achieve the best possible treatment. In actuality, however, there exist a few disease sites (such as prostate) where the shapes, locations and prescribed doses of various structures involved in the treatment vary slightly from case to case. In this situation, beam angle class-solution approach may be an acceptable compromise. In this work, we have studied the inter-patient variation of the optimal beam configurations for prostate IMRT and derived beam orientation class-solutions for the cases of 5-9 incident fields based on analysis of patient specific beam orientation optimization for fifteen prostate cases. The level of accuracy of the class-solution approach was examined by analyzing the difference between the plans obtained with class-solutions and patient specific optimizations. We found that, when the number of incident beams is less or equal to 7, the angle variations from patient to patient are within 18, suggesting the existence of beam angle class-solution for prostate IMRT. When the number of beams is greater than 7, the class-solution becomes less meaningful but may be useful to "streamline" clinical practice. Finally, we mention that in a sense any optimization algorithm has a certain degree of subjectivity due to the difference in the objective function employed to model the system. It would be interesting to explore such model dependence and further examine the validity of the proposed class-solution using different model systems. Given the fact that IMRT is being increasingly employed for prostate cancer irradiation, we believe that this type of study may have practical implication for clinical IMRT, especially before the users are provided with a robust beam orientation optimization tool in the clinical IMRT treatment planning systems.

### Acknowledgements

We would like to thank the useful discussion with Drs. S.L. Hancock, C. King, A. Boyer, J. Hai, A. Pugachev, Y. Yang, J. Lian, Z. Shou, and C. Cotrutz. This work is supported in part by a research grant from the prostate cancer research program of U.S. Department of Defense (DAMD17-03-1-0023) and the American Cancer Society (RSG-01-022-01-CCE).

### References

1. Pugachev A., Li J.G., Boyer A. L., Hancock S. L., Le Q. T., Donaldson S. S., Xing L., *Role of beam orientation optimization in intensity-modulated radiation therapy*. International Journal of Radiation Oncology, Biology, Physics, 2001. **50**(2): p. 551-60.
2. Reinstein, L.E., Hanley J., Meek A.G., *A feasibility study of automated inverse treatment planning for cancer of the prostate*. International Journal of Radiation Oncology, Biology, Physics, 1997. **40**(1): p. 207-14.

3. Xing, L., Pugachev A., Li J.G., Le Q. T., Donaldson S. S., Goffinet D., Hancock S. S., Boyer, A. L. *A medical knowledge based system for the selection of beam orientations in IMRT*. International Journal of Radiation Oncology, Biology, Physics, 1999. **45**(3): p. 246.
4. Soderstrom, S., Brahme A., *Which is the most suitable number of photon beam portals in coplanar radiation therapy?* International Journal of Radiation Oncology, Biology, Physics, 1995. **33**(1): p. 151-9.
5. Gokhale P., Hussein E.M.A., Kulkarni N., *Determination of beam orientation in radiotherapy planning*. Med Phys, 1994. **21**(3): p. 393-400.
6. Hosseini-Ashrafi M.E., Bagherebadian H., Yahaqi E, *Pre-optimization of radiotherapy treatment planning: an artificial neural network classification aided technique*. Phys Med Biol, 1999. **44**(6): p. 1513-28.
7. Rowbottom, C.G., Webb S., and Oldham M., *Beam-orientation customization using an artificial neural network*. Physics in Medicine & Biology, 1999. **44**(9): p. 2251-62.
8. Ezzell G.A., *Genetic and geometric optimization of three-dimensional radiation therapy treatment planning*. Med Phys, 1996. **23**(3): p. 293-305.
9. Das S.K., Marks L.B., *Selection of coplanar or noncoplanar beams using three-dimensional optimization based on maximum beam separation and minimized nontarget irradiation*. Int J Radiat Oncol Biol Phys, 1997. **38**(3): p. 643-55.
10. Rowbottom, C.G., Oldham M., and Webb S., *Constrained customization of non-coplanar beam orientations in radiotherapy of brain tumours*. Physics in Medicine & Biology, 1999. **44**(2): p. 383-99.
11. Sailer S.L., Rosenman J.G., Symon J.R., Cullip T.J., Chaney E.L., *The tetrad and hexad: maximum beam separation as a starting point for noncoplanar 3D treatment planning: prostate cancer as a test case*. Int J Radiat Oncol Biol Phys, 1994. **30**(2): p. 439-46.
12. Stein J., Mohan R., Wang X. H., Bortfeld T., Wu Q., Preiser K., Ling, C. C., Schlegel W. *Number and orientations of beams in intensity-modulated radiation treatments*. Medical Physics, 1997. **24**(2): p. 149-60.
13. Asell, M., Hyodynmaa S., Soderstrom S., Brahme A. *Optimal electron and combined electron and photon therapy in the phase space of complication-free cure*. Physics in Medicine & Biology, 1999. **44**(1): p. 235-52.
14. Bortfeld T. and Schlegel W. *Optimization of beam orientations in radiation therapy: some theoretical considerations*. Physics in Medicine & Biology, 1993. **38**(2): p. 291-304.
15. Haas O.C., Burnham K.J., Mills J.A. *Optimization of beam orientation in radiotherapy using planar geometry*. Phys Med Biol, 1998. **43**(8): p. 2179-93.

16. Pugachev, A., Xing L., Boyer A.L.. *Beam orientation optimization in IMRT: to optimize or not to optimize?* in *XII International Conference on the Use of Computers in Radiation Therapy*. 2000. Heidelberg, Germany.
17. Pugachev B.A., Boyer A.L., Xing L. *Beam orientation optimization in intensity-modulated radiation treatment planning*. *Med Phys*, 2000. **27**(6): p. 1238-45.
18. Braunstein M., Levine R.Y., *Optimum beam configurations in tomographic intensity modulated radiation therapy*. *Phys Med Biol*, 2000. **45**(2): p. 305-28.
19. Xing L., Li J.G., Donaldson S., Le Q.T., Boyer, A.L., *Optimization of importance factors in inverse planning*. *Physics in Medicine & Biology*, 1999. **44**(10): p. 2525-36.
20. Yu Y., *Multiobjective decision theory for computational optimization in radiation therapy*. *Med. Phys.*, 1997. **24**: p. 1445-1454.
21. Cotrutz C., Lahanas M., Kappas C., Baltas D. *A multiobjective gradient-based dose optimization algorithm for external beam conformal radiotherapy*. *Physics in Medicine & Biology*, 2001. **46**(8): p. 2161-75.
22. Hou Q., Wang J., Chen Y., Galvin J.M. *Beam orientation optimization for IMRT by a hybrid method of the genetic algorithm and the simulated dynamics*. *Med Phys*, 2003. **30**(30): p. 2271-2567.
23. Wu, X., Zhu Y., Dai J., Wang Z.. *Selection and determination of beam weights based on genetic algorithms for conformal radiotherapy treatment planning*. *Physics in Medicine & Biology*, 2000. **45**(9): p. 2547-58.
24. Wu, X., Zhu Y., *An optimization method for importance factors and beam weights based on genetic algorithms for radiotherapy treatment planning*. *Physics in Medicine & Biology*, 2001. **46**(4): p. 1085-99.
25. Lahanas M, Baltas.D., Giannouli S, Milickovic N and Zamboglou N, *Generation of uniformly distributed dose points for anatomy-based three-dimensional dose optimization methods in brachytherapy*. *Med. Phys*, 2000. **27**(1034-46).
26. Boersma L.J., van den Brink M., Bruce A.M., Shouman T., Gras L., te Velde A., Lebesque J.V. *Estimation of the incidence of late bladder and rectum complications after high-dose (70-78 GY) conformal radiotherapy for prostate cancer, using dose-volume histograms*. *International Journal of Radiation Oncology, Biology, Physics*, 1998. **41**(1): p. 83-92.
27. Emami, B., Lyman J., Brown A., Coia L., Goitein M., Munzenrider J. E., Shank B., Solin L. J, Wesson M., *Tolerance of normal tissue to therapeutic irradiation*. *International Journal of Radiation Oncology, Biology, Physics*, 1991. **21**(1): p. 109-22.



28. Deb K., Goyal M. *A combined genetic adaptive search (GeneAS) for engineering design*. Computer Science and Informatics, 1996. **26**: p. 30-45.
29. Nocedal J., Dong C.L., *On the limited memory BFGS method for large scale optimization*. Mathematical Programming, 1989. **45**: p. 503-528.
30. Rowbottom, C.G., Webb S., Oldham M. *Improvements in prostate radiotherapy from the customization of beam directions*. Medical Physics, 1998. **25**(7 Pt 1): p. 1171-9.
31. Djajaputra D., Wu Q., Wu Y., Mohan R. *Algorithm and performance of a clinical IMRT beam-angle optimization system*. Phys. Med. Biol, 2003. **48**: p. 3191-3212.

## FIGURES

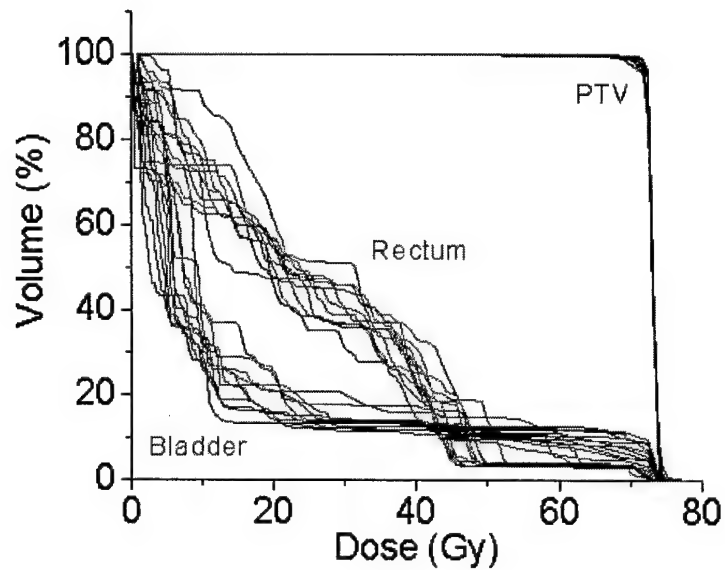


Figure 1 DVH spectra of prostate (red), rectum (green), and bladder for a representative patient for all the non-dominated plans in the Pareto front.

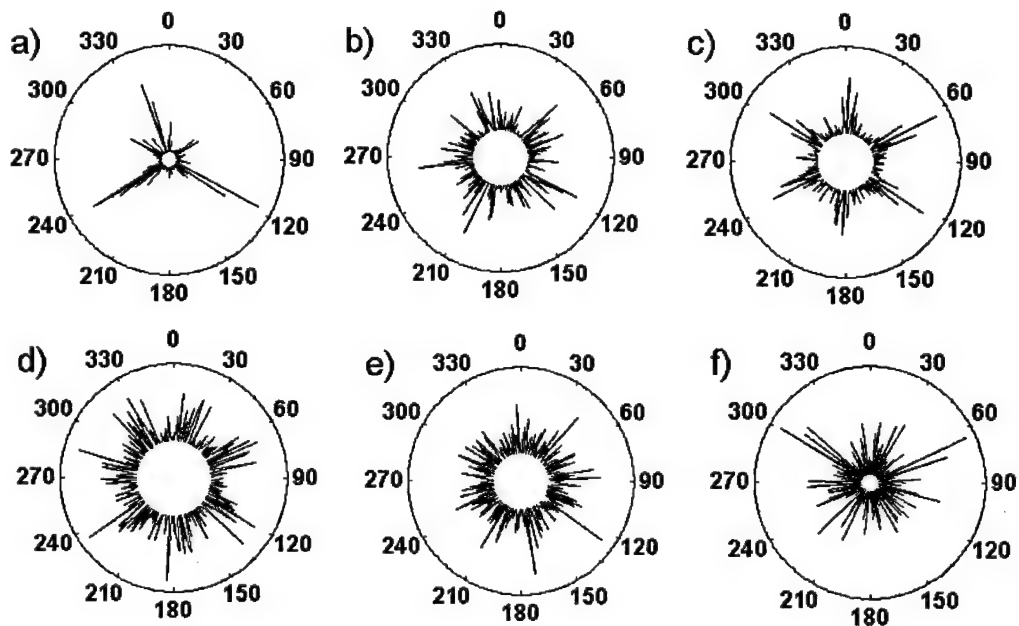


Figure 2 Angular distribution of beams selected by the optimizer, for plans with 3,5-9 beams. The length of the radial segment in the above graphs represents the frequency of occurrence of the corresponding direction.

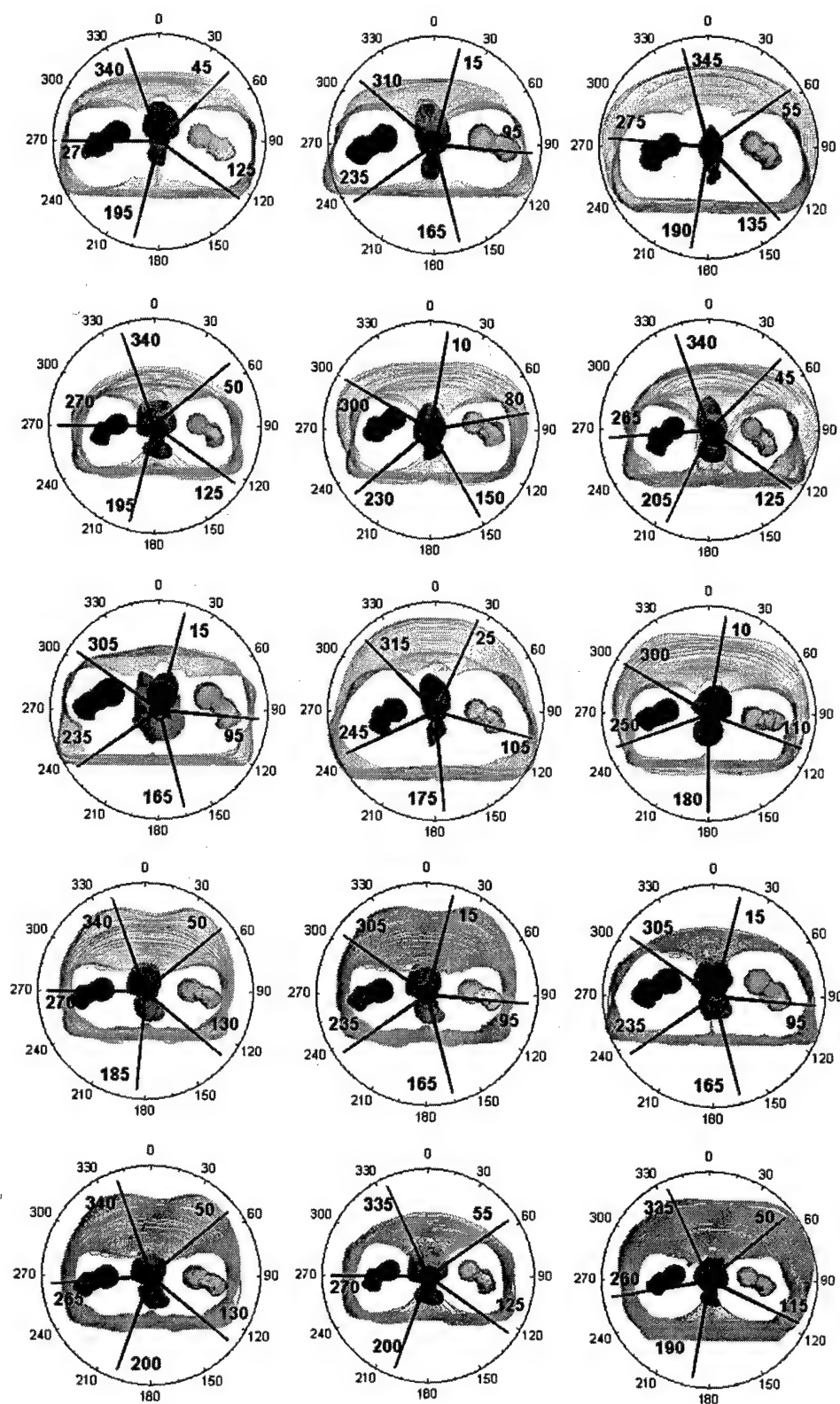


Figure 3. The optimal configuration in 5-beams plans for each of the fifteen individual cases.

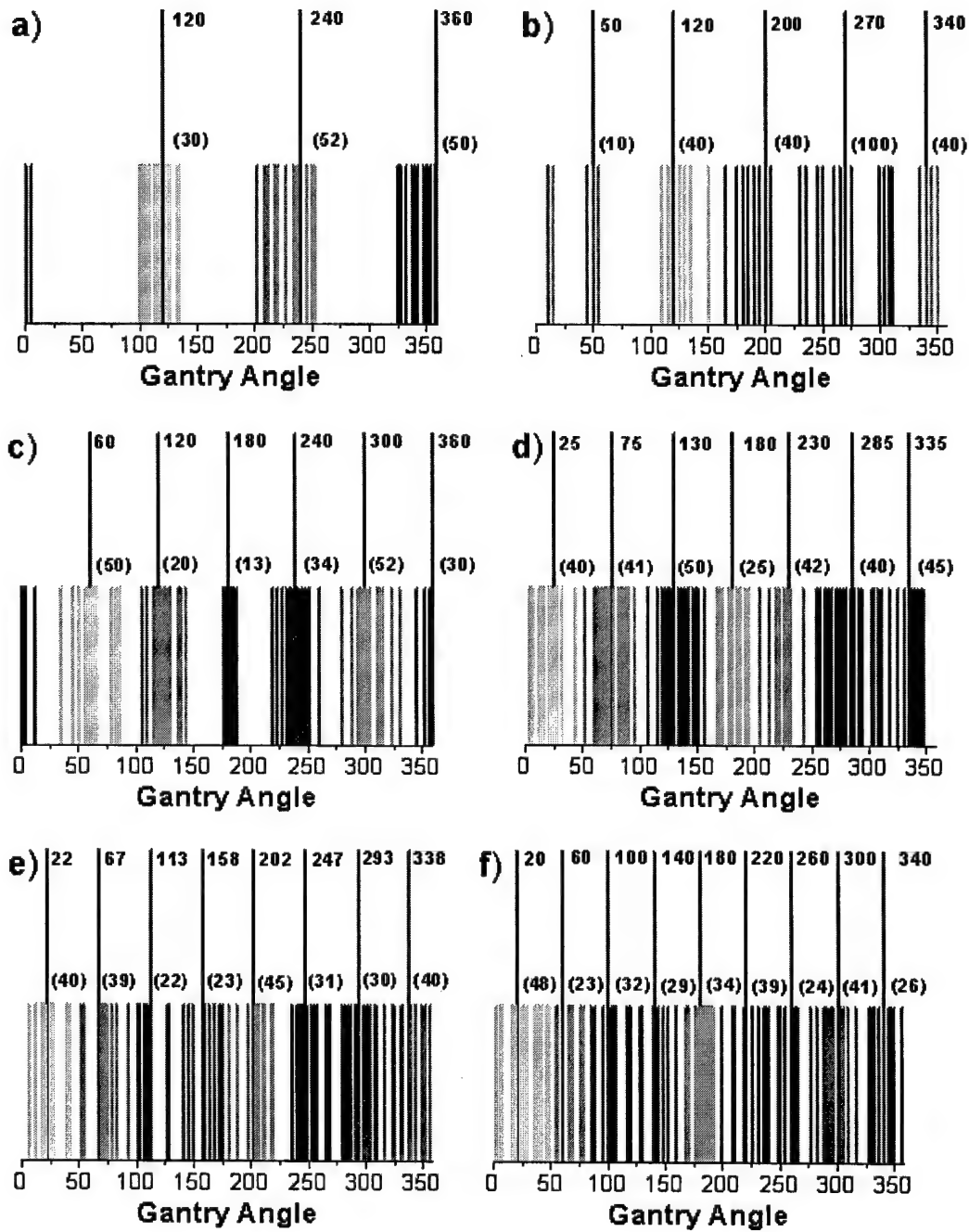


Figure 4 Distributions of beam angles for 3, 5-9 beams, respectively. The colored lines represent directions found in individual cases and red bold lines represent the directions identified as the class-solutions.

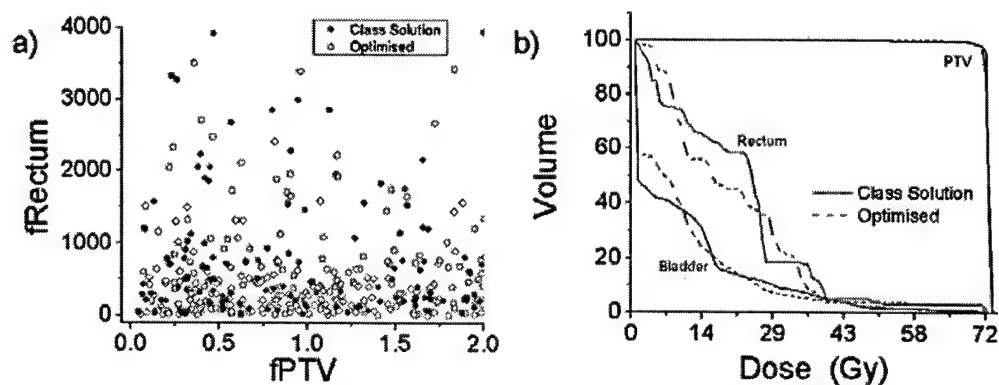


Figure 5 Comparison of plans with customized beams directions and class-solution directions a) Pareto fronts obtained by the two methods b) DVHs of class-solution plan (broken line) and optimized plan.

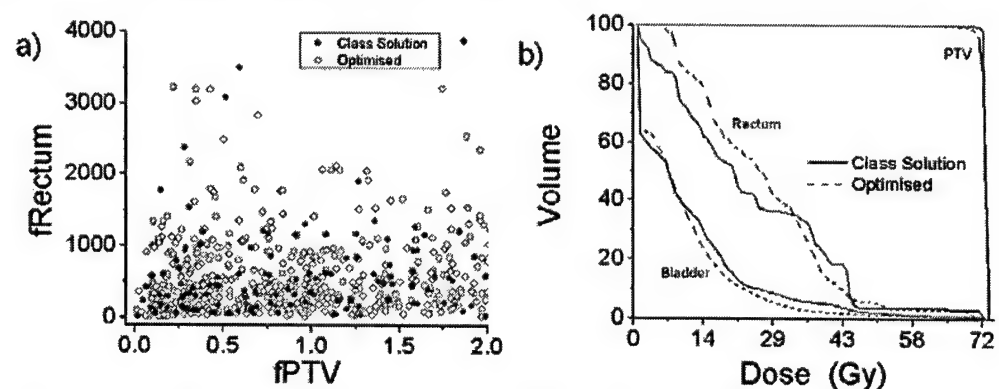


Figure 6 Comparison of class-solution plans and optimised plans for 9 beams. a) Pareto fronts b) DVHs

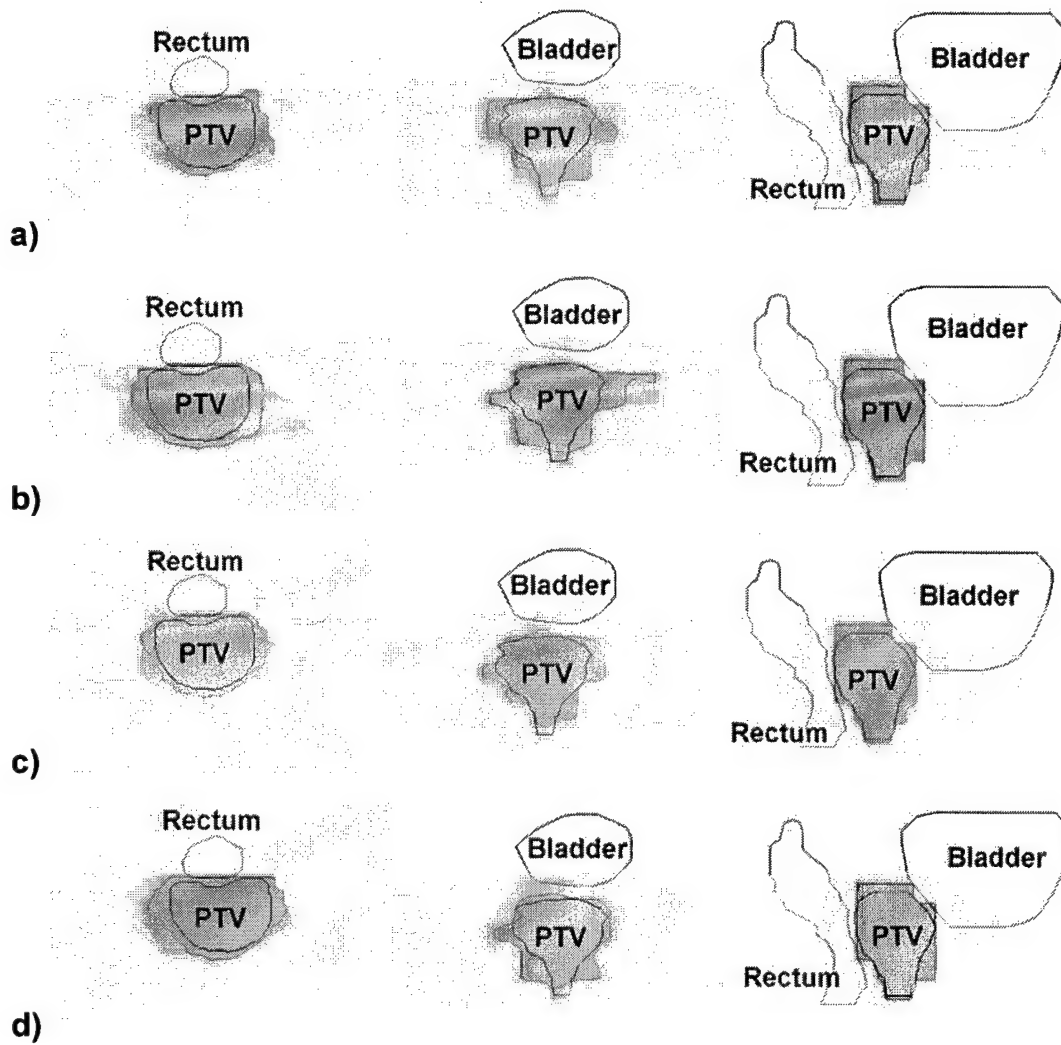


Figure 7 Color wash dose distributions in axial, coronal, and sagittal planes, for the following cases: a) 5 beams plan with optimized directions; b) 5 beams plan with class-solution directions; c) 9 beams plan with optimised directions; and d) 9 beams plan with class-solution directions. Structures are represented as lines : rectum (green) bladder (violet) and PTV (red)

## TABLES

Organ	Max dose $D_{\max}$ (Gy)	Critical dose $D_{\text{Critic}}$ (Gy)	Limit volume $V_{\text{Critic}}$ (% of organ volume)
NT	75	40	20
Left Femur	68	40	20
Rectum	72	53	25
Right Femur	68	40	20

**Table I** Dose limits and volume limits used as constraints for OARs. The prescribed dose was 72 cGy to the PTV and 0 cGy to the OARs. For each OAR, two constraints are imposed: (a) the maximum dose; and (b) a specified volume should not receive a dose greater than the limit dose.

# **Clinical Knowledge-Based Inverse Treatment Planning**

Yong Yang, Ph.D. and Lei Xing<sup>a)</sup>, Ph.D.

Department of Radiation Oncology, Stanford University School of Medicine,  
Stanford, CA 94305-5847

Short title: IMRT inverse planning

<sup>a)</sup> Author to whom correspondence should be addressed:

Department of Radiation Oncology  
Stanford University School of Medicine,  
Clinical Cancer Center  
875 Blake Wilbur Drive, Rm G-204  
Stanford, CA 94305-5847  
Telephone: (650) 498-7896  
Fax: (650) 498-4015  
Email: lei@reyes.stanford.edu

Submitted to: *International Journal of Radiation Oncology, Biology, Physics*



**Purpose:** Clinical IMRT treatment plans are currently done using dose-based optimization algorithms, which do not consider the nonlinear dose-volume effects for tumors and normal structures. The choice of structure specific importance factors represents an additional degree of freedom of the system and makes rigorous optimization intractable. The purpose of this work is to circumvent the two problems by developing a biologically more sensible yet clinically practical inverse planning framework.

**Methods and Materials:** The dose-volume status of a structure was characterized by using the effective volume in the voxel domain. A new objective function was constructed with incorporation of the volumetric information of the system so that the figure of merit of a given IMRT plan depends not only on the dose deviation from the desired dose distribution but also the dose-volume status of the involved organs. To automate the determination of the structure specific importance factors, we wrote the conventional importance factor of an organ into a product of two components: (i) a generic importance that parameterizes the relative importance of the organs in the ideal situation when the goals for all the organs are met; (ii) a dose-dependent factor that quantifies our level of clinical/dosimetric satisfaction for a given plan. The generic importance can be determined *a priori*, and in most circumstances, does not need adjustment, whereas the second one, which is responsible for the intractable behavior of the tradeoff seen in conventional inverse planning, was determined automatically. For this purpose, we heuristically expressed the second factor as a function of TCP or NTCP. After beam optimization, the TCP/NTCP was computed and its value determined whether the corresponding importance factor should be increased or decreased. The procedure proceeded in an iterative fashion until the overall objective function stopped improving. An inverse planning module based on the proposed formalism was implemented and applied to a prostate case and a head-neck case.

**Results:** The incorporation of clinical knowledge allows us to obtain IMRT plans that would otherwise be unattainable and makes it possible to auto-select the importance factors, greatly facilitating the inverse planning process. Comparison of the newly

proposed approach with the conventional inverse planning technique indicated that, for the same target dose coverage, the critical structure sparing was substantially improved for both cases. Conversely, the dose to the target volume can be escalated greatly while maintaining the radiation toxicity at the current level.

**Conclusions:** The modeling of inverse planning objective function plays an essential role in the success of IMRT treatment and the incorporation of the existing clinical endpoint data into inverse planning affords an effective way to improve the sub-optimal performance of current IMRT planning algorithms. The new formalism proposed in this paper also reveals the relationship between different inverse planning schemes and sheds important insight into the problem of therapeutic plan optimization.

***Key word:*** IMRT, inverse planning, dose optimization, objective function, NTCP

## Introduction

An important issue in inverse treatment planning is how to formalize the clinical goals to objectively evaluate the figures of merit of different IMRT plans. Despite of intense research effort in modeling the clinical decision-making strategies(1-6), appropriate form of the objective function for clinical IMRT planning remains illusive. Presently, two types of objective functions are being widely used: dose- or dose volume histogram (DVH)-based (physical objective functions)(7-16) and dose response-based objective functions (biological objective functions)(17-23). The underlying difference between these models lies in what endpoints are used to evaluate the treatment or which fundamental quantities are used to define the optimality. The physical approach emphasizes the difference between the calculated and prescribed doses and does not consider the nonlinear effects for tumors and normal structures. Dose-volume constraints are often introduced to select a solution with certain shapes of the DVHs for the target and sensitive structures. However, it is important to note that the construction of the DVH constraints is *a priori* in nature. The use of constraints can only passively restrict the accessible DVHs of the final solution by narrowing the solution space and the figures of merits of the physically realizable plans are not changed as long as they satisfy the constraints. To reflect our preference over certain DVHs for a structure it is necessary to express the objective of the structure as a function of the volumetric status, which has not been achieved in inverse treatment planning up to this point. On the other hand, biological model-based optimization proponents argue that plan optimization should be guided by estimates of biological effects, which depend on the radiation dose through the dose response function. The treatment objective in biological model-based inverse planning is usually stated as the maximization of the tumor control probability (TCP) while maintaining the normal tissue complication probability (NTCP) to within acceptable levels(5, 17-21, 23). In principle, the biologically based models are most relevant for radiotherapy plan ranking(24-29). However, the dose-response function of various structures is not sufficiently understood and, at this point, there is considerable controversy about the models for computing dose-response indices and their use in optimization. In reality, the use of dose-response indices for optimization may lead to very inhomogeneous target dose distributions(5, 18-21, 23). Furthermore, it is difficult

for clinicians to specify the optimization criteria in terms of certain dose response indices (e.g., TCP, NTCP and P<sub>+</sub>). This issue becomes compounded when two or more independently optimized plans are to be combined. Because of these problems, the use of biological model-based dose optimization has mainly been limited in research community and little effort has been made to implement the model into commercial IMRT planning system. Given the fact that biological outcome is the ultimate endpoint of radiation therapy, the importance of the biological modeling and the biological model-based inverse planning can never be over stated.

To pin down the underlying problem of the current inverse planning formalism and illustrate the need for a clinically more relevant approach, let us take parotid glands as an example. It is well known that the clinical end point is the same if the glands are irradiated 15Gy to 67%, or 30Gy to 30%, or 45Gy to 24% of the total volume(30). If a dose-based metric, such as the commonly used quadratic objective function, is used, the rankings for the three different scenarios would be completely different. Even with the use of dose-volume constraints, it is difficult, if not impossible, to incorporate this type of knowledge to correctly model the behavior of the organ in response to radiation. Indeed, a constraint in optimization acts as a "boundary condition" during the optimization and does not change the rankings of dosimetrically different plans. This example clearly reveals the inadequacy of the conventional dose-based objective function and suggests the urgent need for a clinically more sensible model. Obviously, a minimum requirement for the model is that it should be consistent with the existing clinical outcome data. For parotid glands, for instance, the three different DVHs mentioned above should be scored equally by the objective function. We believe that this type of "degeneracy" is achieved by effectively integrating clinical end point data into the inverse planning formulation. For a given patient, as for which of the degenerate DVHs will be selected, it will be determined by the optimization algorithm with consideration of the dosimetric/clinical requirements of other structures. The specifics of the plan selection process will, of course, depend on the geometric and dosimetric details of the given patient. The example, however, underscores the important role of the existing clinical data in inverse planning and emphasizes the essential ingredients for a clinically realistic objective function. Towards developing a biologically more sensible yet clinically practical inverse planning

formalism, in the following we propose a method to incorporate clinical endpoint data into the construction of the IMRT objective function and attempt to bridge the gap between the clinical decision-making process and the computational modeling. Our study indicates that the clinical knowledge-based model developed in this work allows us to more objectively rank radiation therapy plans according to their clinical merits and makes it possible to obtain truly optimal IMRT plans with much reduced efforts.

## **Methods and Materials**

### ***Dose-volume effect***

To express the treatment objective of an organ as a volumetric function, a critical step is to identify the quantity that characterizes the dose-volume status of the organ and differentiates one DVH state from another. Once the quantity is selected, the objective function can be constructed in the representation defined by the quantity with consideration of clinical outcome data. It appears that there are two ways to proceed. One is to work in the dose-volume domain, in which the dose-volume status of an organ is characterized by the shape of the DVH curve itself. Since, at this point, clinical outcome data are sparse and underdetermined, it is impossible for us to objectively rank all physically realizable plans based on the data, necessitating an interpolation/extrapolation scheme for plan ranking if one chooses to work in the dose-volume domain. A more convenient representation is perhaps the voxel domain since it is relatively intuitive and much work has already been done in the past to describe the dose-volume effect. The key here is how to “extrapolate” the clinical endpoint observed at an organ level to an expression at the individual voxel level. However, it is important to note that the dose-volume presentation is, in principle, a more rigorous domain to deal with the dose-volume effect. The equivalence mapped to the voxel domain is generally established phenomenologically based on sparse clinical data and represents, at best, an approximation of the true dose-volume response relation.

In this research we work in the voxel domain. Generally, the dose response of a structure with respect to the irradiated dose and volume is complicated. The fact that the

dose distribution in tumor or a sensitive structure is generally inhomogeneous makes the establishment of such a relationship even more intractable. Over the last two decades, attempts have been made by many researchers to capture the main feature(s) of the dose volume effects. A power law model represents one of the successful techniques in dealing with the dose-volume effects of sensitive structures(28, 31). In this model an equivalent dose uniformly irradiating the whole organ,  $D_{eq}$ , can be used to represent the situation in which a fractional partial volume,  $v$ , is irradiated to a dose,  $D$ , by a simple power law model:  $D_{eq} = v^{1/n} D$ . A remarkable characteristic of this model is that, although only a single organ-specific parameter,  $n$ , is used, clinical and biological data has shown that this power law holds well at low complication levels(28, 32). Based on this relation, Mohan et al(17) introduced the concept of effective dose to represent a non-uniform dose distribution in a sensitive structure. Kutcher and Burman(29) applied the same power model independently to each volume element of the histogram and introduced the concept of effective volume to reduce the DVH of an inhomogeneous dose distribution in a sensitive structure to a uniform dose distribution. Following their study, we define the effective volume  $(\Delta V_{eff})_i$  for a voxel  $i$  with volume  $\Delta V$  and dose  $D_c(i)$  as follows

$$(\Delta V_{eff})_i = \Delta V (D_i(i) / D_{ref})^{1/n} \quad (1)$$

and extend this concept to handle the voxels in the tumor target, where  $n$  is an organ-dependent parameter and  $D_{ref}$  is the reference dose. For a sensitive structure,  $n$  is a small positive number ( $0 < n < 1$ ) and the value of parameter  $n$  reflects the architecture (serial or parallel) of the sensitive structure. For a target,  $n$  should be assigned with a small negative value ( $-1 < n < 0$ ). The biological meaning of Eq. (1) is that for a sensitive structure a small volume receiving a higher dose than a reference dose would be equivalent to a larger volume receiving the reference dose; for a target, a volume with a lower dose would have a larger effective volume. The effective volumes of all voxels reflect the DVH status of the given organ, and for inverse planning, this permits us to deal with the complicated dose-volume effect in the voxel domain.

### ***Dose-volume based objective function***

The objective function expressed as a function of the effective volume in the voxel domain should take the form of

$$f_{\sigma} = f_{\sigma}(\{(\Delta V_{eff})_i\}), \quad (2)$$

Generally, the dose-volume effect suggests that the voxels receiving different doses are inequivalent: the one with a larger effective volume (higher dose for a critical organ) should be penalized more when compared to a voxel with a smaller effective volume (lower dose). Thus we heuristically write the  $f_{\sigma}$  in the following form

$$f_{\sigma} = 1 + \eta_1 \sum_i r_i (\Delta V_{eff})_i + \eta_2 \left[ \sum_i r_i (\Delta V_{eff})_i \right]^2 + \dots, \quad (3)$$

where  $r_i$  is the importance factor of the  $i$ -th voxel, representing the intrastructural tradeoff due to physical/clinical requirements other than the dose-volume based penalty,  $\eta_1$  and  $\eta_2$  are phenomenological parameters of the model. In Eq. (3), the third (and higher order) term emphasizes more on the voxels with high effective volumes, whereas the first and second terms ensure that the voxels with low effective volumes receive an adequate penalty. We typically set  $r_i \equiv 1$  in Eq. (3), unless there are other physical/clinical considerations (e.g., when the density of clonogenes varies spatially (33)). In this work, unless specifically mentioned, we set  $\eta_1 = 1$  and  $\eta_2 = \eta_3 = \dots = 0$ .

#### *Hybrid of dose-based and dose volume-based objective functions*

Equation (3) provides a good description of the dose-volume effect. With proper choice of the parameter,  $n$ , the clinically observed dose volume effect can be reproduced by the objective function. In reality, other clinical requirements, such as the target dose homogeneity, should also be considered. A more general form of inverse planning objective function can be written as a hybrid of the dose-volume based and the dose-based functions. In this situation, the overall objective function of the system takes the form of

$$F = \sum_{\tau=1}^{t_{\tau}} r_{\tau} \frac{1}{N_{\tau}} \sum_{i=1}^{N_{\tau}} \{1 + \eta_1^{\tau} [D_c(i) / D_{\tau,ref}]^{1/n_{\tau}}\} |D_c(i) - D_0^{\tau}(i)|^{k_{\tau}} \\ + \sum_{\sigma=1}^{s_{\sigma}} r_{\sigma} \frac{1}{N_{\sigma}} \sum_{i=1}^{N_{\sigma}} \{1 + \eta_1^{\sigma} [D_c(i) / D_{\sigma,ref}]^{1/n_{\sigma}}\} D_c(i)^{k_{\sigma}}, \quad (4)$$

where Eq. (1) has been incorporated,  $r_{\tau}$  and  $r_{\sigma}$  are the structure specific importance factor for target  $\tau$  or sensitive structure  $\sigma$ ,  $t_{\tau}$  and  $s_{\sigma}$  are the numbers of targets and sensitive

structures,  $n_\tau$  and  $n_\sigma$  are the  $n$  parameters for target  $\tau$  and sensitive structure  $\sigma$ ,  $D_{\tau,ref}$  and  $D_{\sigma,ref}$  are the reference doses for target  $\tau$  and sensitive structure  $\sigma$ , respectively. The factor  $|D_c(i) - D_0^\tau(i)|^{k_\tau}$  for target or  $D_c(i)^{k_\sigma}$  for a sensitive structure represents the contribution from dosimetric deviation from the ideal situation. If the  $k_\tau$  and  $k_\sigma$  are set to zero, Eq. (4) becomes identical to Eq. (3) and the objective function becomes purely dose-volume driven. In particular, if we set  $k_\sigma$  to zero and  $k_\tau$  to a non-zero value, the objective function for a target becomes a hybrid of dose-volume and dose based, whereas the objective functions for critical structures remain to be purely dose-volume based. On the other hand, when all the  $n$  parameters in Eq. (4) are set to be  $+\infty$ , no dose-volume effects are considered and Eq. (4) is reduced to the conventional dose-based objective function. It is interesting to note that, according to Eqs. (2) and (4), the added dose-based factor can be interpreted as a voxel-dependent importance factor which increases with the dosimetric deviation from the ideal situation for the target or a sensitive structure. It seems to make intuitive sense to assign a high weight (or importance) to those voxels that receive doses farther away from the ideal situations so that more penalty can be applied to these voxels. Conversely, the dose-volume factor,  $f_\sigma$ , can be regarded as the voxel-dependent importance factor for a dose-based objective function. The local importance factor now increases with the effective volume at the voxel. We emphasize that these voxel-based importance factors are derived directly from the existing clinical knowledge instead of heuristic arguments.

#### *Automatic determination of structure specific importance factors*

The selection of structure specific importance factors,  $r_\tau$  or  $r_\sigma$  in Eq. (4), is generally done empirically with trial-and-error. Here we describe an alternative and more automated approach for solving the problem and show that the selection of structure specific importance factors can be facilitated by using computer optimization. The key of success is to establish an effective method to express the structural importance factor in terms of physically or clinically more meaningful quantities. For this purpose we write the importance factor of an involved structure into a product of two components: (i) a generic importance that parameterizes the relative importance of the organs in an ideal



situation when the goals for the organs are met; and (ii) a dose-dependent factor that quantifies our level of clinical/dosimetric satisfaction for a given plan. The first factor can be determined *a priori*, and in most circumstances, does not need adjustment (generally speaking, the value of  $r_\sigma^g$  is determined based on the treatment modality and the patient's overall condition, age, types of complications expected, and so on), whereas the second one is responsible for the intractable behavior of the tradeoff in conventional planning and can be automatically determined. This decomposition is essentially to normalize the conventional importance factor in terms of our clinical goal for the structure under discussion. Because of this decomposition, the meaning of the importance factor is more transparent and the determination of the factors becomes straightforward. Mathematically, we write the organ specific importance factor of a sensitive structure as  $r_\sigma = r_\sigma^g r_\sigma^d$ , where  $r_\sigma^g$  represents the first contribution described above (the desired weighting among different structures in an ideal situation), and  $r_\sigma^d$  is the second component and is defined as a relative ratio against a known clinical end point (for example, 5% complication rate for a sensitive structure). In this study  $r_\sigma^g$  was set empirically (See tables II and III for examples).  $r_\sigma^d$  is updated according to the DVH or the dose distribution during the optimization process and reflects the most current status of tradeoff in the system. For a sensitive structure, the value of  $r_\sigma^d$  is defined as, in this study, the ratio of NTCP against a desired complication probability, say 5%. Generally, the importance of a sensitive structure should be increased in next iteration if NTCP is high, and *vice versa*. We found that a simple linear relation between  $r_\sigma^d$  and NTCP,

$$r_\sigma^d = NTCP_\sigma + \delta \quad (5)$$

describes the tradeoff behavior of the system well, where  $NTCP_\sigma$  is the NTCP corresponding to the dose distribution at the current iteration for structure  $\sigma$ ,  $\delta$  is a cutoff factor for NTCP, which is introduced to ensure the sensitive structure receiving a minimum penalty even if its NTCP is close to zero. We set  $\delta$  as an organ-independent constant of 0.01%.

NTCP was assessed using Lyman's model in this study. For non-uniform irradiation, the Kutcher-Burman effective-volume DVH reduction method(29) is used to

transform a DVH into a uniform irradiation on an effective partial volume. There are three parameters in this model ( $n$ ,  $m$ ,  $TD_{50/5}$ ). The parameter  $n$  represents the volume effect and the parameter  $m$  is the steepness of the dose complication curve for a fixed partial volume. Model parameters used in this study were those fitted to the model by Burman et al(34) for the normal tissue tolerance data compiled by Emami et al(35).

### Computational Algorithm

After considering the automatic tradeoff strategy, the generalized objective function takes the following form

$$F = \sum_{\tau=1}^{I_{\tau}} r_{\tau} \frac{1}{N_{\tau}} \sum_{i=1}^{N_{\tau}} \{1 + \eta_{\tau}^t [D_c(i) / D_{\tau,ref}]^{1/n_{\tau}}\} |D_c(i) - D_0^T(i)|^{k_{\tau}} \\ + \sum_{\sigma=1}^{n_{\sigma}} r_{\sigma}^g r_{\sigma}^d \frac{1}{N_{\sigma}} \sum_{i=1}^{N_{\sigma}} \{1 + \eta_{\sigma}^s [D_c(i) / D_{\sigma,ref}]^{1/n_{\sigma}}\} D_c(i)^{k_{\sigma}}. \quad (6)$$

We implemented a software module to optimize the objective function (6) in the platform of the PLUNC treatment planning system (University of North Carolina, Chapel Hill, NC). The dose calculation engine and varieties of evaluation tools of the PLUNC system were used to evaluate and compare the optimization results. The calculation was performed on a PC with P4 1.7GHz and 1024MB RAM. The ray-by-ray iterative algorithm (SIITP) reported earlier(9, 36) was employed to obtain the optimal beam intensity profiles. The values of  $k_{\tau}$  and  $k_{\sigma}$  in Eq. (6) were set to be 2, but the behavior of the system for a few other combinations of  $k_{\tau}$  and  $k_{\sigma}$  were also checked for the prostate case. The reference dose,  $D_{\sigma,ref}$ , was chosen to be  $TD_{5/5}$  of the corresponding critical organ. For the target,  $D_{\tau,ref}$  was set as the prescription dose. Figure 1 shows the flow chart of the calculation process. In current study we specify a maximum number of iterations as the termination condition of the optimization process. The DVHs can be inspected in each iterative step to visually monitor the optimization process.

### Case studies

Two cases, a prostate case and a head-neck case, were used to evaluate the proposed inverse planning formalism. The optimization results were compared with those obtained using the conventional dose-based optimization method, which was described in

details by Xing et al (9, 36). The optimization parameters in the dose-based method were adjusted by trial-and-error to obtain an “optimal” plan.

In the prostate IMRT case, the target volume included the prostate and seminal vesicles. The sensitive structures involved in this study were rectum, bladder and femoral heads. All the IMRT plans used identical configuration of five equally spaced 15MV photon beams with gantry angles of  $0^\circ$ ,  $72^\circ$ ,  $144^\circ$ ,  $216^\circ$ , and  $288^\circ$  (in IEC convention). The plans were normalized to deliver the prescription dose of 70Gy to 99% of the target volume. The parameter  $n_t$  was chosen to be  $-0.2$  for the target. The parameters used for the computation of the NTCPs for rectum, bladder and femoral heads are listed in Table I, which were obtained by Emami et al(35) and Burman et al(34). Table II summarizes the optimization parameters for both the newly proposed and dose-based approaches.

For the prostate case, we also studied the influence of two more combinations of  $k_\sigma$  and  $k_\tau$ . These included  $(k_\sigma=2, k_\tau=4)$  and  $(k_\sigma=0, k_\tau=2)$ . In the latter case, we have included a higher order term of the dose-volume effect (the third term in Eq. (3) with  $\eta_2=1$ ) to ensure that the high effective volume voxels are penalized enough in the absence of the dose-based factor.

In the head-and-neck case, the organs at risk included the eyes, optic nerves, optic chiasm, brainstem, spinal cord and parotids. Two treatment targets were included in this case: the gross target volume (GTV) and the clinical target volume (CTV), which includes the microscopic disease region surrounding the GTV. The plan was normalized to deliver a prescription dose of 70Gy to at least 99% of the GTV and 62Gy to at least 95% of the CTV. Nine equally spaced 6MV coplanar beams ( $0^\circ$ ,  $40^\circ$ ,  $80^\circ$ ,  $120^\circ$ ,  $160^\circ$ ,  $200^\circ$ ,  $240^\circ$ ,  $280^\circ$ , and  $320^\circ$  in IEC convention) were used for this case. The parameter  $n_t$  were  $-0.5$  for both GTV and CTV. The parameters used for the computation of the NTCPs of the sensitive structures are also obtained from the same source stated earlier and are listed in Table I. The optimization parameters for both the two techniques are summarized in Table III.

## Results

### *Prostate IMRT plans*

Figures 2 and 3 summarize the results of the two IMRT plans obtained using the newly proposed and conventional techniques. Figure 2 compares the isodose distributions in two transverse slices and a sagittal slice for the two plans. The DVHs of the prostate target and sensitive structures are plotted in figure 3, in which the solid and dashed lines represent the DVHs obtained using the new and conventional approaches, respectively. The calculated NTCPs of rectum, bladder and femoral heads for both IMRT plans are listed in table IV. According to the table, it is seen that the NTCPs of the sensitive structures are improved significantly. For the rectum, for example, the NTCP is reduced from 0.45% to 0.03%. Our results also indicate that the main compromise in a prostate IMRT treatment seems to be between the tumor coverage and the rectum complication because the NTCP of the rectum is much higher than that of other sensitive structures.

The above results demonstrate that, for comparable target coverage, the new inverse planning technique greatly improves the critical structure sparing, especially the rectum sparing. By comparing the isodose distributions of the two plans (figure 1), it is seen that the dose gradient at the interface between the target and the rectum is much steeper for the IMRT plan obtained with the new formalism. Furthermore, it is intriguing that the non-sensitive structure normal tissue also receives less dose in comparison with that of the dose-based optimization. Our results suggest that the improvement in the critical structure sparing is achieved not at the cost of higher target dose inhomogeneity, which is commonly seen in IMRT plan optimization.

The resultant DVHs when  $k_\sigma=2$  and  $k_\tau$  was increased from 2 to 4 in Eq. (6) are plotted in Fig. 3 as the dotted curves. While the target dose uniformity is improved when the  $k_\tau$  increases, the doses to the rectum and bladder are worsened. The results make intuitive sense as when the  $k_\tau$  increases, more penalty is applied toward dosimetric deviation from the prescription. The DVHs when the objective function for the target is a hybrid of dose-volume and dose based functions ( $k_\tau=2$ ) and that for the sensitive structures are purely dose-volume based ( $k_\sigma=0$ ) are shown in Fig. 3 as dash-dotted curves. In this case, a high order term of the dose-volume effect in Eq. (3) was added to ensure that the high effective volume voxels are penalized enough in the absence of the dose-based factor. Interestingly, as can be seen from Fig. 3, the results so obtained were very similar to that obtained with the hybrid objective function.

### ***Head-and-neck IMRT plans***

The two IMRT plans obtained using the newly proposed and the dose-based techniques are summarized in figures 4 and 5. Figure 4 shows the isodose distributions in three transverse slices, one sagittal slice and one coronal slice for the two plans and figure 5 compares the DVHs of the targets and sensitive structures. In figure 5 the solid and dashed lines represent the DVHs obtained using the newly proposed and conventional approaches, respectively. The calculated NTCPs of eyes, optical nerves, optical chiasm, brainstem, spinal cord and parotids for both plans are shown in table V. As seen from the isodose distributions (figure 3) and DVHs (figure 4), with comparable GTV and CTV dose coverage and dose homogeneity, the doses to the sensitive structures are dramatically reduced. The dose reduction is particularly pronounced in the spinal cord, brainstem, parotids, and eyes. For the left and right parotids, for example, the fractional volume receiving a dose above 25 Gy is reduced from 35% to 20% and 15%, respectively. Consistent with the enhanced dosimetric conformality and similar to the prostate case, much steeper dose gradient occurs near the boundary of the target volume. The dose to the non-sensitive structure normal tissue is also less in comparison with the conventional IMRT plan. While the NTCPs of the optical nerves and optical chiasm are small and difficult to draw conclusion, from Table V, it is quite clear that the NTCPs of the eyes, parotids, spinal cord and brainstem are improved significantly. We emphasize once again that the significant improvement in sensitive structure sparing is achieved without deteriorating the dose coverage of the GTV and CTV.

### **Discussion**

The currently available dose-based objective functions do not truly reflect the nonlinear relationship between the dose and the response of tumors and tissues and it is highly desirable to incorporate clinical outcome data in the formulation of inverse planning to guide the plan optimization process. While the dose dependence of a clinical endpoint may be degenerate in the sense that it may be caused by a variety of dose distributions or DVHs, there exists no mechanism in conventional inverse planning to

model the phenomenon. The irradiation of parotid glands mentioned in the Introduction represents an example of this. On the other hand, the conventional objective function may impose some unrealistic degeneracy that is inconsistent with clinical experience. For example, assume that in a treatment plan the prescription dose to the target is 70Gy and that the tumor is divided into two parts with the same volume, one receiving a dose 60Gy and another 80Gy. The penalty values of the two scenarios would be the same according to the conventional quadratic function. Obviously, the two different dose distributions would lead to different outcome. The cold part, which would greatly diminish the tumor control, is more detrimental than the hot spot.

In this paper we have established a general inverse planning framework in which the penalty at a voxel depends not only on the dose deviation from the desired value but also the dose-volume status of the involved organs. The technique circumvents the problems mentioned above and makes it possible to take advantage of the clinical data. Our study shows that the incorporation of existing clinical knowledge can greatly facilitate the inverse planning process and allows us to obtain IMRT plans that would otherwise be unattainable. For the same target dose coverage, we found that the critical structure sparing was substantially improved for both cases. Conversely, the dose to the target volume can be escalated greatly while maintaining the radiation toxicity at the current level. It is remarkable that such the significant improvement is resulted purely from a better modeling of the system. We attribute the significant improvement in dose conformity to the more adequate modeling of the system and the enlarged universe of solution space when the dose-volume effects are taken into account. Physically, we believe that the superior performance of the new formalism arises from the adequate modulation of the voxel dependent weighting induced by the dose-volume factor  $f_\sigma$  (see Eqs. (3) and (4)). In conventional dose-based objective function,  $f_\sigma \equiv 1$ , and a tacit assumption that all points within a structure are equivalent has been made. The use of dose-volume factor  $f_\sigma$  given by Eq. (3) enables us to weight different voxels according to the local doses. In this way, we can effectively "boost" those target regions where the doses are low or penalize more to those sensitive structure regions where the doses are high. The dose-volume induced voxel inequality is an important feature of the new

inverse planning formalism and is the main driving-force in improving the dose distributions.

The use of clinical knowledge can also facilitate the determination of the structure specific importance factors. While the general influence of the importance factors on the solution is known, the specific response of the plan to a variation in the factors is not clear until the dose optimization is done, which necessitates a manual trial-and-error adjustment of the factors to achieve an acceptable tradeoff. The underlying deficiency of the conventional approach is that the importance factors are purely heuristic and lack of physical/clinical meanings. In this work we proposed a new scheme for modeling the tradeoff and develop an algorithm to auto-determine the factors. We wrote the importance factor of an organ into a product of a generic importance and a dose-dependent factor. The latter was related to TCP or NTCP according to Eq. (5). After beam optimization, the dose-dependent factors were increased or decreased according to the values of TCPs/NTCPs. This procedure is similar to that reported by Xing et al (37), where a DVH-based "distance" was used for the assessment of the tradeoff status after each optimization. In reality, other types of plan evaluation indices, such as mean/maximum/ minimum doses, can also be employed for the purpose. We noticed that, with the use of new objective function, the final solution becomes much less sensitive to choice of  $\{r_o^g\}$ . This characteristic of the new formalism may have practical implications in simplifying the inverse planning process.

We should acknowledge that the new technique, just like any other dose response-based technique, may be limited by the scarcity and uncertainty of biological data and the limited predictive power of the TCP/NTCP models. It is important to note, however, that the TCP/NTCP is used as a relative ranking in our plan optimization algorithm instead of a clinical decision-making tool. Because of the phenomenological nature of the modeling, one may further modify the structure specific importance factors manually to achieve a certain clinical goal. The proposed technique can, at least, provide us with a good starting point for the fine-tuning. Our experience, along with the results shown in the above section, indicates that the technique proposed in this work is capable of generating clinically sensible plans and is much more efficient than the manual selection process.

Finally, we mention that the optimality of the dose distributions can also be cast into the realm of equivalent uniform dose (EUD)(20, 21, 27), which is defined as the biologically equivalent dose which, if given uniformly, leads to the same cell killing as the actual non-uniform dose distribution. It is interesting to note that the EUD-based objective function can be regarded as a special case of the general objective function (6).

Indeed, assuming  $EUD = \left( \frac{1}{N} \sum_i D_c^a(i) \right)^{1/a}$ ,  $a = 1/n$ , we can rewrite Eq. (3) into

$$F = \sum_{\tau=1}^{I_{\tau}} r_{\tau} [1 + \eta_1^{\tau} (EUD / EUD_{\tau,ref})^{a_{\tau}} + \eta_2^{\tau} (EUD / EUD_{\tau,ref})^{2a_{\tau}} + \dots] + \sum_{\sigma=1}^{n_{\sigma}} r_{\sigma} [1 + \eta_1^{\sigma} (EUD / EUD_{\sigma,ref})^{a_{\sigma}} + \eta_2^{\sigma} (EUD / EUD_{\sigma,ref})^{2a_{\sigma}} + \dots], \quad (7)$$

which becomes a function of EUD. Different from the EUD-based model, the general hybrid objective function given in Eq. (6) treats the dose-volume effect at a more fundamental voxel level with the actual radiation dose considered, which is more flexible than the EUD defined at a structure level. Because of this, other clinical/dosimetric requirements can be easily integrated. Our study for the prostate case suggests that it is necessary to include the higher order contribution(s) if Eq. (3) or (7) is used to appropriately model a sensitive structure. Alternatively, a hybrid of dose-volume and dose based objective function, as given by Eq. (6), can yield equally good plans. In practice, equation (6) is quite broad and seems to model the inverse planning system effectively. It may also find a natural application in functional image-guided IMRT, where the goal is generally to produce a spatially inhomogeneous dose distribution (33). Finally, we note that the formalism does not involve the prescription of EUD, which could be problematic for practical implementation of an EUD-based model.

## Conclusion

Inverse planning is an important step in IMRT and its performance crucially determines the quality of IMRT treatment plans. In this work, we provide a mechanism for incorporating clinical end point data into inverse treatment planning process and established a clinically practicable inverse planning framework. We employed the



effective volume to take the volumetric effects of the involved organs into account. The new formalism sheds important insight into the problem of therapeutic plan optimization. An algorithm for using computer to aid the determination of structure specific importance factors was also developed. A key step for accomplishing the auto-determination of the importance factors is the decomposition of the conventional importance factor into a generic importance and a dose-dependent component. Two case studies were presented to demonstrate the advantages of the proposed objective function. Comparison of the newly proposed approach with the conventional inverse planning technique indicated that the algorithm is capable of greatly improving the sensitive structure sparing with comparable target dose coverage and homogeneity. Conversely, the dose to the target volume can be escalated greatly while maintaining the radiation toxicity at the current level. Considering the level of improvement of the proposed technique and the fact that it is resulted purely from more intelligent computing algorithm, as apposed to any other exogenous means (e.g., the use of radiosensitizer, whose effects to the patients may not be completely clear), we believe that the potential impact of the work on cancer treatment is significant.

#### **Acknowledgement**

Support from the National Cancer Institute (5 R01 CA98523-02) and Department of Defense (DAMD17-03-1-0023) is gratefully acknowledged.

## Reference

1. Mohan R, Wang X, Jackson A, et al.: The potential and limitations of the inverse radiotherapy technique. *Radiotherapy & Oncology* 1994; 32(3): 232-48.
2. Amols HI, Ling CC: EUD BUT NOT QUD. *International Journal of Radiation Oncology, Biology, Physics* 2002; 52(1): 1-2.
3. Xing L, Li JG, Pugachev A, et al.: Estimation theory and model parameter selection for therapeutic treatment plan optimization. *Medical Physics* 1999; 26(11): 2348-58.
4. Langer M, Brown R, Kijewski P, et al.: The reliability of optimization under dose-volume limits. *Int J Radiat Oncol Biol Phys* 1993; 26(3): 529-38.
5. Langer M, Morrill SS, Lane R: A test of the claim that plan rankings are determined by relative complication and tumor-control probabilities. *Int J Radiat Oncol Biol Phys* 1998; 41(2): 451-7.
6. Deasy JO, Niemierko A, Herbert D, et al.: Methodological issues in radiation dose-volume outcome analyses: summary of a joint AAPM/NIH workshop. *Med Phys* 2002; 29(9): 2109-27.
7. Bortfeld T: Optimized planning using physical objectives and constraints. *Seminars in Radiation Oncology* 1999; 9(1): 20-34.
8. Spirou SV, Chui CS: A gradient inverse planning algorithm with dose-volume constraints. *Medical Physics* 1998; 25(3): 321-33.
9. Xing L, Hamilton RJ, Spelbring D, et al.: Fast iterative algorithms for three-dimensional inverse treatment planning. *Medical Physics* 1998; 25(10): 1845-9.
10. Cho PS, Lee S, Marks RJ, 2nd, et al.: Optimization of intensity modulated beams with volume constraints using two methods: cost function minimization and projections onto convex sets. *Medical Physics* 1998; 25(4): 435-43.
11. Hristov D, Stavrev P, Sham E, et al.: On the implementation of dose-volume objectives in gradient algorithms for inverse treatment planning. *Med Phys* 2002; 29(5): 848-56.
12. Langer M, Morrill S, Brown R, et al.: A comparison of mixed integer programming and fast simulated annealing for optimizing beam weights in radiation therapy. *Med Phys* 1996; 23(6): 957-64.

13. Deasy JO: Multiple local minima in radiotherapy optimization problems with dose-volume constraints. *Medical Physics* 1997; 24(7): 1157-61.
14. Michalski D, Xiao Y, Censor Y, et al.: The dose-volume constraint satisfaction problem for inverse treatment planning with field segments. *Physics in Medicine and Biology* 2004; 49(4): 601-616.
15. Holmes TW, Mackie TR, Reckwerdt P: An iterative filtered backprojection inverse treatment planning algorithm for tomotherapy. *Int J Radiat Oncol Biol Phys* 1995; 32(4): 1215-25.
16. Starkschall G, Pollack A, Stevens CW: Treatment planning using a dose-volume feasibility search algorithm. *Int J Radiat Oncol Biol Phys* 2001; 49(5): 1419-27.
17. Mohan R, Mageras GS, Baldwin B, et al.: Clinically relevant optimization of 3-D conformal treatments. *Medical Physics* 1992; 19(4): 933-44.
18. Brahme A: Optimized radiation therapy based on radiobiological objectives. *Seminars in Radiation Oncology* 1999; 9(1): 35-47.
19. Wang XH, Mohan R, Jackson A, et al.: Optimization of intensity-modulated 3D conformal treatment plans based on biological indices. *Radiotherapy & Oncology* 1995; 37(2): 140-52.
20. Thieke C, Bortfeld T, Niemierko A, et al.: From physical dose constraints to equivalent uniform dose constraints in inverse radiotherapy planning. *Med Phys* 2003; 30(9): 2332-9.
21. Wu Q, Mohan R, Niemierko A, et al.: Optimization of intensity-modulated radiotherapy plans based on the equivalent uniform dose. *Int J Radiat Oncol Biol Phys* 2002; 52(1): 224-35.
22. Wu Q, Djajaputra D, Wu Y, et al.: Intensity-modulated radiotherapy optimization with gEUD-guided dose-volume objectives. *Phys Med Biol* 2003; 48(3): 279-91.
23. Kallman P, Lind BK, Brahme A: An algorithm for maximizing the probability of complication-free tumour control in radiation therapy. *Physics in Medicine & Biology* 1992; 37(4): 871-90.
24. Niemierko A, Goitein M: Modeling of normal tissue response to radiation: the critical volume model. *International Journal of Radiation Oncology, Biology, Physics* 1993; 25(1): 135-45.

25. Webb S, Nahum AE: A model for calculating tumour control probability in radiotherapy including the effects of inhomogeneous distributions of dose and clonogenic cell density. *Physics in Medicine & Biology* 1993; 38(6): 653-66.
26. Brahme A: Individualizing cancer treatment: biological optimization models in treatment planning and delivery. *Int J Radiat Oncol Biol Phys* 2001; 49(2): 327-37.
27. Niemierko A: Reporting and analyzing dose distributions: a concept of equivalent uniform dose. *Medical Physics* 1997; 24(1): 103-10.
28. Lyman JT, Wolbarst AB: Optimization of radiation therapy, III: A method of assessing complication probabilities from dose-volume histograms. *International Journal of Radiation Oncology, Biology, Physics* 1987; 13(1): 103-9.
29. Kutcher GJ, Burman C: Calculation of complication probability factors for non-uniform normal tissue irradiation: the effective volume method. *International Journal of Radiation Oncology, Biology, Physics* 1989; 16(6): 1623-30.
30. Eisbruch A, Ten Haken RK, Kim HM, et al.: Dose, volume, and function relationships in parotid salivary glands following conformal and intensity-modulated irradiation of head and neck cancer. *International Journal of Radiation Oncology, Biology, Physics* 1999; 45(3): 577-87.
31. Niemierko A, Goitein M: Calculation of normal tissue complication probability and dose-volume histogram reduction schemes for tissues with a critical element architecture. *Radiotherapy & Oncology* 1991; 20(3): 166-76.
32. Schultheiss TE, Orton CG, Peck RA: Models in radiotherapy: volume effects. *Medical Physics* 1983; 10(4): 410-5.
33. Xing L, Cotrutz C, Hunjan S, et al.: Inverse planning for functional image-guided intensity-modulated radiation therapy. *Phys Med Biol* 2002; 47(20): 3567-78.
34. Burman C, Kutcher GJ, Emami B, et al.: Fitting of normal tissue tolerance data to an analytic function. *Int J Radiat Oncol Biol Phys* 1991; 21(1): 123-35.
35. Emami B, Lyman J, Brown A, et al.: Tolerance of normal tissue to therapeutic irradiation. *International Journal of Radiation Oncology, Biology, Physics* 1991; 21(1): 109-22.
36. Xing L, Chen GTY: Iterative algorithms for Inverse treatment planning. *Physics in Medicine & Biology* 1996; 41(2): 2107-23.

37. Xing L, Li JG, Donaldson S, et al.: Optimization of importance factors in inverse planning. *Physics in Medicine & Biology* 1999; 44(10): 2525-36.

**Table I** The radiological parameters for various sensitive structures used in this study

Sensitive structures	$n$	$m$	$D_{50/5}$ (Gy)	$D_{5/5}$ (Gy)
Bladder	0.50	0.11	80	65
Rectum	0.12	0.15	80	60
Femoral head	0.25	0.12	65	52
Eye lens	0.3	0.27	18	10
Optic nerve	0.25	0.14	65	50
Optic chiasm	0.25	0.14	65	50
Spinal cord	0.05	0.175	66.5	47
Brainstem	0.16	0.14	65	50
Parotid	0.70	0.18	46	32

**Table II** Summary of the optimization parameters used in the dose-based and proposed approaches for the prostate case

Organs	The dose-based approach		The proposed approach
	Relative importance factors	Target prescription and OAR tolerance doses (Gy)	Generic importance factors ( $r_{\sigma}^g$ )
Target	5.0	78	5
Bladder	1.2	48	2
Rectum	1.8	43	2
Femoral head (R)	1.0	32	1
Femoral head (L)	1.0	32	1
Normal tissue	0.5	65	0.3

**Table III** Summary of the optimization parameters used in the dose-based and proposed approaches for the Head-and-neck case

Organs	The dose-based approach		The proposed approach
	Relative importance factors	Target prescription and OAR tolerance doses (Gy)	Generic importance factors ( $r_{\sigma}^g$ )
GTV	3.0	70	4.0
CTV	4.0	62	6.0
Spinal cord	2.0	30	3.0
Brainstem	1.5	30	2.0
Left optic nerve	1.0	25	1.0
Right optic nerve	1.0	25	1.0
Left Eye	2.0	6	3.0
Right Eye	2.0	6	3.0
Left parotid	1.2	25	1.0
Right parotid	1.2	25	1.0
Optic chiasm	1.0	25	1.0
Normal tissue	0.5	40	0.5

**Table IV** Comparison of the normal tissue complication probabilities (NTCP) for the two IMRT plans for the prostate case

NTCP (%)	The dose-based IMRT plan	The proposed IMRT plan
Bladder	0.017	0.00030
Rectum	0.45	0.029
Femoral head (R)	0.000076	0.0000038
Femoral head (L)	0.000032	0.000015

**Table V** Comparison of the normal tissue complication probabilities (NTCP) for the two IMRT plans for the head-and-neck case

NTCP (%)	The dose-based IMRT plan	The proposed IMRT plan
Spinal cord	0.043	0.0025
Brainstem	0.012	0.0040
Left Eye	0.27	0.18
Right Eye	0.24	0.12
Left parotid	0.21	0.056
Right parotid	0.22	0.064
Optic chiasm	0.00024	0.00064
Left optic nerve	0.000064	0.0000075
Right optic nerve	0.000043	0.000025



## Legends

Fig. 1. A flow chart of the proposed optimization process.

Fig. 2. Comparison of the isodose distributions of the two prostate IMRT plans: (a) the conventional dose-based approach; (b) the newly proposed approach. The results on two transverse slices and a sagittal slice are shown.

Fig. 3. Comparison of Dose Volume Histograms (DVHs) of the prostate IMRT plans obtained using the proposed approach (solid curves) and the conventional dose-based approach (dash lines). The dotted curves represent the results obtained with  $k_r=4$  and  $k_o=2$  in Eq. (6). The dash-dotted curves are the DVHs with  $k_r=2$  and  $k_o=0$  (a higher order term, the third term in Eq. (3), was included during the optimization).

Fig. 4. Comparison of the isodose distributions of the two head-and-neck IMRT plans: (a) the conventional dose-based approach; (b) the newly proposed approach. The results on three transverse slices, one sagittal slice and one coronal slice are shown.

Fig. 5. Comparison of the Dose Volume Histograms (DVHs) of the two head-and-neck IMRT plans obtained using our newly proposed approach (solid curves) and the conventional dose-based approach (dash lines).

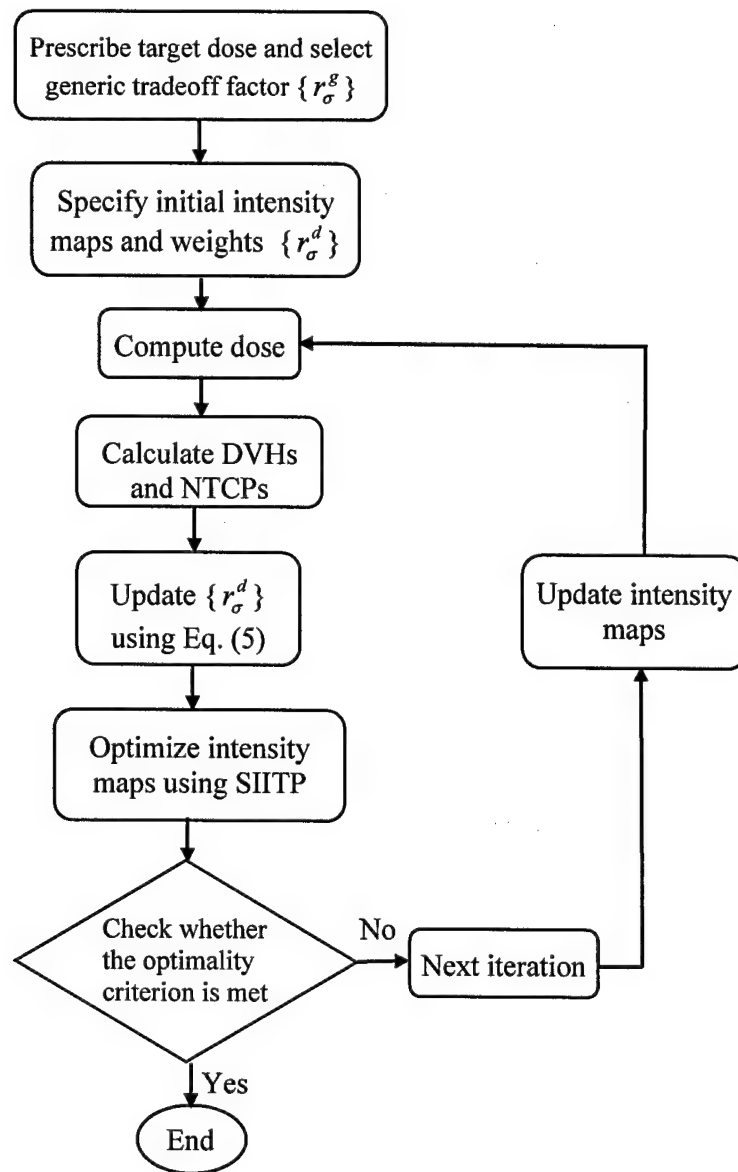
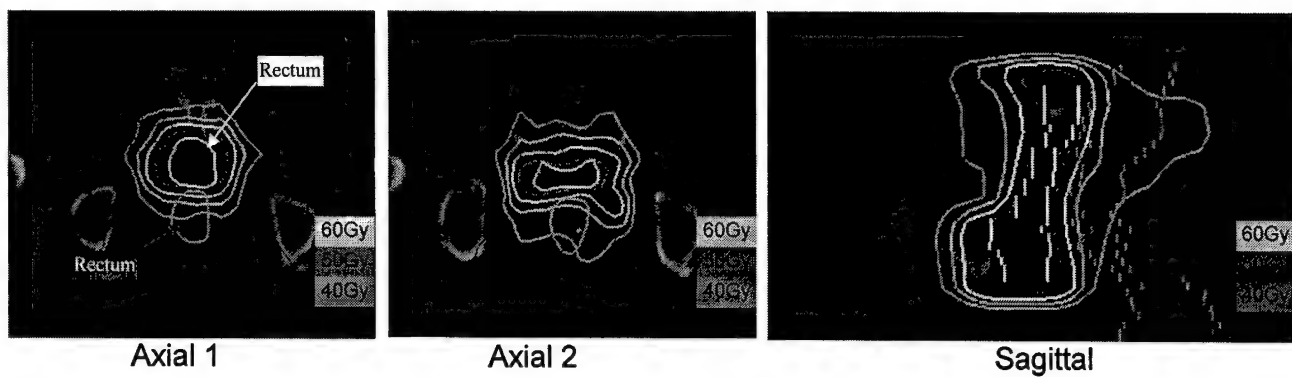
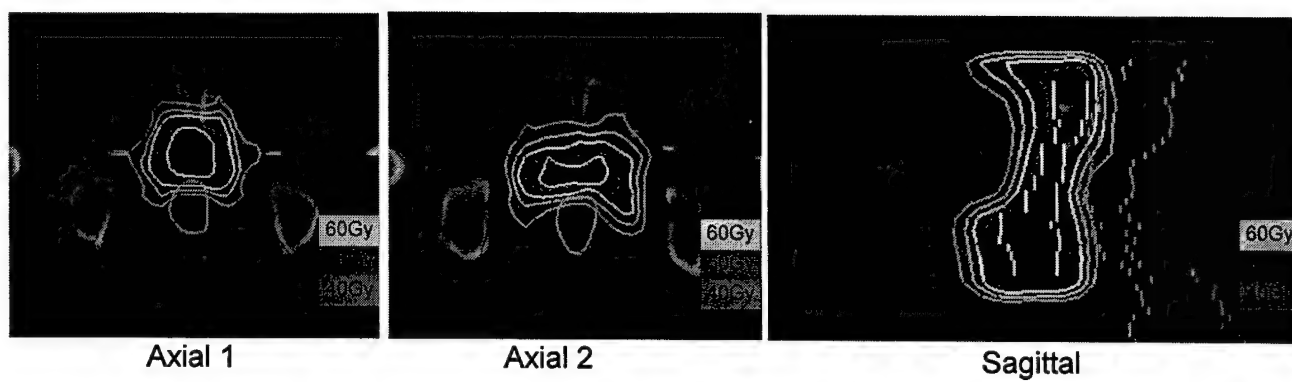


Figure 1

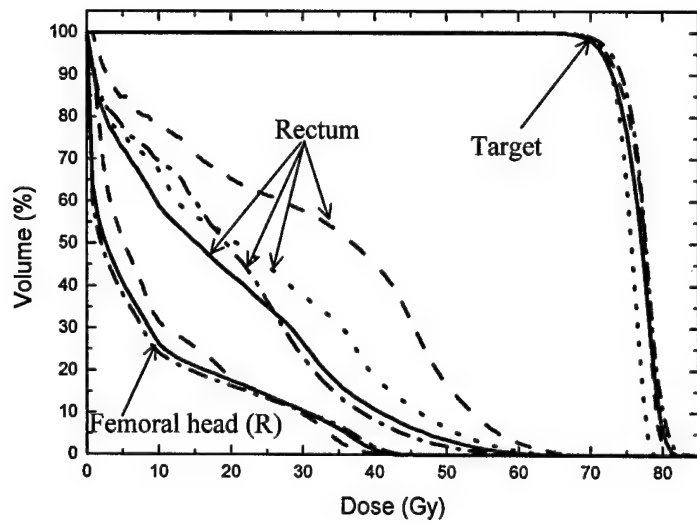


(a)

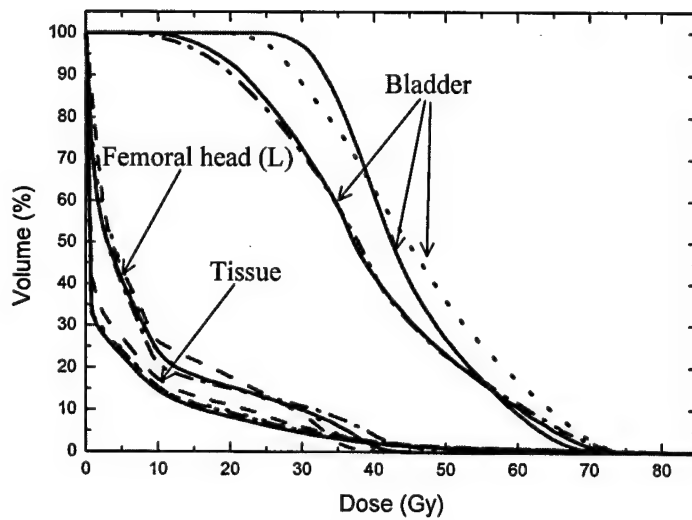


(b)

Figure 2



(a)



(b)

Figure 3

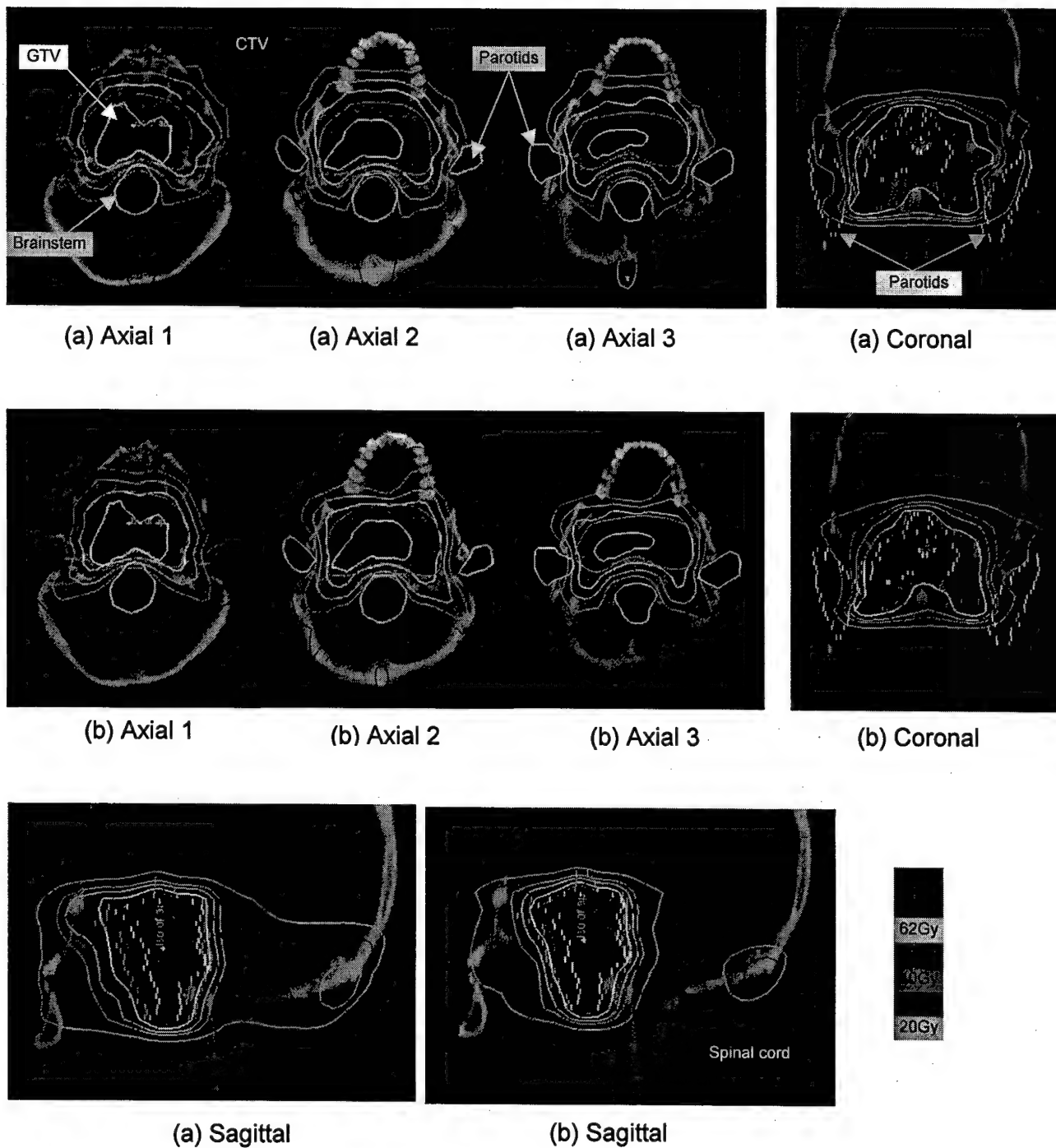
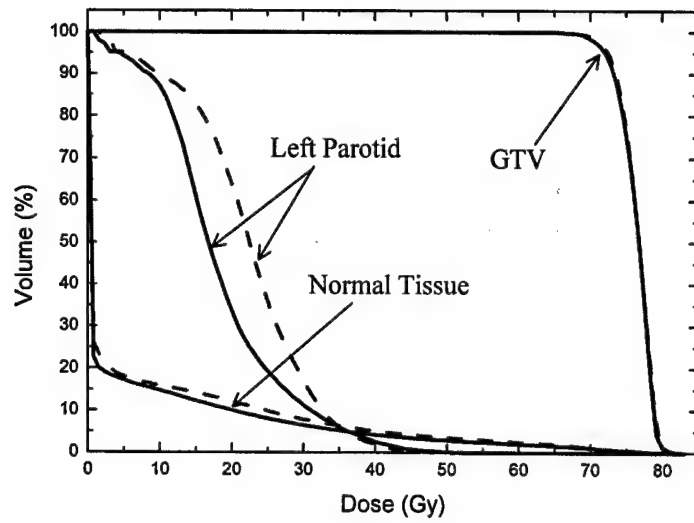
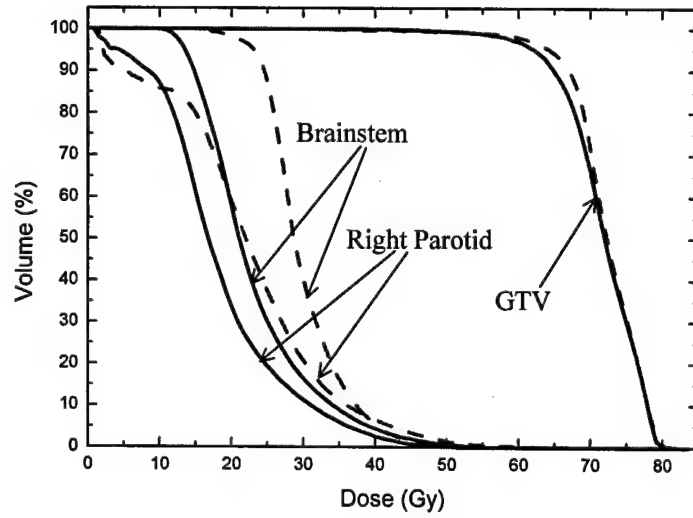


Figure 4

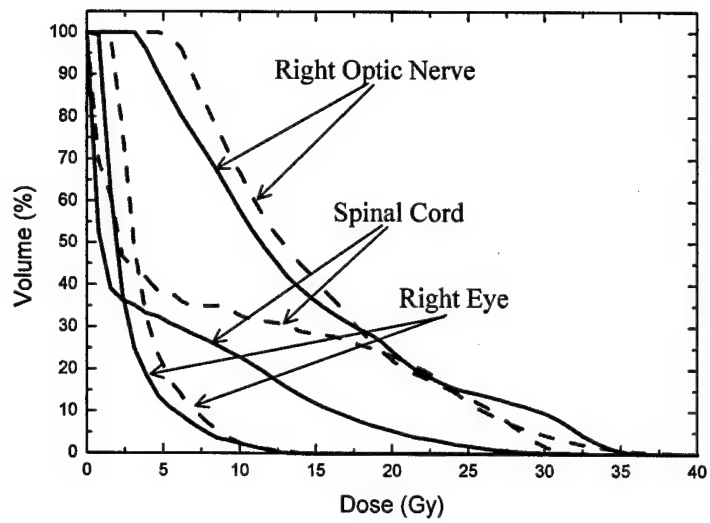


(a)

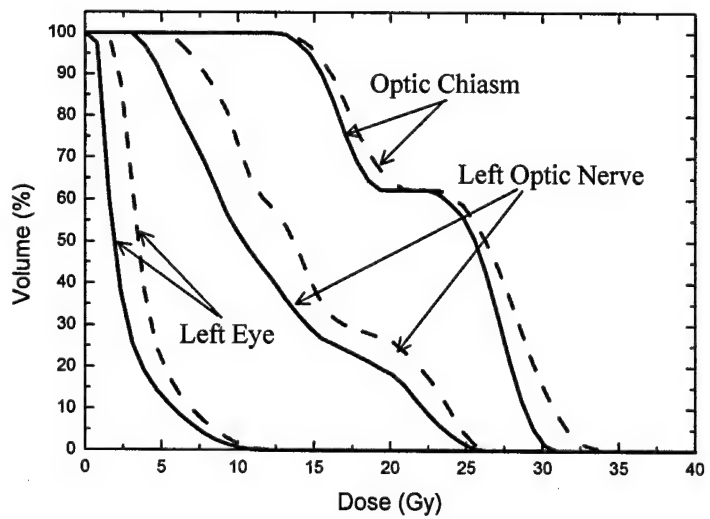


(b)

Figure 5



(c)



(d)

Figure 5

# **In-vivo Detection of Citrate for Prostate Cancer at 3 Tesla**

DONG-HYUN KIM<sup>1</sup>, DIRK MAYER<sup>1</sup>, LEI XING<sup>2</sup>, BRUCE DANIEL<sup>1</sup>,  
DANIEL MARGOLIS<sup>1</sup>, DANIEL SPIELMAN<sup>1</sup>

<sup>1</sup>Radiological Sciences Laboratory

Department of Radiology

<sup>2</sup> Department of Radiation Oncology

Stanford University

Stanford, California

**Running head:** Citrate at 3T

**Correspondence to:**

Dong-hyun Kim

Lucas MRS Imaging Center

Stanford CA 94305-5488

(650) 498-5461

fax: (650) 723-5795

email: dhkim@stanford.edu



## Abstract

The detection of Citrate at main magnetic field of 3 Tesla is investigated. Citrate is an important metabolite often used to aid the detection of Prostate Cancer but the behavior of the metabolite is complicated due to its strong coupling effects at this field strength. We show simulations illustrating the behavior of the resonance with data measured from phantom and in vivo. Echo times of approximately 80 ms – 100 ms gave maximum peak amplitude and energy of the metabolite using PRESS excitation. We also show simulations using 2D J-resolved single voxel spectroscopy, which provides robust detection. Phantom and in vivo data are presented to illustrate the spectral pattern of the J-resolved Citrate metabolite.

**Key words:** citrate; 2D J-resolved spectroscopy, prostate cancer.

## 1 INTRODUCTION

Citrate is an important metabolite often used in Magnetic Resonance Spectroscopy (MRS) and MR Spectroscopic Imaging (MRSI) to aid the detection of Prostate Cancer (PCa) along with the Choline and Creatine metabolites (1). In addition to the morphological information provided by MR Imaging (MRI), the additional information gained using MRS/MRSI increases the specificity of the examination. In these exams, the level of (Choline + Creatine)/Citrate is regarded as a marker for PCa (2). To date, MRSI protocols for PCa detection have been well established at main magnetic field strength of 1.5 Tesla (T) (3).

The advent of higher field strength scanners provide many new extensions from previous 1.5T systems due to the inherent increase in the signal to noise ratio (SNR). For PCa exams using MRS/MRSI methods, this advantage can be exploited in various forms, which include using higher spatial resolution acquisitions to increase the accuracy of localization of the cancerous tissues. Scan times can also be made shorter compared to 1.5T for the same SNR thereby reducing the overall MR exam time. The extension of 1.5T MRSI protocols for usage in 3T PCa can therefore provide potential merits.

However, the process of advancing to higher field strength accompanies additional technical considerations. For clinical prostate examinations using spectroscopic techniques, one of the major issues that arise involves the detection of the Citrate resonance. While coupling effects can be largely neglected at 1.5T, the dominance of the strong coupling for the Citrate resonance at 3T needs consideration in selecting the acquisition parameters if reliable detection of the metabolite is desired. At 3T, the J-coupling constant is closely tied with the chemical shift constant of the metabolite thereby causing dependence of the spectra as a function of echo time (TE) (4). Constraints in the radio frequency (RF) field can also exist when using body coil excitation thereby further compromising the data acquisition. Therefore, close investigation of the behavior of the Citrate resonance needs to be studied as well as careful

considerations in selecting the image protocols.

This study involves the study of different spectral patterns associated with the Citrate resonance at 3T. We show the dependance as a function of the echo time using simulations based on the full density matrix calculation and using phantom measurements for comparison. Single voxel in vivo spectroscopic data are acquired using echo times selected from simulations that maximizes the detection criteria. Furthermore, we explore the use of 2D J-resolved single voxel spectroscopic sequence (5) to provide robust detection of the Citrate metabolite and to illustrate the characteristics of the J-resolved spectral pattern. Simulations and measurements are performed with phantom while in vivo data are collected using the J-resolved sequence. This study is intended to provide a guideline in selecting pulse sequence protocols for MR spectroscopy to aid the diagnosis of PCa detection at 3T.

## 2 METHODS

Simulations were performed for the Citrate metabolite by solving the full density matrix of strongly coupled two-spin system (6). Different echo time acquisitions were simulated assuming a PRESS excitation scheme. The timing of the acquisition of the PRESS sequence was assumed to be  $90^\circ - [t_{12}] - 180^\circ - [TE/2] - 180^\circ - [TE/2 - t_{12}] -$  acquisition, where TE was incremented to encode echo timing dependance (7). For our PRESS sequence, we prescribed  $t_{12}$  to be 10 ms. We assumed the J-coupling constant to be 15.4 Hz with chemical shift of 0.12 ppm (=16.6 Hz at 3T) for simulations (8). The T2 value was assumed to be 200 ms with a line width of 10 Hz. The simulations were conducted for echo times starting from 30 ms and ending at 400 ms with 10 ms intervals.

Quantification of the simulations were conducted using two different quantification metrics. Firstly, the peak amplitude at the center of the spectrum (2.6 ppm peak) was

calculated as a function of echo time. Secondly, the energy was calculated by integrating the square of the spectrum. Another set of simulations were performed which relates to the power constraints in the RF excitation encountered in in vivo cases. In such situations, reduced flip angle techniques are often required (9). Therefore, we quantified the simulations for the case of using  $90^\circ$ - $180^\circ$ - $180^\circ$  flip angle excitation as well as for the case of using a  $90^\circ$ - $167^\circ$ - $167^\circ$  excitation often used in in vivo examinations. Experimental data were acquired from a Citrate phantom using the PRESS sequence with the same time settings. All phantom and in vivo measurements were also made with this reduced flip angle. Data from different echo times were acquired with a 3 second repetition time (TR) and were similarly quantified to compare with the simulations. All data were acquired on a 3T Signa scanner (GE Medical Systems, Waukesha, WI).

In vivo data from a subject suspicious of PCa were acquired using the echo time that indicated the maximum amplitude and energy of the Citrate metabolite from the simulation and phantom measurement results. From the quantification results, this echo time for maximum detection was in the range of 80-100 ms. Echo times below 50 ms were discarded due to reasons given in the discussion section. Therefore in vivo single voxel spectroscopy data were acquired with an echo time of 90 ms. Data were acquired for 8 minutes from a voxel of size 1.5 cc for adequate SNR. All in vivo data were acquired using the body coil for excitation followed by an endorectal coil signal reception (10). All in vivo studies were conducted under IRB guidelines and with informed consent.

Simulations and phantom measurements were also conducted for a 2D J-resolved acquisition. In both cases, the echo time spacing were adjusted to be 7.8 ms for a total of 64 steps from 35 ms to 534 ms for finer resolution in the F1 domain. This resulted in a 2 Hz spectral resolution with a bandwidth of 128 Hz in the F1 domain. The spectral bandwidth for F2 was 5000 Hz with 2048 data point acquisitions. For the actual 2D J-resolved measurements, a phantom composed of Citrate, Creatine,

and Choline metabolites were used to emulate the existence of cancerous tissue.

Finally, in vivo data were collected from a subject suspicious of PCa using the 2D J-resolved technique. Single voxel 2D J-resolved spectroscopic data were acquired from two different regions at the peripheral zone of the prostate. The parameters were maintained as with the simulations. The voxel size chosen was  $1\text{cm} \times 1.12\text{cm} \times 1.08\text{cm} = 1.2\text{cc}$ . Four acquisitions were averaged per echo time for a total scan time of 8 minutes ( $\text{TR} = 2\text{sec}$ ) for each voxel.

### 3 RESULTS

Figure 1 shows the Citrate resonance behavior at different echo times obtained from the PRESS excitation simulation. Unlike 1.5T, due to the strong coupling effects, very different resonant behavior can be observed at 3T as a function of echo time. The center of the spectrum can be seen to have a peak at very short echo time of 30 ms, a negative peak near 90 ms echo time, and returning to a positive peak near 270 ms but at a reduced amplitude due to the T2.

Figure 2 quantifies the simulation and measurement results by calculating the relative peak value at the 2.6 ppm location (left) and the energy of the metabolite (right). For each quantification metric, simulations assuming  $180^\circ$  flip angle (circled line), simulations assuming reduced flip angle excitation (squared line), and phantom measurement results (crossed line) are shown. Line characteristics of the measured data obtained from the phantom are seen to closely resemble the results obtained from the simulations although the dynamic range is smaller, which could be due to inhomogeneities or other inaccurate modelling of the metabolite. In both quantifications however, a local peak can be obtained with echo time of approximately 80 ms - 100 ms.

In Fig. 3, in vivo single voxel measurement data acquired with 90 ms echo time is

presented. The excited region is shown on the T2 weighted anatomical image (left) with the reconstructed spectrum. The presence of Creatine and Choline resonances can be seen along with the clearly visible inverted peak of the Citrate metabolite near the 2.6 ppm region.

Figure 4 shows the simulated 2D J-resolved Citrate spectra (right) along with 2D J-resolved data acquired with a phantom (left) containing Citrate as well as Choline and Creatine metabolites for different F1 lines. In both cases, due to the modulations occurring as a function of echo time, resonances are clearly seen beyond the J(0) line. The spectra for both cases have very similar spectral patterns. In both cases, the J(0) line has a slight negative peak at the Citrate position which is due to the strong negative peaks at echo times of 60 – 120 ms.

Finally, two single voxel 2D J-resolved spectra from in vivo subject are given in Fig. 5. The two regions that were selected are shown in the anatomical T2 weighted image given along with the 2D J-resolved spectra. The spectra obtained from the right side of the subject (a) displays negligible Citrate metabolite intensity compared with Creatine and Choline resonances. Compared to this spectra, the 2D J-resolved spectra from the left side of the subject (b) reveals the presence of Citrate along with the Creatine and Choline metabolites. The Citrate metabolite can be seen more visibly from the modulations occurring in the F1 lines. These two comparisons show that with the 2D J-resolved acquisition method, the strongly coupled Citrate metabolite can be resolved while the presence of the metabolite can be confirmed robustly.

## 4 DISCUSSION

The successful application of PCa detection using MRS/MRSI at 3T depends on the proper choice of pulse sequence parameters based on the knowledge of the Citrate

resonance behavior. As seen from Figs. 1 and 2, to maximize the resonance amplitude and/or energy, good choices of TE would be below 35 ms or in the range of 80 - 100 ms. In the former case, practical issues pertaining to minimizing lipid contamination using saturation pulses and eliminating macromolecular contributions need to be established. Also, hardware instabilities at short echo times, for example gradient modulations or eddy current errors can deteriorate the quality of the data acquired. Meanwhile, at echo times between 80 - 100 ms, lipid contamination can be reduced while hardware instabilities can be less problematic. Therefore, in the case of using a fixed echo time for spectroscopy, this range of echo times can be advantageous.

We used two different metrics in quantifying the Citrate resonance. Namely, the peak amplitude at the center of the spectrum and the energy of the metabolite, defined by the integral of its square over the spectral width. Other different methods of criteria for evaluating the outcome can also be established. For example, in the case of poor  $B_0$  homogeneity, line broadening can cause spectral overlap. Calculating the energy can be less than helpful in this situation while negative peaks can be obscured. Rather, obtaining the energy of the main central lobe can give more robust results in such cases.

The same criteria used here can result in different optimal echo times depending on the pulse sequence parameters. For example, simulations assuming a  $90^\circ$ -[TE/4]- $180^\circ$ -[TE/2]- $180^\circ$ -[TE/4]-acq PRESS sequence resulted in maximum (negative) amplitude and energy at a slightly shorter echo time near the 75 ms range. More broadly speaking, different spectroscopic sequences such as J-PRESS (4) or STEAM (11) can require different parameter setting. Finally, restrictions in the RF field can also yield different results which is a nontrivial practical issue. Even with the simulations at reduced flip angles to address peak limitation issues, the  $B_1$  inhomogeneity can still be in effect causing parameter settings to be suboptimal. Methods to reduce RF inhomogeneity and power constraints is highly desirable (12, 13).

An alternate and more robust method for detection of Citrate is to use J-resolved

spectroscopic sequences as we have demonstrated here. In this case, the presence of the citrate metabolite is well demonstrated at lines beyond  $J(0)$ , which provides robustness in the estimation of the presence of the metabolite. Other metabolites used as markers of PCa can be observed in the  $J(0)$  line. In addition to the benefit of resolving the J-coupling for the detection of Citrate, it has been shown that J-resolved spectroscopy can further differentiate other metabolites, for example, polyamines which co-resonate near the Creatine and Choline peaks (14, 15). This eventually leads to additional physiologic information concerning the prostate tissue. Furthermore, J-resolved spectroscopy has been used to reduce sidebands artifacts (16, 17). The acquisitions from multiple echo times can also help determine the  $T_2$  of the metabolites of interest as well as the water content(14).

For application of J-resolved techniques in the clinical settings, a means of quantifying the amount of the Citrate metabolite needs to be established. Due to the modulation of the citrate resonance shape as a function of echo time, a straight forward method of quantifying the amount is not available. Rather, the relative amount can be inferred from the peaks at  $J(\pm 4)$ ,  $J(\pm 8)$ , or other lines in F1 using a model based approach.

A clinically more useful examination using J-resolved spectroscopy would be to have information regarding the spatial distribution of the metabolites. Using straight forward phase encoding methods for gathering spatial information can lead to increased scan time not suitable for in vivo studies. To overcome these issues, clever choice of pulse sequence parameters needs to be made. For example, a multiple spin echo sequence can be used to collect additional echo time data from one excitation pulse. Also, since the Citrate resonance is mostly concentrated near the center of the  $J(0)$  line, adjusting the sampling can be used to effectively decrease the scan without deteriorating the spectra by using undersampling or variable rate sampling techniques (18). Another alternative method to increasing spatial information is to use time varying readout gradients (19, 20). It has been shown that using read-



out gradients can dramatically decrease the minimum total scan time. This can be effectively used to gain the additional information needed for J-resolved techniques.

## 5 CONCLUSION

An analysis of the Citrate metabolite, which is useful for the detection of Prostate cancer, using full density matrix has been conducted for applications at 3T. Phantom results are provided for comparison. Using peak estimate and energy calculations, echo time in the range of 80 – 100 ms gave maximum results suggesting single voxel or chemical shift imaging experiments using PRESS excitation to be conducted at this echo time. Also, we have shown that 2D J-resolved spectroscopy provides an elegant method to detect the Citrate metabolite effectively. Strong coupling which leads to modulations as a function of echo time is easily observed using 2D J-resolved spectroscopic sequences. In vivo measurements confirms the observation of Citrate with patterns similar to simulation and phantom studies.

## 6 ACKNOWLEDGMENTS

We gratefully acknowledge the support from GE Medical Systems, Lucas Foundation, NIH CA 48269, PR09784, 1R01 CA098523-01, DOD DASMD17-03-1-0023.

## REFERENCES

1. L. .C. Costello, R. B. Franklin, and P. Narayan. Citrate in the diagnosis of prostate cancer. The Prostate, 38:237–245, 1999.
2. J. Scheidler, H. Hricak, D. B. Vigneron, K. K. Yu, D. L. Sokolov, R. L. Huang, C. J. Zaloudek, S. J. Nelson, P. R. Carroll, and J. Kurhanewicz. 3D  $^1\text{H}$ -MR

- spectroscopic imaging in localizing prostate cancer: clinico-pathologic study. Radiology, 213:473-480, 1999.
3. J. Kurhanewicz, D.B. Vigneron, H. Hricak, P. Narayan, P. Carroll, and S.J. Nelson. Three-dimensional  $^1\text{H}$  MR spectroscopic imaging of the in situ human prostate with high (0.24-0.7  $\text{cm}^3$ ) spatial resolution. Radiology, 198:795-805, 1996.
  4. R. V. Mulkern, J. L. Bowers, S. Peled, R. A. Kraft, and D. S. Williamson. Citrate signal enhancement with a homonuclear J-refocusing modification to double-echo PRESS sequences. Magn Reson Med, 36:775-780, 1996.
  5. M. A. Thomas, L. Ryner, M. Metha, P. Turski, and J. A. Sorenson. localized 2D J-resolved  $^1\text{H}$  MR spectroscopy of human brain tumors in vivo. J Magn Reson Imaging, 6:453-459, 1996.
  6. P. J. Hore, J. A. Jones, and S. Wimperis. NMR: The toolkit. oxford science publications, 2000.
  7. L. N. Ryner, J. A. Sorenson, and M. A. Thomas. Localized 2D J-resolved  $^1\text{H}$  MR spectroscopy: strong coupling effects in vitro and in vivo. Magn Reson Imaging, 13(6):853-869, 1995.
  8. F. Schick, H. Bongers, S. Kurz, W. Jung, M. Pfeffer, and O. Lutz. Localized proton MR spectroscopy of citrate in vitro and of the human prostate in vivo at 1.5T. Magn Reson Med, 29:38-43, 1993.
  9. T. Raidy, N. Sailasuta, R. E. Hurd, and J. M. Pauly. Application of reduced flip angle 180 RF pulses in PRESS. Proceedings of the 2th Scientific Meeting of the International Society for Magnetic Resonance in Medicine, page 1020, 1995.
  10. B. L. Daniel, C. Dumoulin, R. Watkins, K. Rohling, R. Giaquinto, J. Presti, K. Butts, R. Bammer, and M. Moseley. 3 Tesla imaging of the prostate

- with a rigid endorectal coil. Proceedings of the 11th Scientific Meeting of the International Society for Magnetic Resonance in Medicine, page 1462, 2003.
11. R. B. Thompson and P. S. Allen. Response of metabolites with coupled spins to the STEAM sequence. Magn Reson Med, 45:955–965, 2001.
  12. C. H. Cunningham, G. A. Wright, D. B. Vigneron, and J. M. Pauly. Correction for RF inhomogeneity for improved spatial saturation. Proceedings of the 11th Scientific Meeting of the International Society for Magnetic Resonance in Medicine, page 1135, 2003.
  13. S. Conolly, G. Glover, D. Nishimura, and A. Macovski. A reduced power selective adiabatic spin-echo pulse sequence. Magn Reson Med, 18:28–38, 1991.
  14. M.G. Swanson, D.B. Vigneron, T-K.C. Tran, N. Sailasuta, R.E. Hurd, and J. Kurhanewicz. Single-voxel oversampled j-resolved spectroscopy of in vivo human prostate tissue. Magn Reson Med, 45:973–980, 2001.
  15. K. Yue, A. Marumoto, N. Binesh, and M. A. Thomas. 2D JPRESS of human prostates using an endorectal receiver coil. Magn Reson Med, 47(6):1059–1064, 2002.
  16. R.E. Hurd, D. Gurr, and N. Sailasuta. Proton spectroscopy without water suppression: the oversampled j-resolved experiment. Magn Reson Med, 40:343–347, 1998.
  17. P.J. Bolan, L. DelaBarre, E.H. Baker, H. Merkle, L.I. Everson, D. Yee, and M. Garwood. Eliminating spurious lipid sidebands in  $^1\text{H}$  MRS of breast lesions. Magn Reson Med, 48:215–222, 2002.
  18. B. Kuhn, W. Dreher, D. Leibfritz, and M. Heller. Homonuclear uncoupled  $^1\text{H}$  spectroscopy of the human brain using weighed accumulation schemes. Magn Reson Imaging, 8:1193–1201, 1999.

19. E. Adalsteinsson and D. M. Spielman. Spatially resolved two-dimensional spectroscopy. Magn Reson Med, 41:8–12, 1999.
20. D. Mayer, D. H. Kim, E. Adalsteinsson, and D. M. Spielman. Fast CT-PRESS based spiral CSI at 3T. Proceedings of the 12th Scientific Meeting of the International Society for Magnetic Resonance in Medicine, 2004.

## Table and Figure Captions

Figure 1. Citrate metabolite characteristics for different echo times at 3T. The Citrate resonance behavior was simulated assuming a PRESS excitation with J-coupling constant of 15.4 Hz and chemical shift value of 0.12 ppm (16.6 Hz at 3T). The behavior is very different from 1.5 T due to the strong coupling effects. The central lobe modulates as a function of echo time, with positive peak at short  $TE \approx 30$  ms followed by a negative peak near the 90 ms range. Another positive peak can be observed at 270 ms range but decreased in intensity due to T2 effects, which was assumed to be 200 ms.

Figure 2. Quantitative results obtained from simulations and measurement from phantom as a function of echo time. Graphs are plotted for simulated results assuming  $90^\circ$ - $180^\circ$ - $180^\circ$  excitation ( $\circ$ ), simulated results assuming reduced flip angle  $90^\circ$ - $167^\circ$ - $167^\circ$  excitation ( $\diamond$ ), and measured data acquired from phantom ( $\times$ ). Left) value of center peak of the spectrum at 2.6 ppm. Right) energy of the Citrate spectrum. The comparison in both cases shows good agreement between the simulations and phantom measurements. Also, it provides a good guideline for selecting the echo time for Citrate metabolite detection. In both cases, echo times near 80 – 100 ms range have a local peak.

Figure 3. In vivo single voxel spectroscopy measurement. Measurement region was selected from the T2 weighted anatomic image as shown using the PRESS sequence at an echo time of 90 ms where an inverted peak of the Citrate metabolite should be observed. As the result spectrum suggests, the presence of the Citrate metabolite can be seen at the 2.6 ppm region as an inverted peak. Other metabolites of interest for detection of PCa, namely the Creatine and Choline peaks can also be observed.

Figure 4. 2D J-resolved spectra obtained from simulations (right) and phantom measurements (left) at 3T using the PRESS sequence. The echo time interval was 7.8

ms starting from 35 ms for 64 steps. For the phantom measurement, Choline and Creatine metabolites were added to mimic PCa. Due to modulations as a function of echo time, the J-resolved spectra show strong signal of the Citrate metabolite at lines outside of  $J(0)$ . Simulated J-resolved spectra and phantom measured J-resolved spectra are shown with similar spectral patterns. In this respect, the detection of the Citrate resonance can be made robustly using J-resolved acquisitions.

Figure 5. Single voxel 2D J-resolved spectroscopy results obtained from an in vivo subject suspicious of PCa. Two voxels were selected for the single voxel examinations as shown in the T2 weighted anatomical images. The corresponding J-resolved spectra are shown on the bottom of each image. In (a), even though the presence of Creatine and Choline metabolites are evident, there is no visible Citrate. As for the region shown in (b), the Citrate resonance is visible (2.6 ppm region from  $J(-10)$  to  $J(10)$  line) in the J-resolved spectra while other metabolites are also present. This shows the J-resolved spectroscopy can be useful for the detection of the Citrate metabolite as well as other metabolites of interest in the detection of PCa.

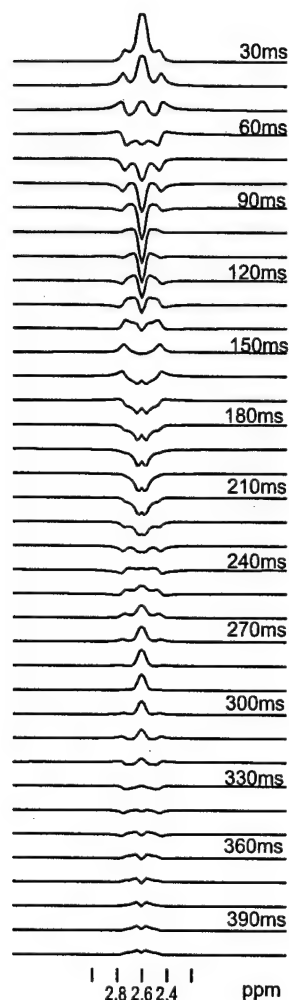


Figure 1: Citrate metabolite characteristics for different echo times at 3T. The Citrate resonance behavior was simulated assuming a PRESS excitation with J-coupling constant of 15.4 Hz and chemical shift value of 0.12 ppm (16.6 Hz at 3T). The behavior is very different from 1.5 T due to the strong coupling effects. The central lobe modulates as a function of echo time, with positive peak at short  $TE \approx 30$  ms followed by a negative peak near the 90 ms range. Another positive peak can be observed at 270 ms range but decreased in intensity due to T2 effects, which was assumed to be 200 ms.

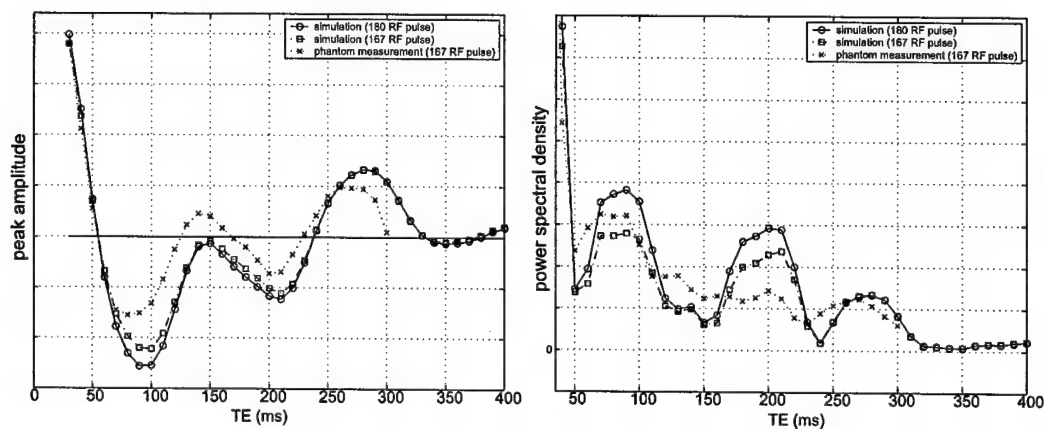


Figure 2: Quantitative results obtained from simulations and measurement from phantom as a function of echo time. Graphs are plotted for simulated results assuming  $90^\circ$ - $180^\circ$ - $180^\circ$  excitation ( $\circ$ ), simulated results assuming reduced flip angle  $90^\circ$ - $167^\circ$ - $167^\circ$  excitation ( $\diamond$ ), and measured data acquired from phantom ( $\times$ ). Left) value of center peak of the spectrum at 2.6 ppm. Right) energy of the Citrate spectrum. The comparison in both cases shows good agreement between the simulations and phantom measurements. Also, it provides a good guideline for selecting the echo time for Citrate metabolite detection. In both cases, echo times near 80 – 100 ms range have a local peak.



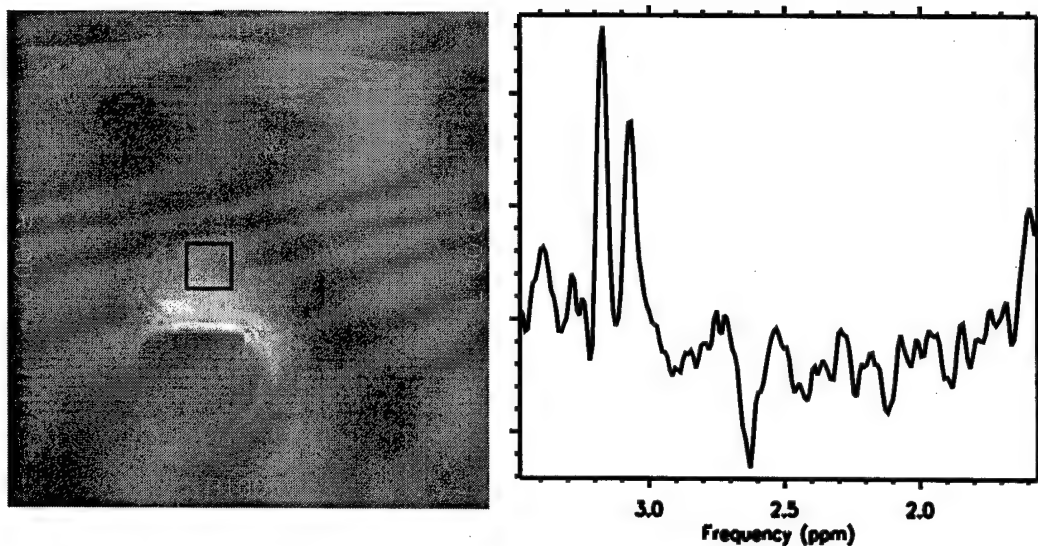


Figure 3: In vivo single voxel spectroscopy measurement. Measurement region was selected from the T2 weighted anatomic image as shown using the PRESS sequence at an echo time of 90 ms where an inverted peak of the Citrate metabolite should be observed. As the result spectrum suggests, the presence of the Citrate metabolite can be seen at the 2.6 ppm region as an inverted peak. Other metabolites of interest for detection of PCa, namely the Creatine and Choline peaks can also be observed.

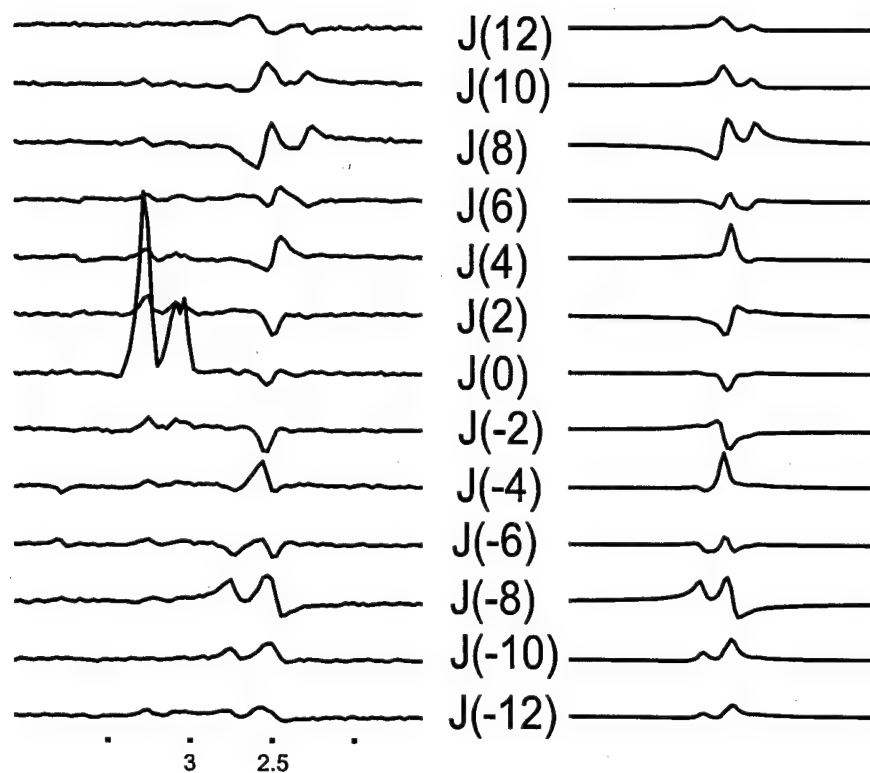


Figure 4: 2D J-resolved spectra obtained from simulations (right) and phantom measurements (left) at 3T using the PRESS sequence. The echo time interval was 7.8 ms starting from 35 ms for 64 steps. For the phantom measurement, Choline and Creatine metabolites were added to mimic PCa. Due to modulations as a function of echo time, the J-resolved spectra show strong signal of the Citrate metabolite at lines outside of J(0). Simulated J-resolved spectra and phantom measured J-resolved spectra are shown with similar spectral patterns. In this respect, the detection of the Citrate resonance can be made robustly using J-resolved acquisitions.

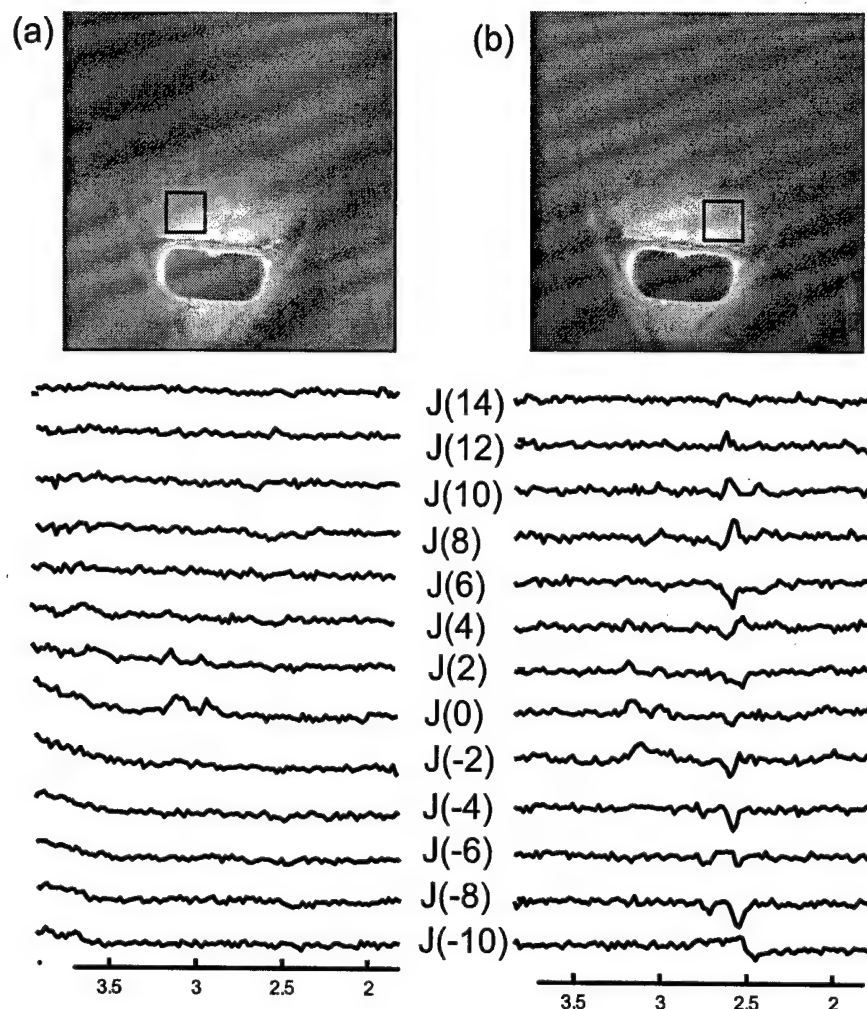


Figure 5: Single voxel 2D J-resolved spectroscopy results obtained from an in vivo subject suspicious of PCa. Two voxels were selected for the single voxel examinations as shown in the T2 weighted anatomical images. The corresponding J-resolved spectra are shown on the bottom of each image. In (a), even though the presence of Creatine and Choline metabolites are evident, there is no visible Citrate. As for the region shown in (b), the Citrate resonance is visible (2.6 ppm region from J(-10) to J(10) line) in the J-resolved spectra while other metabolites are also present. This shows the J-resolved spectroscopy can be useful for the detection of the Citrate metabolite as well as other metabolites of interest in the detection of PCa.

# Molecular/functional image-guided Intensity modulated radiation therapy

LEI XING<sup>1</sup>, YONG YANG<sup>1</sup>, AND DANIEL M. SPIELMAN<sup>2</sup>

Department of Radiation Oncology<sup>1</sup> and Radiology<sup>2</sup>, Stanford University School of Medicine, Stanford, CA 94305

Telephone: (650) 498-7896

Fax: (650) 498-4015

Email: [lei@reves.stanford.edu](mailto:lei@reves.stanford.edu)

1. Introduction
  - 1.1 Molecular and functional imaging
  - 1.2 IMRT as a means of producing biologically conformal dose distributions
2. Functional and molecular imaging and biologically conformal radiation therapy
  - 2.1 Integration of functional and molecular imaging into IMRT planning
  - 2.2 Image registration
  - 2.3 Quality assurance of molecular and functional imaging modalities
  - 2.4 Inverse treatment planning
    - 2.4.1 Objective function
    - 2.4.2 Relation between metabolic abnormality level and radiation dose
    - 2.4.3 Implementation
    - 2.4.4 Role of intra-structural tradeoff
    - 2.4.5 Spectral uncertainty
    - 2.4.6 Biological model for molecular/functional image-guided IMRT
    - 2.4.7 Plan review tools
3. Conclusion

## 1 Introduction

### 1.1 Molecular and functional imaging

For much of the last century, medical imaging has been focused on faster and more detailed anatomic pictures of the human body. The accomplishment of the visible human project of the National Library of Medicine (<http://www.nlm.nih.gov/research/visible>) represents perhaps one of the most important milestones in these developments. With the goal of producing a system of knowledge structures that transparently links visual knowledge forms to symbolic knowledge formats such as the names of body parts, a complete, anatomically detailed, 3D representations of the normal male and female human bodies were rendered based on transverse CT, MR and cryosection images of male and female cadavers. Medical imaging has been an integral part of radiation therapy since the discovery of x-rays and the imaging techniques, such as X-ray, CT, MRI and ultrasound imaging, are the foundation for the modern radiation therapy modalities that are routinely used in the clinics, such as 3D conformal radiation therapy, intensity modulated radiation therapy (IMRT), stereotactic radiosurgery, and brachytherapy. Indeed, the development of radiation therapy has strongly relied on the imaging technology and, historically, almost every major advancement in imaging science would bring radiation therapy to a new level.

In general, medical imaging is involved in all key steps of radiation treatment (figure 1). One of the most important uses of imaging techniques is the delineation of a tumor target. Despite the tremendous successes, the anatomic imaging techniques such as CT/MRI/US are inherently deficient in that they can only reveal spatial changes in physical properties and fail to provide basic biological information that is much needed for the optimal management of the patients. Clinically, tumor biology plays an important role in the diagnosis, treatment decision-making, and assessment of therapeutic response of various diseases. It is thus highly desirable to develop imaging techniques capable of revealing the spatial biology distribution of the patients. Toward this goal, a new branch of science, referred to as molecular imaging, is emerging as a result of research efforts in cellular biology and imaging techniques over the years. The development of cellular and molecular imaging provides significant opportunities for radiation discipline to take patient's biological information into radiation therapy treatment decision-making process and to truly individualize the cancer radiotherapy.

## 1.2. IMRT as a means of producing biologically conformal dose distributions

IMRT is an advanced form of external beam irradiation and represents a radical change in radiation oncology practice<sup>1-3</sup>. This new process of treatment planning and delivery shows significant potential for improving therapeutic ratio and offers a valuable tool for dose escalation and/or radiation toxicity reduction. Preliminary published results and unpublished results from several institutions indicate that with IMRT, radiation doses to sensitive structures can be reduced significantly while maintaining adequate target dose coverage<sup>4-15</sup>. Because in many clinical situations the dose to the tumor volume is limited by the tolerance doses of the sensitive structures, it is considered likely that IMRT will improve local control and lead to an increase in survival rate for certain cases through dose escalation. In addition, IMRT has the potential to improve the efficacy of treatment planning and delivery in routine clinical practice with the use of computerized planning and treatment process. For details about IMRT inverse treatment planning, delivery and quality assurance, we refer the readers to the related chapters of this book.

In IMRT, each incident beam is divided into a number of beamlets (typically, the size of beamlet is 1cmX1cm), allowing us to modify the dose distribution on an individual beamlet level. Using IMRT, it is possible to produce not only spatially uniform but also non-uniform dose distributions. Recently, Ling et al and several other researchers<sup>16-21</sup> have emphasized the technical capability of "dose painting" and "dose sculpting" offered by IMRT, which allows customized dose delivery to the target volume(s) with centimeter or even sub-centimeter spatial resolution. Using functional and molecular imaging techniques to identify spatial metabolic distribution and hence guide the delivery of radiation represents a paradigm shift in radiation oncology and this type of "biologically" conformal radiation therapy may provide a significant opportunity to improve conventional IMRT treatment. A timely question is how to integrate the state-of-the-art functional imaging technologies into radiation therapy techniques such as IMRT to positively impact clinical cancer management. The purpose of this Chapter is to review recent progress in this endeavor and identify the important issues in the development of biologically conformal radiation therapy.

## 2. Biologically conformal IMRT

Current IMRT treatment plan optimization is based on the assumption of uniform biology distribution within the target volume and is aimed at achieving geometrically conformal dose distributions under the guidance of CT/MRI images. In reality, it has long been recognized that the spatial distribution of biological properties in most tumors and normal tissues are heterogeneous. With the advent of various molecular and functional imaging techniques, it is now possible to map out biology distribution on a patient specific basis. To use the spatially heterogeneous biology information derived from the new imaging modalities to guide IMRT dose painting and sculpting process, several key problems need to be resolved. In general, the molecular/functional imaging-guided IMRT generally favors non-uniform dose distributions and requires a plan optimization formalism in voxel domain to deal with the biological heterogeneity. In addition, new method of specifying the desired doses and a mechanism for inter- and intra-structural tradeoff must be introduced to efficiently produce metabolically/functionally conformal doses. In figure 2 we list the general steps of biologically conformal IMRT treatment. Each of the steps in figure 2 is discussed.

### 2.1 Integration of functional and molecular imaging into IMRT planning

The area of molecular/functional imaging is rapidly evolving <sup>22-24</sup>. Many of the molecular imaging modalities (such as fluorescent and bioluminescent imaging, optical imaging, SPECT/PET with novel isotopes/contrast agents targeting some specific molecular markers, MR spectroscopic imaging (MRSI)) are being developed for tumour specific imaging and deployed into clinical practice. Presently, MRSI, PET/SPECT and micro-bubble based ultrasound are perhaps the most mature modalities and available for guiding radiation therapy treatment. Details on various molecular and functional imaging modalities have been given in Chapter 3 and will not be repeated here. We refer the readers to that Chapter and references therein. The remaining of this Chapter will be focused on the issues related to the integration of the new imaging modalities into radiation treatment planning.

### 2.2 Image registration

Radiation therapy treatment planning is mainly CT image-based because it provides complete geometric data and electron density information for accurate dose

calculation. To utilize the biological information derived from the new image modalities, we must map the imaging data onto treatment planning CT images. The level of complexity of image coregistration depends on the imaging techniques involved and specific software tools often need to be developed in order to use some of the new imaging modalities, such as fluorescent images, endoscopic images and endorectal images. Sometimes, deformable model-based image registration is required if the shape(s) of the involved organs are deformed from its normal shape.

Let us take endorectal MRSI as an example. The introduction of endorectal surface coils significantly improve spatial resolution and signal-to noise ratio (SNR) of prostate MR imaging and allows evaluation of the tumor location, tumor volume, capsular penetration, invasion of neurovascular bundle, and seminal vesicle involvement, which is crucial for accurate treatment planning. Endorectal-coil based MRSI has also been shown effective in distinguishing between areas of cancer and normal prostatic epithelium through differences in [choline+ creatine]/citrate ratio 25-28. However, the use of endorectal probe inevitably distorts the prostate and other soft tissue organs, making it impossible to directly fuse the acquired image data onto treatment planning CT. In figure 3 we show the difference between endorectal coil-based MRI defined and CT-defined prostate volume 29. In order to fuse MRI/MRSI with treatment planning CT, it is needed to develop an effective deformable image registration procedure. Otherwise, the gain from the use of the state-of-the-art imaging techniques may be lost due to the inferior performance of image registration.

Zaider et al 30 have reported a translation and scaling based registration method to map MRS positive volumes onto the CT and ultrasound images. In their approach, the coordinates of the boundary and the center of mass were used to linearly interpolate the positions of the mapped voxels. A larger discrepancy was found for regions with more severe distortion ( $\geq 4\text{mm}$ ). Lian et al 29, 31 have developed an effective deformable image registration algorithm to map the MRI/MRSI information obtained using a rigid or inflatable endorectal probe onto CT images and to verify the accuracy of the registration by phantom and patient studies. For this purpose, a thin plate spline (TPS) transformation first introduced by Bookstein 32 was implemented to establish voxel-to-voxel correspondence between a *reference* image and a *floating* image with deformation. The idea is to find a continuous transformation within a suitable Hilbert space to minimize the landmark



difference in two images. The detailed description of the TPS transformation can be found in Bookstein's original paper<sup>32</sup>. To access the quality of the registration, an elastic phantom with a number of implanted fiducial markers was designed. Radiographic images of the phantom were obtained before and after a series of intentionally introduced distortions. After mapping the distorted phantom to the original one, the displacements of the implanted markers were measured with respect to their ideal positions and the mean error was calculated. Phantom studies showed that using the deformable registration method the mean landmark displacement error was  $0.62 \pm 0.39$  mm when the distortion was of the order of 23.07 mm. A deformable model seems to be necessary to faithfully map the metabolic information onto the treatment CT images. When a non-deformable method based on a rigid-body transformation and scaling was used for the same distortion, the mean displacement of the fiducials with respect to their actual positions was found to be as large as  $12.95 \pm 0.57$  mm. In patient studies, CT images of two prostate patients were acquired, followed by 3 Tesla (3T) MR images with a rigid endorectal coil. For both patient studies, significantly improved registration accuracy was achieved. The prostate centroid position displacement was  $0.58 \pm 0.10$  mm and the coincidence index was  $92.6 \pm 5.1$  % when a TPS transformation was used. Different from the non-deformable approach, the TPS-based registration accommodates the organ distortion and enables us to achieve significantly higher MR/MRSI and CT image registration accuracy. More advanced finite element method is also developed to attack the problem<sup>33</sup>.

### 2.3 Quality assurance of molecular and functional imaging modalities

Any new imaging modality requires validation and quality assurance to ensure that the obtained images faithfully reflect the reality. In anatomical imaging, surrogate phantoms have been widely used for assessing the geometric and physical (e.g., electron density) properties of the images. For radiation therapy application, Mutic et al have reported a simple design of PET phantom to validate the image registration of PET and CT images<sup>34</sup>. Generally speaking, for a biological imaging modality, validation of geometric accuracy represents only one facet of the problem. The accuracy of the pixel values of the imaging modality also needs our attention. While the specific meaning of the pixel values depends on the modality, let us take an MRSI phantom (figure 4) constructed by Hunjan et al as an example to illustrate

the basic idea. The multi-modality, multi-purpose phantom is suitable for quality assurance testing of fusion data from MRI, MRSI and CT images<sup>35</sup>. The phantom contains fiducial markers that are simultaneously MR, MRS, and CT-visible. To examine the accuracy of MRSI for brain tumor, the phantom was filled with a brain-mimicking solution with an insert holding 8 vials containing calibrated solutions of precisely varying metabolite concentrations that emulated increasing grade/density of brain tumor. Metabolite ratios calculated from fully relaxed 1D, 2D and 3D MRS data for each vial were compared to calibration ratios acquired *in vitro* using a 9.4 Tesla MR spectrometer. Figure 5 shows an axial scout scan of the MRS metabolite ratio quantitation standard showing the calibration vials 1-8. The resulting single voxel MR spectra are shown inset next to corresponding vials and a linear fit between the Choline/NAA ratio of the calibration solutions obtained at 9.4 T versus the calibration-solution-filled vials inside the phantom obtained at 1.5 T. For detailed information on the design of the phantom and measurements, please refer 35, 36.

## 2.4 Inverse planning

In general, molecular/functional imaging could impact the current radiation therapy treatment in two fundamental aspects 16, 20, 37. First, it offers an effective means for us to more accurately delineate the tumor and better define the treatment volume. Secondly, it provides valuable spatial metabolic information in the tumor and sensitive structures. While it is straightforward to modify the radiation portals to accommodate any changes in treatment volume, new methods of dose optimization and medical decision-making must be developed to take full advantage of the metabolic information and IMRT. We have recently introduced the concept of 4D inverse planning and demonstrated the integration of MRSI into IMRT planning. The goal of this type of treatment scheme is to achieve biologically conformal doses, instead of the geometrically conformal dose distribution sought by conventional radiation therapy planning. We showed that, under the guidance of MRSI metabolic maps, it is possible to prescribe a higher dose where there is resistance and/or where there are dense tumor cell populations. Similarly, the technique also allows for differential sparing of sensitive structures accounting for functionally important regions. A few important issues related to new inverse planning scheme are outlined in the following.

#### 2.4.1 Objective function

The objective function is used in inverse planning to quantitatively rank the candidate plans and the optimization of the function yields the optimal input beam parameters. Ideally, an objective function should rank a given solution in a way consistent with the clinical judgment. Despite of intense research effort in modeling the clinical decision-making strategies 38, 39 40 41, 42, appropriate form of the objective function for clinical IMRT planning remains illusive even for conventional IMRT inverse planning. Our recent study has indicated that the IMRT plans derived from the existing inverse planning techniques are, at best, sub-optimal. For convenience, it seems appropriate to classify the currently available dose optimization methods into four categories: (i) dose-based<sup>43-48</sup>; (ii) clinical knowledge-based<sup>49</sup>; (iii) EUD-based<sup>50-53</sup>; and (iv) TCP/NTCP-based<sup>38, 54, 55</sup>. The underlying difference between these models lies in that what endpoint are used to quantify the treatment or what fundamental quantities are used to define the optimality of a plan. In reality, each type of inverse planning formalism has pros and cons. The dose-based, EUD-based and TCP/NTCP-based optimizations have been discussed extensively in the previous Chapters. We focus our discussion on the 2<sup>nd</sup> category here.

To illustrate the need for a biologically more sensible yet clinically more relevant approach, let us take parotid glands as an example. It is well known that the clinical end point is the same if the glands are irradiated 15Gy to 67%, or 30Gy to 30%, or 45Gy to 24% of the total volume<sup>56</sup>. A quadratic objective function or alike would rank the three scenarios completely differently. The use of dose-volume constraints does not change the ranking because they act as “boundary conditions” only limit the search space. A minimum requirement for a sensible objective function is that it should be consistent with the existing clinical outcome data. While the biologically based models are more relevant for radiotherapy plan ranking, the dose-response function of various structures is not sufficiently understood and, at this point, there is considerable controversy about the models for computing dose-response indices and their use in optimization. In reality, it is difficult for clinicians to specify the optimization criteria in terms of certain dose response indices (e.g., TCP, NTCP and P<sub>+</sub>). This issue becomes compounded when two or more independently optimized plans are to be combined. Towards developing a clinically

practical inverse planning formalism, we have proposed a new type of the inverse planning formulation with integration of clinical end point data and showed that the clinical knowledge-based model more objectively ranks radiation therapy plans and makes it possible to obtain truly optimal IMRT plans with much reduced efforts. The objective function is based on the concept of equivalent volume<sup>57-59</sup>,  $(\Delta V_{eff})_i$ , for an individual voxel  $i$ ,

$$(\Delta V_{eff})_i = V_i (D_i / D_{ref})^{1/n}, \quad (1)$$

where  $V_i$  is the volume of the voxel  $i$ ,  $D_i$  and  $D_{ref}$  are the dose and reference dose at the voxel, respectively,  $n$  is a parameter that represents the biological characteristic of the organ. For a sensitive structure,  $n$  is a small positive number ( $0 < n < 1$ ) and the value of parameter  $n$  reflects the architecture (serial or parallel) of the sensitive structure. For a target,  $n$  should be assigned with a small negative value ( $-1 < n < 0$ ). In order to model the volumetric effect, the objective function should take the form of

$$f_\sigma = f_\sigma(\{(\Delta V_{eff})_i\}). \quad (2)$$

In figures 6 and 7 we compare IMRT plans obtained using the clinical knowledge-based and conventional quadratic objective functions. As seen from the figures, dose distribution was significantly improved as a result of the more adequate modeling.

#### 2.4.2 Relation between metabolic abnormality level and radiation dose

An important task in biologically conformable radiation therapy is to quantify the tumor burden and relate the metric to the radiation dose. In Sec. 2.4.6 we will derive such a relation based on radiobiology model under the assumption that all necessary model parameters are known. At present, the radiobiology parameters are spares and one should perhaps take a less precise yet more practical approach. Generally speaking, the relation between the abnormality level and radiation dose can in principle be determined experimentally or through analysis of animal and hypothesis-driven clinical data, which is similar to the establishment of the empirical radiation dose prescriptions for different disease sites in our current clinical practice. A linear relation between the dose and metabolic abnormality levels<sup>20</sup>

$$D'(n) = D_0' + \kappa M(n), \quad (3)$$

was assumed in our previous study, where  $D'(n)$  is the prescribed target dose at voxel  $n$ ,  $M(n)$  is the abnormality level at the voxel,  $\kappa$  is an empirical coefficient,  $D_0'$  can be regarded as the conventional prescription dose when functional imaging information is

not available or when the abnormality level is minimum,  $M(n)=0$ . The bottom line is that no subvolume in the tumor should receive a dose less than conventionally prescribed dose  $D_0'$  unless it is clinically justifiable. For a given organ, we postulated that the tolerance dose is related to the functional importance by

$$D^c(n) = D_0^c - \alpha K(n), \quad (4)$$

where  $D^c(n)$  is the tolerance dose at voxel  $n$ ,  $K(n)$  is the functional importance at the voxel,  $\alpha$  is an empirical coefficient,  $D_0^c$  represents the tolerance dose corresponding to the situation when functional distribution information is not available or when the functional importance is minimum,  $K(n)=0$ .

We emphasize that the above two relations are somewhat *ad hoc* and may need to be refined as more knowledge are gained. For treatment of dose-response neoplasm, such as prostate cancer, it seems to be a good strategy to attempt to escalate the dose to those high tumor burden points as high as possible while keeping the normal tissue complications below a certain level. In this case, the linear relations (3) and (4) serves as a reasonable starting point for fine-tuning or optimization.

#### 2.4.3. Implementation

Some preliminary studies of incorporating metabolic information into the IMRT inverse planning has been reported by our group<sup>20</sup> and others and the technical feasibility of planning deliberately non-uniform dose distributions in accordance with functional imaging requirements has been demonstrated. In our preliminary study, a conventional quadratic objective function was used with an iterative inverse planning algorithm for the optimization of the system with inhomogeneous dose prescription specified according to the method described above. The generalized quadratic objective function used for the 4D-dose optimization problem reads <sup>20</sup>

$$F = \sum_{\sigma=1}^{n_{\sigma}} \left[ \frac{r_{\sigma}}{N_{\sigma}} \sum_{n=1}^{N_{\sigma}} r_n \cdot [D_c(n) - D^p(n)]^2 \right], \quad (5)$$

where  $N_{\sigma}$  represents the total number of voxels of a structure,  $D_c(n)$  is the calculated dose at voxel  $n$ ,  $D^p(n)$  is the prescribed dose given by Eq. (3) or (4) depending on whether the voxel  $n$  belongs to the target or normal tissue. The weighting factor at a voxel  $n$  is a product of two factors, an overall factor specific to the structure  $\sigma$ ,  $r_{\sigma}$ , and a voxel dependent component <sup>60</sup>,  $r_n$ , describing the relative weighting of different voxels inside the structure.

For testing purpose we constructed a phantom with a few hypothetical metabolic distributions in the tumor and functional importance distributions in the sensitive structure, as shown in top row of figures 8. The use of phantom case with hypothetical functional data allows us to systematically test the performance of the algorithm effectively without going into the technical details of functional imaging modalities. In figure 8 we show the IMRT plans obtained for these hypothetical situations. Figure 9 shows a six-field (0, 55, 135, 180, 225 and 305 degrees in IEC convention) IMRT glioma case. The MRSI metabolic map was discretized into three discrete levels (figure 9A). The level of abnormality at a point is characterized by an index based on the number of standard deviations (SD) from normal values of the choline/NAA ratio. The tumor was unifocal and 44 Gy was prescribed to the volume between the tumor boundary and the 1<sup>st</sup> abnormality level (AL=3) and 64 Gy was prescribed to the highest abnormal region (AL between 5 and 7).

#### 2.4.4 Role of intra-structural tradeoff

Even in conventional inverse planning scheme, voxels within a target or a sensitive structure volume are generally not equivalent in achieving their dosimetric goals in IMRT planning. Depending on the patient's geometry, beam modality and field configuration, some regions may have better chance to meet the prescription than others, and *vice versa*. It has shown <sup>61</sup> that the purposed modulation of spatial penalty distribution is more advantageous over the conventional inverse planning technique with structurally uniform importance factors, leading to significantly improved IMRT treatment plans that would otherwise unattainable. An example is given in figure 10, in which the isodose curves are "pushed" toward the target volume and the dose gradient at the tumor boundary is greatly increased. The significant improvement is also demonstrated in the DVH plots. It is remarkable that by simply modulating the spatial importance distribution an almost uniform reduction of ~20% (normalized to the maximum sensitive structure dose) in the sensitive structure dose was accomplished. Conversely, the target dose can often be escalated by ~10% while keeping the radiation toxicity at its current IMRT level.

The intra-structural tradeoff plays a more important when dealing with biologically heterogeneous systems since non-uniform dose prescription often aggregates the competition among the voxels. The approach proposed by Shou and Xing can be easily extended for the determination of an adequate set of voxel

dependent importance factors to model the intra-structural tradeoff. Briefly, once the prescription dose is given, it is possible to quantify the degree for a voxel to achieve its dosimetric goal by introducing the concept of dosimetric capability for each voxel in a target or sensitive structure. As an example, in figure 11 we show the capability maps obtained for a uniform dose prescription when five incident beams are involved. The capability of a voxel represents *a priori* dosimetric knowledge of the system. The intra-organ tradeoff is then modulated purposely using a heuristic relationship between the inherent dosimetric capability and the voxel-based weighting factors. In such way, we can impose a differential penalty scheme and allows the system to suppress potential overdosing spots and boost the potential underdosing spots, leading to a solution that is more consistent to our clinical expectation.

The voxel based penalty scheme can also be used as a means to fine-tune the regional doses. Clinically, it happens frequently that, after optimization, the dose at all but just one or a few small regions are satisfactory and thus prevent the plan from being acceptable. The difficulty is that the location of the hot/cold region in inverse planning is generally not known until the “optimal” plan is obtained. Consequently, an “on-the-fly” mechanism is highly desirable to adaptively fine-tune the dose distribution after a solution close to the optimum is obtained. Currently, the modification can only be achieved through adjusting structure dependent system parameters (e.g., prescription, importance factors), which influence not only the dose at the region of interest but also at other areas. In order to modify the dose at a specific region, in principle, one can use ray-tracing to find the beamlets that intercept the area and adjust their intensities accordingly. But there are numerous ways to change and the optimal arrangement of the beamlet intensities is not obvious. In biologically conformal IMRT, the issue becomes more urgent. The voxel dependent penalty scheme provides a practical solution for us to modify the local dosimetric behavior effectively, as has been demonstrated in recent studies of our group <sup>62, 63</sup> and Wu et al. <sup>64</sup>

#### 2.4.5 Spectral uncertainty

In practice, molecular/functional imaging data do not always accurately reflect the actual metabolic level over the entire imaging volume because of some technical

limitations (in MRSI, for example, shimming can be problematic near air-filled cavities and may strongly depend on the surface coil SNR on the spatial position). To fully utilize the metabolic information, it is desirable to develop an algorithm to numerically incorporate the spectral uncertainties (confidence map) into IMRT treatment planning. A statistical analysis-based inverse planning seems to be ideally suitable for this purpose. Assuming that the fluctuation of the spectral activity or the prescribed dose  $D^p(n)$  at voxel  $n$  is specified by a probability distribution  $P_n(D^p)$ , we incorporate the  $P_n(D^p)$  by using a statistical inference technique. Considering that currently available functional image data are not completely reliable and that missing or incomplete spectral data may occur frequently, such type of technique should be useful to minimize the effect and generate statistically optimal treatment plans. When there is no uncertainty in the spectral data, the algorithm reduces to the conventional inverse planning scheme.

#### 2.4.6 Biological model for molecular/functional image-guided IMRT

Dose-based, and more recently, clinical knowledge-based model provides an immediately applicable technique for generating spatially non-uniform dose distributions. However, a biological model-based approach is more fundamental and logical in dealing biological imaging data and is worth of a detailed investigation. Two important questions in the biological modeling of the system are:<sup>65</sup> (i) how to determine the non-uniform dose prescription provided that the biology distribution is known; and (ii) how to find the optimal solution. While the latter problem is similar to that in conventional IMRT inverse planning, the solution to the first problem entails some theoretical considerations. In Sec. 2.4.2 we have used the metabolic abnormality index to phenomenologically characterize the tumor burden. Using radiobiological model, it is possible to relate the prescription dose to the more fundamental radiobiology parameters to optimize the cell killing.

Let us start with the linear quadratic (LQ) model. We include the effect of tumor cell proliferation but ignore the quadratic term. The model parameters include clonogen density ( $\rho$ ), radiosensitivity ( $\alpha$ ), and proliferation rate ( $\gamma$ ). The time dependence of the parameters are ignored. The tumor control probability,  $TCP_i$ , for a tumor voxel  $i$ , can be expressed as

$$TCP_i = \exp[-\rho_i V_i \exp(-\alpha_i D_i + \gamma_i \Delta T)], \quad (6)$$



where  $V_i$  is the volume of voxel  $i$ ,  $\rho_{0i}$ ,  $\alpha_i$  and  $\gamma_i$  represent the initial clonogen density, radiosensitivity and proliferation rate in voxel  $i$ , respectively,  $D_i$  is the dose received by voxel  $i$ , and  $\Delta T$  is the overall treatment time. In Eq. (6),  $\gamma_i = \ln 2 / T_{pi}$  where  $T_{pi}$  is the potential doubling time in voxel  $i$ . TCP for the tumor is given by

$$TCP = \prod_i TCP_i. \quad (7)$$

A constraint from the normal cells within the tumor volume given by

$$\sum_i m_i D_i = E_t \quad (8)$$

should be applied to determine the tumor dose prescription, where  $m_i$  is the mass of voxel  $i$ ,  $E_t$  is the integral dose in tumor. The problem now becomes to maximize the TCP under the constraint of equation (6), which can be solved using the method of Lagrange multipliers<sup>66</sup>. When the mass and volume are equal for all tumor voxels, the desired prescription dose of a voxel is given by

$$D_i = \frac{\alpha_r}{\alpha_i} D_r - \frac{1}{\alpha_i} (\gamma_r - \gamma_i) \Delta T - \frac{1}{\alpha_i} \ln \left( \frac{\alpha_r \rho_{0r}}{\alpha_i \rho_{0i}} \right). \quad (9)$$

IMRT inverse planning optimization can proceed by numerically maximize the TCP while maintaining the NTCP below a certain limit. One can also take a "hybrid" approach by using the conventional objective function with the above dose prescription.

#### 2.4.7 Plan review tools

The sheer volume of information inherent in 3D treatment designs and the corresponding dose distributions make display and objective assessment problematic. Details of a dose-distribution's spatial characteristics can be obtained by examining 2D isodose curves in a slice-by-slice fashion; however, this is a quasi-quantitative, time-consuming process and is not an efficient way to compare competing plans even for conventional IMRT. In the presence of an additional degree of freedom (metabolic abnormality), the problem is exacerbated by the breakdown of uniform dose assumption within the target volume. One of the commonly used approaches is the reliance on data reduction techniques in the quantitative assessment of alternative plans. DVH is one of the most widely used data reduction techniques. This technique enables the ready reduction of the complex 3D data set of a treatment design into the 2D display of the fractional volume of a given structure receiving doses within a particular range.

Unfortunately, this tool becomes invalid for 4D plan evaluation because of possibly non-uniform biological status of the involved structures. 4D IMRT technique requires new plan review tools to facilitate the quantitative comparison of plans. The following are a few tools that are potentially useful for the plan review of molecular/functional image guided IMRT plans.

a). Effective isodose dose distribution: The effective dose at a voxel is defined as the ratio of the physical dose and the prescribed dose. This distribution considers both the spatial dose distribution and the metabolic map and provides intuitive information on the geometric location of underdosing or overdosing regions. In this way, we can use conventional wisdom to evaluate a 4D-dose distribution. The DVH corresponding to the effective dose distribution is also useful.

b). DVH clusters: In practice, not all underdosing/overdosing are equally significant and underdosing/overdosing at a certain metabolic level maybe more acceptable than at other metabolic levels. A cluster of DVHs, each corresponding to an incremental range of metabolic activity of interest, may provide useful tool to address the issue. The cluster of DVHs can be used to check the overall dosimetric behavior at an individual metabolic level. Figure 11 represents an example of a 3-level DVH cluster. For a sensitive structure with functional data available, similar technique applies.

c). Functional dose-volume histogram (FDVH): Distribution of functional importance appears to be heterogeneous in some normal organs and functional imaging modalities such as MRSI or PET/SPECT may provide valuable information about the spatial distribution of the functional importance. The FDVH, originally introduced by Lu *et al.* <sup>67</sup>, Marks *et al.* <sup>68</sup>, and Alber and Nusslin <sup>69</sup>, may prove to be a useful plan review tools. A similar histogram function can be introduced for the tumor, but its usefulness needs to be justified.

d). Modified TCP and NTCP calculation tools: The conventional TCP and NTCP formula <sup>57 50, 70, 71</sup> need to be modified to take into account the heterogeneous biology distribution <sup>72-74</sup>. This modification should be straightforward if the spatial distributions of radiobiological parameters are known. Although it is difficult to obtain quantitative results from the model calculation because of the uncertainties in the parameters, qualitative conclusions regarding the deliberately non-uniform irradiation scheme can be drawn and may shed useful insight into the problem <sup>74</sup>.

### 3. Conclusion

The success of radiotherapy critically depends on the imaging modality used for treatment planning and the level of integration of the available imaging information. The use of functional/metabolic imaging provides us much more than a tool to better delineate the boundary of a tumor target. Together with anatomical CT or MRI images, functional imaging affords valuable 4D data (3D structural plus 1D metabolic) for both tumor and sensitive structures, valuable for guiding us to design spatially non-uniform dose distributions to deliver high doses to where the tumor burdens are high and differentially spare the sensitive structures according to the functional importance distributions. The integration and utilization of the functional data in radiation therapy treatment planning become increasingly important to improve clinical cancer management. While it is straightforward to modify the radiation portals to accommodate any changes in treatment volume, new methods of dose optimization and medical decision-making must be developed to take full advantage of the metabolic information and IMRT. How to achieve biologically conformal doses, instead of the geometrically conformal dose distribution, presents a new challenge to radiation oncology discipline. Hopefully, with the efforts from multi-institutions, the new approach of imaging, planning and decision-making will be resolved. Ultimately, whether using deliberately inhomogeneous dose distributions obtained under the guidance of functional imaging such as MRSI can improve patient survival and reduce the side effects associated with radiation treatment should be established through extensive clinical trials.

### Acknowledgements

We would like to thank Drs. A. Boyer, S. Hunjan, J. Lian, C. Cottrutz, Z. Shou, P. Maxim, E. Schreibmann, Q. Le, S. Hancock, I. Gibbs, K. King, B. Daniel, D. Kim and E. Adalsteinsson for many useful discussions. We also wish to acknowledge grant support from the NCI 5R0 CA98523-02, NIH P41 RR09784, Department of Defense (DAMD17-03-1-0023), and the Vadasz Family Foundation. The authors are also grateful to the publishers of *Physics in Medicine and Biology*, *Medical Physics*, and *International Journal of Radiation Oncology, Biology and Physics* for the permission of using their copyrighted figures.

## References

1. Webb S. Intensity-Modulated Radiation Therapy. Bristol: Institute of Physics Publishing, 2001:xv, 633.
2. IMRT Collaborative Working Group. Intensity-modulated radiotherapy: current status and issues of interest. International Journal of Radiation Oncology, Biology, Physics 2001; 51:880-914.
3. AAPM IMRT Sub-committee. Guidance document on delivery, treatment planning, and clinical implementation of IMRT: Report of the IMRT subcommittee of the AAPM radiation therapy committee. Medical Physics 2003; 30:2089-2115.
4. Carol M, Grant WH, 3rd, Pavord D, et al. Initial clinical experience with the Peacock intensity modulation of a 3-D conformal radiation therapy system. Stereotactic & Functional Neurosurgery 1996; 66:30-4.
5. Ling CC, Burman C, Chui CS, et al. Conformal radiation treatment of prostate cancer using inversely-planned intensity-modulated photon beams produced with dynamic multileaf collimation. International Journal of Radiation Oncology, Biology, Physics 1996; 35:721-30.
6. Woo SY, Grant WH, 3rd, Bellezza D, et al. A comparison of intensity modulated conformal therapy with a conventional external beam stereotactic radiosurgery system for the treatment of single and multiple intracranial lesions. International Journal of Radiation Oncology, Biology, Physics 1996; 35:593-7.
7. Le QT, Xing L, Boyer AL. Head and Neck IMRT--The Stanford Experience, International Symposium: 3D Conformal Radiation Therapy and Intensity Modulated radiation Therapy in New Millenium, Houston, 1999. Vol. 42. Medical Physics Publishing.
8. Hancock S, Luxton G, Chen Y, Xing L, Boyer AL. Intensity modulated radiotherapy for localized or regional treatment of prostate cancer: clinical implementation and improvement in acute tolerance, Annual meeting of ASTRO, Boston, MA, 2000.
9. Teh BS, Mai WY, Uhl BM, et al. Intensity-modulated radiation therapy (IMRT) for prostate cancer with the use of a rectal balloon for prostate immobilization: acute toxicity and dose-volume analysis. International Journal of Radiation Oncology, Biology, Physics 2001; 49:705-12.
10. Huang E, Teh BS, Strother DR, et al. Intensity-modulated radiation therapy for pediatric medulloblastoma: early report on the reduction of ototoxicity. International Journal of Radiation Oncology, Biology, Physics 2002; 52:599-605.

11. Mundt AJ, Lujan AE, Rotmensch J, et al. Intensity-modulated whole pelvic radiotherapy in women with gynecologic malignancies. *International Journal of Radiation Oncology, Biology, Physics* 2002; 52:1330-7.
12. Mundt AJ, Roeske JC, Lujan AE, et al. Initial clinical experience with intensity-modulated whole-pelvis radiation therapy in women with gynecologic malignancies. *Gynecologic Oncology* 2001; 82:456-63.
13. Chao KS, Deasy JO, Markman J, et al. A prospective study of salivary function sparing in patients with head-and-neck cancers receiving intensity-modulated or three-dimensional radiation therapy: initial results. *International Journal of Radiation Oncology, Biology, Physics* 2001; 49:907-16.
14. Lee N, Xia P, Quivey JM, et al. Intensity-modulated radiotherapy in the treatment of nasopharyngeal carcinoma: an update of the UCSF experience. *International Journal of Radiation Oncology Biology Physics* 2002; 53:12-22.
15. Eisbruch A. Intensity-modulated radiotherapy of head-and-neck cancer: encouraging early results. *International Journal of Radiation Oncology Biology Physics* 2002; 53:1-3.
16. Ling CC, Humm J, Larson S, et al. Towards multidimensional radiotherapy (MD-CRT): biological imaging and biological conformality. *International Journal of Radiation Oncology, Biology, Physics* 2000; 47:551-560.
17. Goitein M, Niemierko A. Intensity modulated therapy and inhomogeneous dose to the tumor: a note of caution. Comment in: *Int J Radiat Oncol Biol Phys* 1997 Jul 15;38(5):1138-9. *International Journal of Radiation Oncology, Biology, Physics* 1996; 36:519-22.
18. Macklis R, Weinhaus M, Harnisch G. Intensity-modulated radiotherapy: rethinking basic treatment planning paradigms. *International Journal of Radiation Oncology, Biology, Physics* 2000; 48:317-8.
19. Rosenman J. Incorporating functional imaging information into radiation treatment. *Seminars in Radiation Oncology* 2001; 11:83-92.
20. Xing L, Cotrutz C, Hunjan S, Boyer AL, Adalsteinsson E, Spielman DM. Inverse Planning for Functional Image-Guided IMRT. *Physics in Medicine & Biology* 2002; 47:3567-3578.
21. Alber M, Paulsen F, Eschman SM, Machulla HJ. On biologically conformal boost dose optimization. *Physics in Medicine & Biology* 2003; 48:N31-N35.
22. Contag CH, Ross BD. It's not just about anatomy: in vivo bioluminescence imaging as an eyepiece into biology. *Journal of Magnetic Resonance Imaging* 2002; 16:378-87.
23. Seltzer M, Schiepers C, Silverman DH, et al. Recent advances in imaging endogenous or transferred gene expression utilizing radionuclide technologies in

- living subjects: applications to breast cancer. *Journal of Nuclear Medicine* 2001; 42:586-90.
24. Cheery SR. In vivo molecular and genomic imaging: new challenges for imaging physics. *Physics in Medicine and Biology* 2003; 49:R13-R48.
25. Kurhanewicz J, Vigneron DB, Hricak H, et al. Three-dimensional H-1 MR spectroscopic imaging of the in situ human prostate with high (0.24-0.7-cm<sup>3</sup>) spatial resolution prostate carcinoma: MR imaging findings after cryosurgery. *Radiology* 1996; 198:795-805.
26. Zaider M, Zelefsky MJ, Lee EK, et al. Treatment planning for prostate implants using magnetic-resonance spectroscopy imaging. *International Journal of Radiation Oncology, Biology, Physics* 2000; 47:1085-96.
27. DiBiase SJ, Hosseinzadeh K, Gullapalli RP, et al. Magnetic resonance spectroscopic imaging-guided brachytherapy for localized prostate cancer. *International Journal of Radiation Oncology, Biology, Physics* 2002; 52:429-438.
28. Kim D, Mayer D, Xing L, Daniel D, Spielman D. In vivo detection of citrate for prostate cancer at 3 Tesla. *Magnetic Resonance in Medicine* 2004:submitted.
29. Lian J, Xing L, Hunjan S, et al. Mapping of the Prostate in Endorectal Coil-Based MRI/MRSI and CT: a Deformable Registration and Validation Study. *Medical Physics* 2003; 31:in press.
30. Zaider M, Minerbo GN. Tumour control probability: a formulation applicable to any temporal protocol of dose delivery. *Physics in Medicine & Biology* 2000; 45:279-93.
31. Lian J, Hunjan S, Dumoulin C, Levin J, Watkins R, Rohling K, Giaquinto R, Kim D, Lo, A., Spielman D, Daniel B, Xing L, Integrating Deformable MRI/MRSI and CT Image Registration into the Prostate IMRT Treatment Planning. *International Journal of Radiation Oncology, Biology and Physics* 2003; 57:S207.
32. Bookstein FL. Thin plate splines and the decomposition of deformations. *IEEE Trans. Pattern Anal. Mach. Intell.* 1989; 11:567-585.
33. Wu X, Yu C, DiBiase SJ, Gullapalli R. The application of deformable image registration for MRS in prostate treatment planning. *International Journal of Radiation Oncology, Biology and Physics* 2003; 57:S208.
34. Mutic S, Dempsey JF, Markman J, Chao KS, Purdy JA. Multimodality image registration quality assurance for conformal three-dimensional treatment planning. *Medical Dosimetry* 2001; 26:79-82.
35. Hunjan S, Adalsteinsson E, Kim DH, et al. Quality assurance of magnetic resonance spectroscopic imaging-derived metabolic data. *International Journal of Radiation Oncology, Biology, Physics* 2003; 57:1159-73.

36. Hunjan S, Spielman DM, Adalsteinsson E, Boyer AL, Xing L. Phantom for quality assurance testing of MRSI data incorporated into radiation treatment planning, in Proceeding of Annual Meeting of International Associate of Magnetic Resonance in Medicine, Honolulu, Hawaii, 2002.
37. Xing L, Cotrutz C, Hunjan S, Boyer AL, Adalsteinsson E, Spielman D. Inverse planning for functional image-guided IMRT, Oral Presentation in 2002 Annual Meeting of ASTRO, New Orleans, LA, 2002.
38. Mohan R, Wang X, Jackson A, et al. The potential and limitations of the inverse radiotherapy technique. *Radiotherapy & Oncology* 1994; 32:232-48.
39. Langer M, Brown R, Kijewski P, Ha C. The reliability of optimization under dose-volume limits. *International Journal of Radiation Oncology, Biology, Physics* 1993; 26:529-38.
40. Langer M, Morrill SS, Lane R. A test of the claim that plan rankings are determined by relative complication and tumor-control probabilities [see comments]. Comment in: *Int J Radiat Oncol Biol Phys* 1999 Feb 1;43(3):697-8. *International Journal of Radiation Oncology, Biology, Physics* 1998; 41:451-7.
41. Xing L, Li JG, Pugachev A, Le QT, Boyer AL. Estimation theory and model parameter selection for therapeutic treatment plan optimization. *Medical Physics* 1999; 26:2348-58.
42. Niemierko A, Herbert D, Yan D, et al. Uncertainties in model-based outcome predictions for treatment planning. *Medical Physics* 2002; 29:2109-27.
43. Bortfeld T, Burkelbach J, Boesecke R, Schlegel W. Methods of image reconstruction from projections applied to conformation radiotherapy. *Physics in Medicine & Biology* 1990; 35:1423-34.
44. Webb S. Optimisation of conformal radiotherapy dose distributions by simulated annealing. *Physics in Medicine & Biology* 1989; 34:1349-70.
45. Xing L, Chen GTY. Iterative algorithms for Inverse treatment planning. *Physics in Medicine & Biology* 1996; 41:2107-23.
46. Spirou SV, Chui CS. A gradient inverse planning algorithm with dose-volume constraints. *Medical Physics* 1998; 25:321-33.
47. Cho PS, Lee S, Marks RJ, 2nd, Oh S, Sutlief SG, Phillips MH. Optimization of intensity modulated beams with volume constraints using two methods: cost function minimization and projections onto convex sets. *Medical Physics* 1998; 25:435-43.
48. Xing L, Hamilton RJ, Spelbring D, Pelizzari CA, Chen GT, Boyer AL. Fast iterative algorithms for three-dimensional inverse treatment planning. *Medical Physics* 1998; 25:1845-9.

49. Yang Y, Xing L. Clinical knowledge-based IMRT plan optimization. *International Journal of Radiation Oncology, Biology, Physics* 2003;submitted.
50. Niemierko A. Reporting and analyzing dose distributions: a concept of equivalent uniform dose. *Medical Physics* 1997; 24:103-10.
51. Wu Q, Mohan R, Niemierko A, Schmidt-Ullrich R. Optimization of intensity-modulated radiotherapy plans based on the equivalent uniform dose. *International Journal of Radiation Oncology, Biology, Physics* 2002; 52:224-35.
52. Wu Q, Djajaputra D, Wu Y, Zhou J, Liu HH, Mohan R. Intensity-modulated radiotherapy optimization with gEUD-guided dose-volume objectives. *Physics in Medicine & Biology* 2003; 48:279-91.
53. Thieke C, Bortfeld T, Niemierko A, Nill S. From physical dose constraints to equivalent uniform dose constraints in inverse radiotherapy planning. *Medical Physics* 2002; 30:2332-2339.
54. Brahme A. Individualizing cancer treatment: biological optimization models in treatment planning and delivery. *International Journal of Radiation Oncology, Biology, Physics* 2001; 49:327-37.
55. Brahme A. Optimized radiation therapy based on radiobiological objectives. *Seminars in Radiation Oncology* 1999; 9:35-47.
56. Eisbruch A, Ten Haken RK, Kim HM, Marsh LH, Ship JA. Dose, volume, and function relationships in parotid salivary glands following conformal and intensity-modulated irradiation of head and neck cancer. *International Journal of Radiation Oncology, Biology, Physics* 1999; 45:577-87.
57. Lyman JT, Wolbarst AB. Optimization of radiation therapy, III: A method of assessing complication probabilities from dose-volume histograms. *International Journal of Radiation Oncology, Biology, Physics* 1987; 13:103-9.
58. Burman C, Kutcher GJ, Emami B, Goitein M. Fitting of normal tissue tolerance data to an analytic function. *International Journal of Radiation Oncology, Biology, Physics* 1991; 21:123-35.
59. Burman CM. Fitting of tissue tolerance data to analytic function: improving the therapeutic ratio. *Frontiers of Radiation Therapy & Oncology* 2002; 37:151-62.
60. Xing L, Li JG, Donaldson S, Le QT, Boyer AL. Optimization of importance factors in inverse planning. *Physics in Medicine & Biology* 1999; 44:2525-36.
61. Shou Z, Xing L. Improve IMRT dose distribution by using spatially non-uniform dose importance factors. *Proceeding of the 14th ICCR. Seoul, Korea, 2003.*
62. Cotrutz C, Xing L. Using voxel-dependent importance factors for interactive DVH-based dose optimization. *Physics in Medicine & Biology* 2002; 47:1659-1669.



63. Cotrutz C, Xing L. IMRT dose shaping using regionally variable penalty scheme. *Medical Physics* 2003; 30:544-551.
64. Wu C, Olivera GH, Jeraj R, Keller H, Mackie TR. Treatment plan modification using voxel-based weighting factors/dose prescription. *Physics in Medicine & Biology* 2003; 48:2479-2491.
65. Yang Y, Xing L. On the dose prescription in molecular/functional image-guided IMRT. *International Journal of Radiation Oncology, Biology, Physics* 2003:submitted.
66. Crooks S, Xing L. Application of constrained least-square techniques to inverse planning. *International Journal of Radiation Oncology, Biology, Physics* 2002:accepted.
67. Lu Y, Spelbring DR, Chen GT. Functional dose-volume histograms for functionally heterogeneous normal organs. *Physics in Medicine & Biology* 1997; 42:345-56.
68. Marks LB, Sherouse GW, Munley MT, Bentel GC, Spencer DP, Scarfone C. Incorporation of functional status into dose-volume analysis quantitative pulmonary single photon emission computed tomography for radiotherapy applications. *Medical Physics* 1999; 26:196-9.
69. Alber M, Nusslin F. Tools for the analysis of dose optimization: I. Effect-volume histogram. *Physics in Medicine and Biology* 2002; 47:2451-2458.
70. Martel MK, Ten Haken RK, Hazuka MB, Turrisi AT, Fraass BA, Lichter AS. Dose-volume histogram and 3-D treatment planning evaluation of patients with pneumonitis. *International Journal of Radiation Oncology, Biology, Physics* 1994; 28:575-81.
71. Martel MK, Ten Haken RK, Hazuka MB, et al. Estimation of tumor control probability model parameters from 3-D dose distributions of non-small cell lung cancer patients. *Lung Cancer* 1999; 24:31-7.
72. Webb S, Nahum AE. A model for calculating tumour control probability in radiotherapy including the effects of inhomogeneous distributions of dose and clonogenic cell density. *Physics in Medicine & Biology* 1993; 38:653-66.
73. Niemierko A, Goitein M. Implementation of a model for estimating tumor control probability for an inhomogeneously irradiated tumor. *Radiotherapy & Oncology* 1993; 29:140-7.
74. Popple RA, Ove R, Shen S. Tumor control probability for selective boosting of hypoxic subvolumes, including the effect of reoxygenation. *International Journal of Radiation Oncology Biology Physics* 2002; 54:921-927.

